Modelling and experiments on NTM stabilisation at ASDEX Upgrade

Laura Urso

Der Fakultät für Physik
der Ludwig -Maximilians-Universität München
zur Erlangung des akademischen Grades eines
Doktors der Naturwissenschaften (Dr. rer. nat.)
vorgelegte Dissertation

22 April 2009

Erstgutachter: Prof. Dr. Hartmut Zohm

Zweitgutachter: Prof. Dr. Harald Lesch

Tag der mündlichen Prüfung: 27 Juli 2009

Dedicato alla mia famiglia

Zusammenfassung

Man erwartet für das nächste Fusionsexperiment ITER, dass neo-klassische Tearing Moden (NTMs) einen sehr negativen Effekt auf den Einschluss des Plasmas haben werden. Diese resistiven Instabilitäten hängen mit dem Auftreten von magnetischen Inseln zusammen, die experimentell durch lokalen Elektron-Zyklotron Stromtrieb (ECCD) kontrolliert werden können. Die Stabilisierung und der Zerfall der Inseln kann mit Hilfe der so-genannten modifizierten Rutherford-Gleichung beschrieben werden. In dieser Arbeit werden die theoretischen Vorhersagen der modifizierten Rutherford-Gleichung für das Abnehmen der Inselbreite mit den experimentellen Werten verglichen, um die zwei freien, maschinen-unabhängigen Parameter der Gleichung zu bestimmen. Auf der Grundlage der Datenbanken von NTM-Stabilisierungsentladungen an ASDEX Upgrade und an JT-60U soll im Rahmen eines Multi-Maschinen-Benchmarks die benötigte Stabilisierungsleistung für ITER extrapoliert werden. Die experimentellen Ergebnisse an beiden Maschinen werden in ihrer Konsistenz überprüft und unter Einbeziehung einer Sensitivitätsanalyse werden die beiden freien Parameter der modifizierten Rutherford-Gleichung bestimmt. Dabei wird zum ersten mal die Asymmetrie der Insel mit in Betracht gezogen und der Effekt des ECCD auf die marginale Phase der Mode quantifiziert. Es wurde gefunden, dass vor allem der radiale Versatz des ECCD gegenüber der Insel und Überstabilisierung der Mode die entscheidenden Grössen bei der NTM-Stabilisierung und Modellierung sind. Als das wichtigste Ergebnis dieser Arbeit liefert die Extrapolation der Stabilitätsexperimente von ASDEX Upgrade und JT-60U, dass an ITER 10 MW ECCD-Leistung ausreichen um grosse NTMs zu stabilisieren, solange der ECCD-Strahl perfekt auf den O-Punkt der Insel trifft. Das grosse Verhältnis zwischen der saturierten Inselbreite und der ECCD-Depositionsbreite, das an ITER erwartet wird, erfordert einen kleinen radialen Versatz zwischen ECCD und der Insel von maximal 2-3 Zentimetern und impliziert, dass man nur wenig ECCD-Leistung bei moduliertem Stromtrieb, verglichen mit kontinuierlichem Stromtrieb, spart.

Abstract

In the next fusion device ITER the so-called neoclassical tearing modes (NTMs) are foreseen as being extremely detrimental to plasma confinement. This type of resistive instability is related to the presence in the plasma of magnetic islands. These are experimentally controlled with local electron cyclotron current drive (ECCD) and the island width decay during NTM stabilisation is modelled using the so-called Modified Rutherford equation. In this thesis, a modelling of the Modified Rutherford equation is carried out and simulations of the island width decay are compared with the experimentally observed ones in order to fit the two free machine-independent parameters present in the equation. A systematic study on a database of NTM stabilisation discharges from ASDEX Upgrade and JT-60U is done within the context of a multi-machine benchmark for extrapolating the ECCD power requirements for ITER. The experimental measurements in both devices are discussed by means of consistency checks and sensitivity analysis and used to evaluate the two fitting parameters present in the Modified Rutherford equation. The influence of the asymmetry of the magnetic island on stabilisation is for the first time included in the model and the effect of ECCD on the marginal island after which the mode naturally decays is quantified. The effect of radial misalignment and over-stabilisation during the experiment are found to be the key quantities affecting the NTM stabilisation. As a main result of this thesis, the extrapolation to ITER of the NTM stabilisation results from ASDEX Upgrade and JT-60U shows that 10 MW of ECCD power are enough to stabilise large NTMs as long as the O-point of the island and the ECCD beam are perfectly aligned. In fact, the high ratio between the island size at saturation and the deposition width of the ECCD beam foreseen for ITER is found to imply a maximum allowable radial misalignment of 2-3 cm and little difference in terms of gained performance between modulated ECCD and continuous ECCD.

Contents

Chapter 1

Introduction

1.1 Thermonuclear fusion

The controlled nuclear fusion of hydrogen isotopes in a plasma is one of the most promising energy resources for the future allowing for very high efficiency and higher environmental safety conditions compared to nuclear fission. In a laboratory, the reaction that offers the best energetics for thermonuclear fusion is one in which the nuclei of deuterium (D) and tritium (T) fuse to yield an α-particle and a neutron releasing 17.6 MeV of energy per reaction:

$$D_1^2 + T_1^3 \rightarrow He_2^4 + n_0^1 \tag{1.1}$$

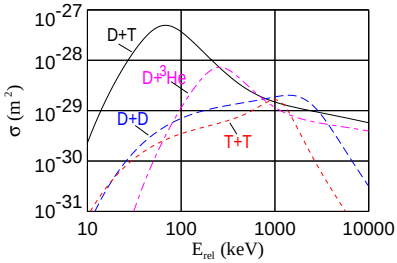

Figure 1.1: The fusion reaction $D_1^2 + T_1^3 \rightarrow He_2^4 + n_0^1$ has by far the largest cross-section at relatively low energies.

At low energies, the cross section for fusion is small due to the Coulomb barrier preventing the nuclei of the reactants to approach each other close enough to fuse. This repulsive force is eventually overcome as the kinetic energy of the nuclei increases. Actually the Deuterium-Tritium reaction can occur even before the Coulomb barrier is overcome because of quantum mechanical tunneling. In a commercial fusion reactor, the neutrons produced by these reactions will be used to breed tritium from lithium, which is very abundant on earth, via interactions with the wall. The α-particle heating provides an increasing fraction of the total heating and when adequate confinement conditions are provided, plasma temperature can be mantained against the energy losses above mentioned solely by α-particle heating contribution. If this is the case, the plasma is said to be in an ”ignited” state. The progress towards ignition is expressed in terms of a parameter, the triple product $nT\tau_E$, which brings out most clearly the requirements on density n, temperature T and on energy

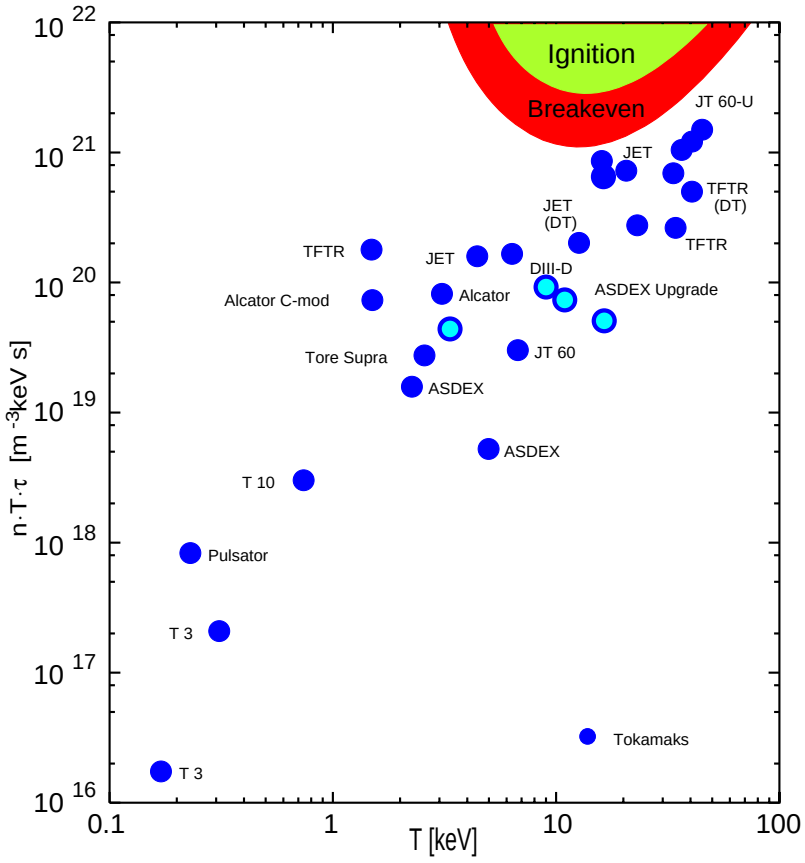

Figure 1.2: Contours for effective breakeven and ignition together with values of the fusion product obtained in several tokamaks.

confinement time τ_E (the ratio of the energy stored in the plasma to the heat loss rate) leading to the following condition for ignition:

$$nT\tau_E > 3 \cdot 10^{21} m^{-3} \text{keV s} \tag{1.2}$$

for values of T_e ranging between $10 \div 20\, keV$. The condition would be reached for example by $n = 1 \cdot 10^{20}\, m^{-3}$, $T_e = 10\, keV$ and a confinement time $\tau_E = 3\, s$. In a laboratory, the most feasible approach for confining a plasma is magnetic confinement. In general magnetic configurations of fusion interest are toroidal to avoid end-losses and, among them, the **tokamak** configuration has proven to be so far the most successful device in improving the desired fusion plasma conditions. For a tokamak, the principal magnetic field is the toroidal field. In order to have an equilibrium in which the plasma pressure is balanced by the magnetic forces (e.g Lorentz force), it is also necessary to have a poloidal magnetic field. This field is mainly produced by the current in the plasma itself, which flows in the toroidal direction. This current is produced by induction, the plasma

acting as the secondary winding of a transformer. It serves also for plasma build-up and ohmic heating. The induction of current dictates that operation needs to be pulsed. During the discharge, the plasma, due to its electrical resistance, is heated by the Joule (ohmic) dissipation of the current flowing through it but in addition other forms of heating as neutral beam injection NBI [Stäbler(2003)] are often employed to raise the temperature. The toroidal magnetic field, on the

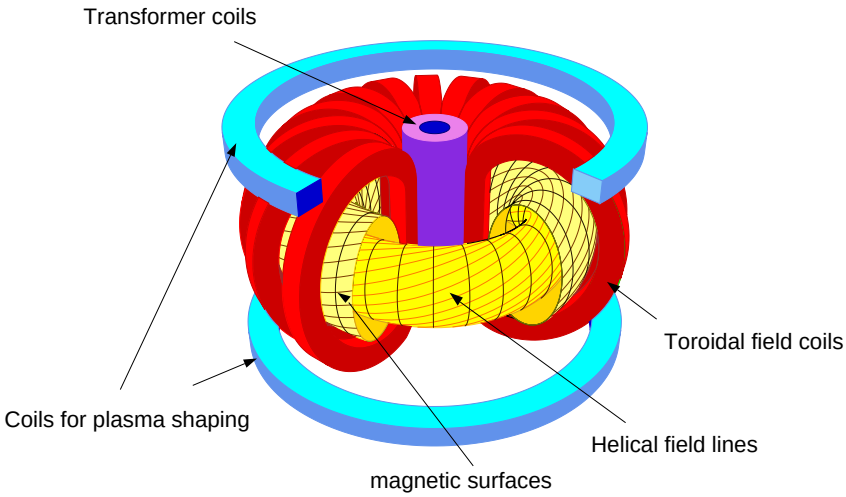

Figure 1.3: Tokamak concept: the axisymmetric toroidal field is produced by poloidal currents in a set of magnetic coils surrounding the plasma. A central solenoid is used to produce a time-varying poloidal magnetic flux which induces a toroidal loop voltage, and due to plasma resistivity, a plasma current.

other hand, is produced by currents in coils linking the plasma, as shown in figure 1.3. Over the past decades a number of medium and large size tokamaks like ASDEX Upgrade, Tore Supra and JET in Europe, JT-60U in Japan, TFTR and DIII-D in the USA and many others have been operated to investigate the physics aspects of fusion plasma physics. The improvement in fusion performance in these large experimental devices is mainly due to their increased size and power capability, to the exploration of new operational regimes, and to the progress in understanding basic physics processes. Typically the energy confinement times for these devices are proportional to $\propto \frac{1}{2} r_p^2$ where r_p is the mean minor radius of the plasma [Wesson(1997)], since on larger devices particles and energy require more time to diffuse away from the core region of the plasma and thus to reduce the confinement. Comparative studies of plasma behaviour and performance among these devices have made a fundamental contribution to the development of the physics basis for the design of ITER, (**I**nternational **T**hermonuclear **E**xperimental **R**eactor). For the main fusion devices the improvement towards ignition in terms of the fusion product $nT\tau_E$ is shown in figure 1.2 and it is expected that the ITER device will come close to reach ignition. ITER will be the next generation tokamak, which will have to prove deuterium-tritium burning

with substantial α-particle heating ($Q = P_{\mathrm{fus}} / P_{\mathrm{aux}} \geq 10$) and a fusion power of about 0.4-0.8 GW is expected to be produced during the burn time of about 1000 s. For the purpose of this thesis experimental data from ASDEX Upgrade and JT-60U has been investigated since these two devices contribute significantly to the extrapolation for ITER prediction in terms of size and performance and above all in terms of similar shape. As figure 1.4 shows, these two devices contribute in terms of size to build a step ladder towards ITER as their aspect ratio R_{maj} / a lies in both cases around 3 (see table 1.1).

Table 1.1: Main descriptive parameters for ASDEX Upgrade, JT-60U and ITER

Device	Major Radius R_{maj} [m]	Minor radius a [m]	Toroidal Field B_T[T]	Plasma current I [MA]	Heating Power P[MW]
ASDEX Up	1.65	0.5	3.9	1.0-1.4	28
JT-60U	3.4	1	4.2	2.5-5	58
ITER	6.2	2.0	5.3	15	~ 100

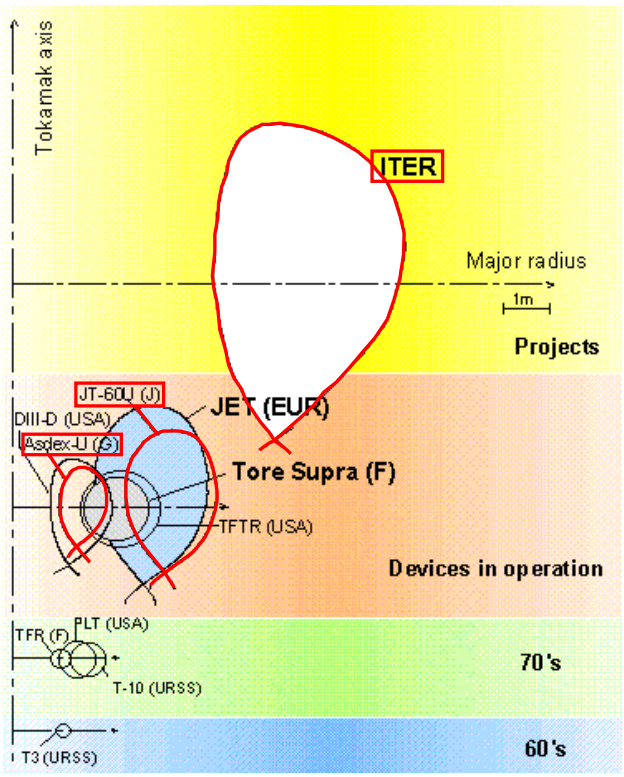

Figure 1.4: Poloidal cross-sections of ASDEX Upgrade, JT-60U and ITER tokamaks. ASDEX Upgrade and JT-60U have increasing size and an aspect-ratio R_{maj}/a similar at the ITER cross-section shape and therefore their results can be extrapolated for predicting ITER performance.

1.2 The q and the β parameter as important parameters in stability

In a tokamak equilibrium the magnetic force balances the plasma pressure: $\vec{j} \times \vec{B} = \nabla p$ (as shown in chapter 2) and this requirement leads to a set of nested magnetic surfaces on which $\vec{j}$ and $\vec{B}$ are constant. Each of these surfaces is characterized by its own value of magnetic flux and called flux surface [Wesson(1997)]. On these surfaces one can define the safety factor q. This name is due to the role it lays in determining the stability. In general, greater stability corresponds to higher values of q. In an equilibrium configuration each magnetic field line has a value of q and follows a helical path around the torus on its own magnetic surface. In cylindrical approximation, the definition of the q-value for a field line is the following:

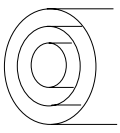
flux surfaces

$$q = \lim_{N_{\mathrm{tor}} \to \infty} \frac{N_{\mathrm{tor}}}{N_{\mathrm{pol}}} \tag{1.3}$$

where N_{tor} denotes the number of times a magnetic field line goes around a torus "the long way" (toroidally) for the number of times N_{pol} a magnetic field line goes around a torus "the short way" (poloidally). For example, a safety factor equal to 1 corresponds to a magnetic surface with field lines joining up on itself after exactly one rotation around the torus. In stability analysis, magnetic surfaces with rational values of the safety factor q become very important. If the field line joins up on itself after m toroidal turns, the safety factor reads $q = \frac{m}{n}$ where n and m are integers. Perturbations are easily excited on these surfaces since the field lines do not cover these surfaces ergodically. These flux surfaces are called resonant surfaces and the mode numbers (m,n) characterise the helicity of the standing waves which can occur as a consequence of the perturbation. An other important parameter is β defined as

$$\beta = \frac{2\mu_0 p}{B^2} = \frac{\text{plasma pressure}}{\text{magnetic field pressure}} \tag{1.4}$$

which characterizes the basic properties of the plasma. It represents the efficiency of the plasma confinement since it measures how much kinetic pressure ($p = nkT$, which in turn is related to the fusion power by the factor $\sim (nT)^2$), can be confined by a given magnetic pressure (which is a cost for the reactor). In principle, one would like to have β as large as possible, but its maximum value is usually limited in tokamak devices by the onset of various kind of MHD instabilities. Often, the normalised parameter β_N is used in order to measure how close one is to the limit set by ideal MHD (the Troyon limit $\beta_{\text{max,ideal}} \sim I/aB_T$):

$$\beta_N = \frac{\beta[\%]}{I[MA]/(a[m] \cdot B[T])} \tag{1.5}$$

where a is the minor radius of the plasma, B is the main magnetic field, I is the total plasma current.

1.3 Tearing Mode instability

An (m,n)-tearing mode is a resistive MHD instability characterized by a helical perturbation current on a resonant surface with $q = m/n$ in a tokamak plasma. For a classical tearing mode the perturbation current is due to an unfavourable equilibrium current profile parametrized by the so-called Δ' [Rutherford(1973)] which is a measure for the available magnetic energy to drive the instability. The associated perturbation of the magnetic system leads to reconnection of the flux surfaces and hence the formation of the so-called magnetic islands. Due to the resulting reduced radial heat insulation the pressure profile p inside the island is flattened. An important consequence is a loss of confined energy since heat and particles are moved towards the outside of the plasma. This is also observed by a drop in β.

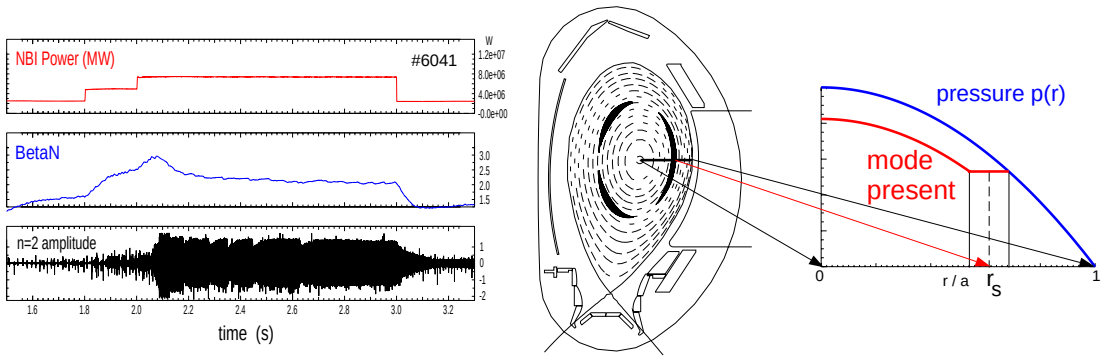

Figure 1.5: Limit in β and pressure degradation due to NTM

When the drive of the tearing instability is due to the loss of the current which is proportional to the pressure of the plasma, the tearing mode is called Neoclassical Tearing Mode (NTMs). As the NTM is triggered due to a small seed island generated by some initial perturbation (e.g. sawtooth crash) the β limit is reached and degraded. Because of toroidicity effects, which will be clarified in chapter 2, this may lead to further island growth although the seed island should be classically stable. Figure 1.5 shows a $m = 3$, $n = 2$ mode, forming three islands in the poloidal cross-section. If an island is formed at a rational surface with a high pressure gradient, the pressure gradient flattens in the island, as shown in fig. 1.5. The most common NTM instabilities are found at the q values 1.5 and 2, for $m = 3$, $n = 2$ and for $m = 2$, $n = 1$ respectively. (3,2) NTMs determine a loss of confinement of about $10\% - 30\%$ (soft-β limit). The (2,1) NTMs (hard-β limit), which occur at lower densities, can lead even to disruptions, that is the plasma confinement is suddenly destroyed. The typical value of β_N, at which these resistive modes appear is in the range 1.5-2.5 in discharges similar to those expected in the ITER plasma scenarios with high confinement (H-mode) [Editors(1999)]. The ideal β_N limit for ITER scenarios is 3.5-4, and it will require $\beta_N \geq 2$ to be able to ignite. However, this value is exactly in the range where the resistive modes can appear and limit the operational β_N below 2 and this is why it is important for projecting

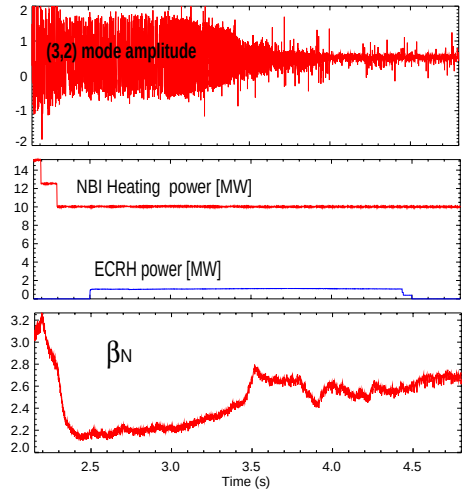

Figure 1.6: NTM stabilisation: as the NTM develops in the plasma, it lowers significantly the β_N. To control it, ECRH power is applied in form of ECCD so that the NTM can be reduced till it disappears from the plasma and the β_N can be recovered.

ITER performance to be able to predict their behaviour. Therefore, stabilisation methods are studied to control NTMs by reducing their mode amplitude until the magnetic islands totally disappear and the β value recovers (as shown in figure 1.6). These methods are based on driving appropriate electrical currents through the plasma [Zohm(2001)]. Direct control on NTMs is obtained by injecting rf waves, mainly with Electron Cyclotron Current Drive (ECCD) injected at the resonant surface of interest to substitute the loss of current inside the island with an externally applied one. In ASDEX Upgrade and JT-60U, typically, the (3,2) NTM is completely suppressed at ECRH power of roughly 10% of the total heating power. The (2,1) NTM can also be completely suppressed, but the power requirement is higher for this mode than for the (3,2) NTM since the current drive efficiency at larger minor plasma radius is reduced due to the lower temperature. ECCD is foreseen to be used for NTM stabilisation also in ITER and therefore extrapolation studies are needed to predict how much power will be required in ITER for this purpose. At present, ~ 20 MW of Electron Cyclotron Heating power (P_{ECRH}) are installed for NTM stabilisation.

1.4 Aim of this work

As already mentioned, ITER will be operating in a plasma scenario in which NTMs are predicted to be present and for which it will be necessary to provide an efficient scheme to control them. In view of this, theoretical and experimental efforts are constantly made to validate the present understanding on NTM physics and to actively control the presence of NTMs during the plasma operations. NTMs are a non-linear process which include magnetic reconnection phenomena and a complete fully-consistent theoretical description is still missing. Indeed, the large scale-processes involved in the evolution of the NTM can be well described by resistive MHD theory, whereas small-scale effects require at least a 2-fluid description of the plasma or even a full kinetic theory. The experiments carried out in the past years mainly focused on three aspects of the NTM physics:

- the study of the physics that seeds the NTMs [Günter(1998)].
- the observation of the phenomenology of the NTMs [Meskat(2001)]
- the study of the stabilisation of the NTMs by means of external applied current drive [Gantenbein(2000)], [Nagasaki(2003)]

A link between theory and experiment is to be found in the so-called Rutherford Equation [Rutherford(1973)] which is a non-linear equation describing the time

evolution of the magnetic island of width W associated to the NTM. The Rutherford Equation consists of different terms (so-called Δ-terms) which describe different physical mechanisms affecting the island width evolution. Originally, the Rutherford Equation described only the effect of the modification of the equilibrium current profile due to the presence of the island (Δ' effect) and later, as more and more physics underlying the evolution of the NTMs has been understood, other Δ-terms have been added to obtain the Modified Rutherford Equation. These terms can't be calculated analytically for a real shaped plasma and are derived using mainly cylindrical or simplified toroidal approximations. In addition, the saturated phase of the NTM can be relatively well described in terms of β dependency whereas the physics at small island size, which is crucial for understanding how NTMs can be triggered and controlled before they become too large in the plasma, is very much under debate and new terms at small island size have been introduced in the Rutherford Equation. As a consequence, some free coefficients need to be introduced in front of each Δ-term of the Modified Rutherford equation in order to account for real shape and possible missing physics. To evaluate these free coefficients and to determine the importance of each Δ-term in the equation the comparison with the experimental time evolution of the magnetic island $W(t)$ is necessary. This type of analysis is very sensitive to the quality of local measurements, to fitting of kinetic profiles, experimental set-ups, plasma conditions, etc. The first attempt to model the experimental observation of the NTMs with the Rutherford Equation took place in 1995 [Chang(1995)] and is shown in figure 1.7 and since then, in principle, the approach to study NTMs has not changed although it has been favoured by the availability of better diagnostics, a larger parameter space, larger sets of data and new terms at small island size. The aim of this work has been to test the Modified Rutherford Equa-

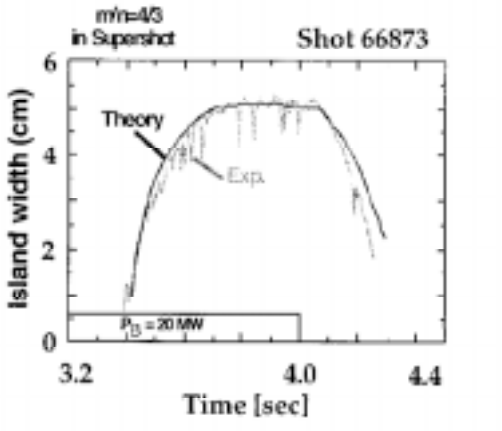

Figure 1.7: First observation and modelling of NTMs with the Modified Rutherford equation for a TFTR (4,3) NTM.

tion against experimental data by attempting to differentiate this analysis from the past works [Buttery(1999)], [Zohm(2001)], [Sauter(2002)], [Reimerdes(2002)], [Hayashi(2004)], [LaHaye(2006)] by:

- validating the terms present in the Modified Rutherford Equation and by checking how consistent are the fitting parameters over a relatively large database of discharges analysed.
- building up a robust methodology for the analysis of the NTM experiments.
- developing a cross-machine comparison between ASDEX Upgrade and JT-60U in order to be able to consistently extrapolate the results to ITER

Therefore, the open questions which are investigated in this thesis are

1. whether the experimental NTM evolution during ECCD stabilisation is fully described with the Modelled Rutherford equation
2. what are the main issues which arise when doing a cross-machine benchmark for the NTM stabilisation with ECCD in view of ITER
3. what is the prediction for the amount of power required to stabilise NTMs with ECCD in ITER

The experimental data has been collected both at ASDEX Upgrade and JT-60U and it covers the whole range of experimental studies on NTMs mentioned above. This makes it a complete database for extrapolating to ITER the ECCD power requirements in the most consistent way. The work discussed in this thesis has been conducted at the ASDEX Upgrade tokamak experiment, at the Max-Planck-Institut für Plasmaphysik (IPP) in Garching (Germany) and fruitful collaboration with JT-60U. It is organised as follows: the derivation of the Modified Rutherford equation with only two free parameters tested in this work is presented in chapter 2. In chapter 3, the plasma parameters and the measurements required for the analysis are presented whereas in chapter 4 an overview of the experimental discharges taken both from ASDEX Upgrade and from JT-60U is given. In chapter 5 the method used for the fitting of the Modified Rutherford equation is introduced and the fitting analysis is carried out. In chapter 6, the error on the results of chapter 5 is quantified and discussed by using a probabilistic approach. Finally, in chapter 7, the predictions for ITER are carried out and in chapter 8 the work is summarised and conclusions are given.

Chapter 2

Modelling of the experimental behaviour of Neoclassical Tearing Modes

Tearing Modes are due to the rise of a current in the plasma which perturbs the equilibrium magnetic field line configuration. As a consequence of this, magnetic reconnection of the flux surfaces takes place which leads to the formation of magnetic islands. In fact, in presence of this perturbation, the ideal magnetic island topology of nested flux surfaces breaks and the typical island structure forms on the $q = m/n$ resonant surface. In this way, the island structure can be seen as a closed helical flux tube closing on itself after going m times around the torus while going n times in the poloidal direction. Inside the island, each field line makes a large radial excursion, creating a shortcut for the radial transport of energy and particles. This effect is due to the presence of finite resistivity in small regions of the plasma, leading to the modification of magnetic field line topology which can only be explained within the context of the resistive MHD model [Freidberg(1987)]. The basic description of this phenomenon is carried out in a cylindrical configuration using a helical coordinate system, which follows the geometry of the perturbation. The modification of the equilibrium current of the system by the perturbation leads the so-called Classical Tearing Modes and their dynamics is described with the Rutherford Equation. In a toroidal configuration, on the other hand, new effects due to the geometry of the system arise, such as neoclassical transport processes or trapped particle orbits, which create other type of currents in the plasma, responsible for the so-called Neoclassical Tearing Modes. Their dynamics is described by a modified form of the Rutherford Equation, which takes into account these effects. Since Neoclassical Tearing Modes are actively controlled and stabilised with ECCD, the dynamics of the Neoclassical Tearing Mode during the stabilisation process is especially considered. In this chapter, first the topology of magnetic islands is reviewed and then the evolu-

tion of the magnetic island is described. The classical Rutherford equation and its modified version are introduced once neoclassical transport effects such as the presence of banana orbits and the bootstrap current are presented. The second part of the chapter deals with the modelling carried out in this work for the modified Rutherford equation mainly focusing on the physical issues which will be addressed in chapter 5 via comparison with the NTM stabilisation experiments.

2.1 Resistive MHD and magnetic reconnection

A magnetically confined plasma can be described as a conducting fluid. The magneto-hydro-dynamic MHD model is basically a combination of Maxwell's equations and conservation equations for the mass, the momentum and the energy in the fluid. The conservation law for energy can be substituted by the equation of state for the pressure and the momentum conservation is an extension of the Navier Stokes equation to magnetised fluid. The electromagnetic variables are the electric field $\vec{E}$, the magnetic field $\vec{B}$, and the current density $\vec{j}$. The fluid variables are the mass density ρ, the fluid velocity $\vec{v}$ and the pressure p. The term $\frac{d}{dt} = \frac{\partial}{\partial t} + \vec{v} \cdot \nabla$ is the convective derivative in the fluid. Since the electron mass is small $\frac{m_e}{m_i} << 1$ the momentum of the fluid is mainly carried by the ions. The single-fluid approach, for a hydrogen system, is based on the following assumptions: $n_i = n_e = n$, $\vec{v}_i = \vec{v}$, $\vec{j} = en(\vec{v}_i - \vec{v}_e)$ where $\vec{v}_i$ and $\vec{v}_e$ are the ion velocity and the electron velocity, respectively. In addition, we define a total pressure as $p = p_e + p_i$, where $p_e = k_B n_e T_e$ and $p_i = k_B n_i T_i$ are the electron and ion pressure respectively. In an ideal approach the resistivity η is neglected whereas in the resistive approach it is taken into account. In this case, the equations underlying the model are:

$$\frac{\partial \rho}{\partial t} + \nabla \cdot (\rho \vec{v}) = 0 \quad \text{(mass conservation)} \tag{2.1}$$

$$\rho \frac{d\vec{v}}{dt} = \vec{j} \times \vec{B} - \nabla p \quad \text{(momentum equation)} \tag{2.2}$$

$$\frac{d}{dt}\left(\frac{p}{\rho^\gamma}\right) = 0 \quad \text{(adiabatic equation)} \tag{2.3}$$

$$\vec{E} + \vec{v} \times \vec{B} = \eta \vec{j} \quad \text{(Ohm's law)} \tag{2.4}$$

$$\nabla \times \vec{E} = -\frac{\partial \vec{B}}{\partial t} \quad \text{(Faraday's law)} \tag{2.5}$$

$$\nabla \times \vec{B} = \mu_0 \vec{j} \quad \text{(Ampères's law)} \tag{2.6}$$

$$\nabla \cdot \vec{B} = 0 \quad \text{(absence of magnetic charges)} \tag{2.7}$$

The presence of finite resistivity η in equation 2.4 has important consequences on the magnetic field line structure since it leads to non-conservation of the magnetic flux (which is valid in the ideal MHD case). In particular, if the system is perturbed, the presence of finite resistivity allows the magnetic energy around a resonant layer to be released via the modification of the field line topology. This

process leads to the so-called magnetic reconnection phenomena which is shown schematically in figure 2.1.

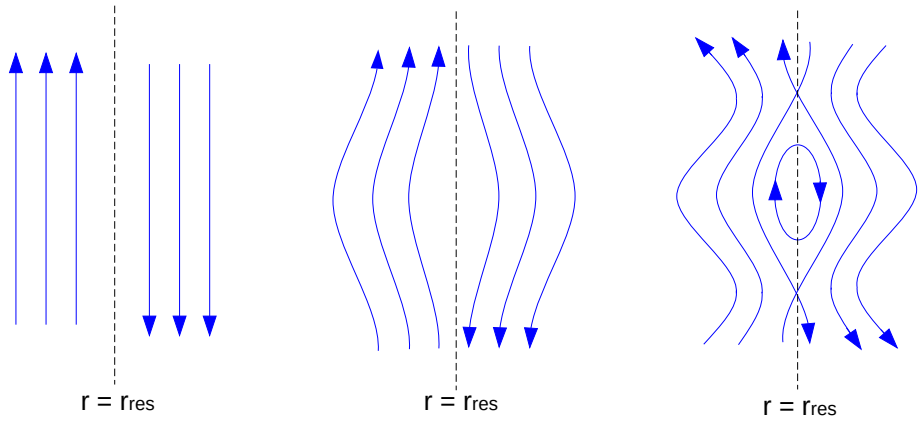

Figure 2.1: Formation of a magnetic island due to field line reconnection around a resonant layer in which plasma resistivity is not negligible: starting from an unperturbed system (left), a small perturbation near the rational surface (center) can lead to reconnection of the magnetic field lines (right).

2.2 The magnetic island topology

The study of the magnetic island topology and of the island evolution generally make use of the observation that a realistic toroidal description of the problem can be obtained by bending a cylinder into a torus as shown in figure 2.2. In this way a large aspect-ratio approximation $r/R << 1$ (that is $B_z^2 >> B_\theta^2$) can be adopted and a helical coordinate system (r,μ,η) together with the helical angle $\alpha = \theta - n/m\phi$ can be introduced. The distance from the resonant surface is defined as $x = r - r_{\rm res}$ and the poloidal angle θ remains unchanged as in the cylindrical coordinate system and the equilibrium magnetic field is independent of the poloidal angle θ. In presence of an island, the helical flux $\psi_{\rm hel}$ consists of an equilibrium part ψ_0, and a perturbation ψ_1:

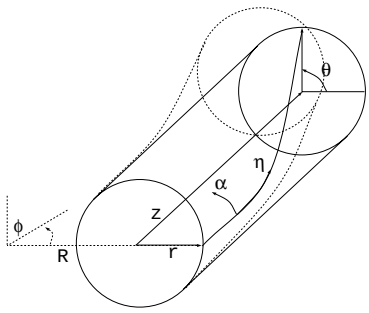

Figure 2.2: Approximation of a torus to a cylinder and helical angle α

$$\psi_{\rm hel}(r,\eta) = \psi_0(r) - \psi_1(r,\alpha) \tag{2.8}$$

where the equilibrium helical flux ψ_0 is assumed to depend only on the radial coordinate and is approximated to a parabola

$$\psi_0 = \psi_0(r_{\rm res}) + \frac{1}{2} B_{\theta 0} \frac{q'}{q} (r - r_{\rm res})^2 \tag{2.9}$$

centered at the resonant surface $r = r_{\rm res}$; this is obtained by Taylor expanding to the second-order equation of the helical magnetic field $B_{\rm hel}$[1] $\simeq B_{\theta 0}(1 - \frac{q(r)}{q_{\rm res}})$ at $r = r_{\rm res}$ and noticing that in general the shear rq'/q is a positive quantity. The

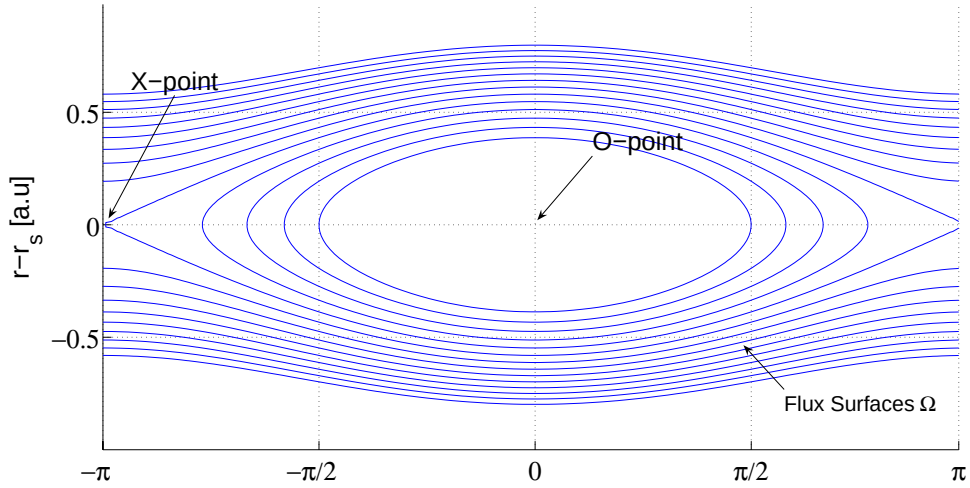

Figure 2.3: The magnetic island contours are defined via the the normalised flux function Ω, the center of the island is called O-point whereas the last closed surface is called the separatrix on which the magnetic field lines cross in the so-called X-point.

helical perturbation ψ_1 has the form $\psi_1(r,\alpha) = \psi_1(r)\cos\alpha$, assuming that only one harmonic of the perturbation is dominant. However, the radial component of the helical perturbation is assumed constant $\psi_1(r) = \psi_1 = const$, since far away from the resonant surface its effect is negligible compared to the effect of $\psi_0 \simeq (r - r_{\rm res})^2$. In general, magnetic islands are characterized by their width W, which is the maximum radial expansion of the island structure. The point where the minimum of the perturbation current flows is the island O-point whereas the point of where the maximum value of the disturbance current flows is the X-point as indicated in figure 2.3. The last closed surface is the separatrix. At the X-point of the island $r - r_{\rm res} = 0$ and $\alpha = -\pi, \pi$ so that $\psi_{\rm hel} = \psi_1$ whereas at the O-point of the island $r - r_{\rm res} = \frac{W}{2}$ and $\alpha = 0$ giving $\psi_{\rm hel} = \frac{1}{2}\frac{q}{q'}(\frac{W}{2})^2 - \psi_1$. By equating these two equations, the island width turns out to be proportional to the square root

[1] $B_{\rm hel} = \nabla\psi_{\rm hel} \times \hat{e}_\eta \simeq \nabla\psi_{\rm hel} \times \hat{e}_z$ and $(B_r, B_\mu, B_\eta) = (\frac{m}{r}\frac{\partial\psi_{\rm hel}}{\partial\alpha}, -\frac{\partial\psi_{\rm hel}}{\partial r}, 0)$

of the perturbation size and to the shear $\psi_0'' = q'/q$ at the resonant surface of the magnetic field $W = 4\sqrt{\frac{\psi_1}{\psi_0''}}$ which can be re-written in terms of magnetic field:

$$W = 4\sqrt{\frac{B_r q'}{q B_\theta}} \tag{2.10}$$

By dividing ψ_{hel} to ψ_1, the normalized flux surface Ω is introduced as

$$\Omega = 8\frac{(r - r_{\text{res}})^2}{W^2} - \cos\alpha \tag{2.11}$$

whose contours, shown in figure 2.3, depict two distincts type of curves: $\Omega = 1$ defines the separatrix of the island, $-1 < \Omega < 1$ defines flux surfaces inside the island and $\Omega > 1$ defines the flux surfaces outside the island. Because of the shape of the helical flux function, the magnetic island has a symmetrical shape.

2.2.1 Asymmetric island geometry

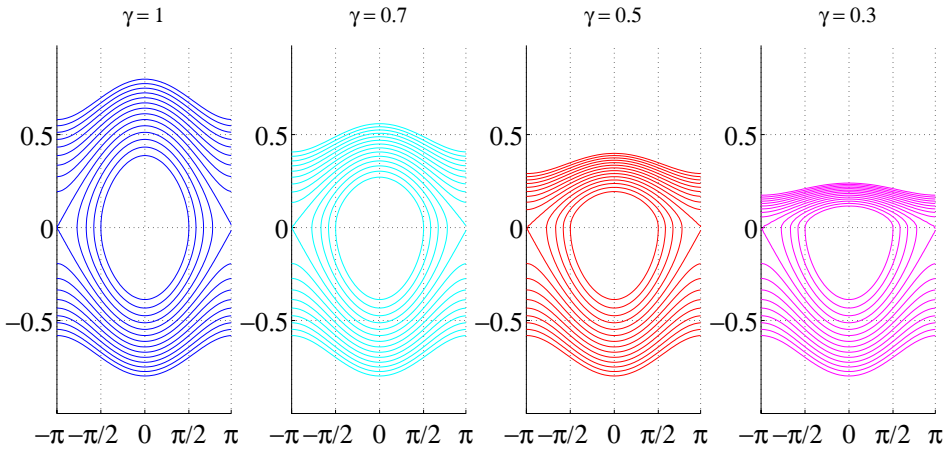

Figure 2.4: Shape of the modelled asymmetric island in dependance of the asymmetry factor γ: $\gamma = 1$ corresponds to a fully symmetrical island whereas for $\gamma = 0.7$, $\gamma = 0.5$ and $\gamma = 0.3$ the island shrinks on one side and becomes more and more asymmetrical.

Although most of the NTM studies are carried out assuming symmetrical islands, experimentally it is observed that magnetic islands have an asymmetric shape [Meskat(2001)] as figure 3.7 of chapter 3 shows. In this work, a simple model for describing an asymmetric island is used which defines the flux function Ω as:

$$\Omega = \begin{cases} \frac{8x^2}{W^2} - \cos\alpha \ \text{ if } \ x \leq 1 \\ \frac{8x^2}{\gamma^2 W^2} - \cos\alpha \ \text{ if } \ x > 1 \end{cases} \tag{2.12}$$

where the symmetry factor $\gamma < 1$ is introduced for 'shrinking' one side of the island as shown in figure 2.4. By introducing γ, the asymmetrical island W^* can be expressed in terms of the symmetrical island W using the relation:

$$W^* = \frac{W}{2}(1+\gamma) \tag{2.13}$$

2.3 The island evolution equation

The various types of currents flowing in the plasma (and its boundary) all influence the dynamics of magnetic islands. The natural stability of magnetic islands is determined by the equilibrium toroidal current profile. On the other hand, the evolution of magnetic islands is governed by the perturbed helical currents in the island region. In general, to describe the dynamics of a tearing mode in the plasma it is sufficient to apply the Ohm's law (equation 2.4) and the Ampére's law (equation 2.6) to the perturbed flux function ψ_1 along the magnetic field lines. Along the helical direction, in fact, due to the Ohm's law, an electric field E_η is induced associated with the changing in time of ψ_1:

$$\frac{\partial \psi_1}{\partial t} = E_\eta = \frac{1}{\sigma} j_\eta - (\vec{v} \times \vec{B})_\eta \tag{2.14}$$

and by assuming that in the resistive layer $(\vec{v} \times \vec{B})_\eta$ is negligible compared to $\frac{1}{\sigma} j_\eta$, ψ_1 results to vary in time because of the currents flowing along the helical magnetic field lines:

$$\frac{\partial \psi_1}{\partial t} = E_\eta = \frac{1}{\sigma} j_\eta \tag{2.15}$$

In addition, j_η can be evaluated making use of the the Ampére's law $(\nabla \times \vec{B})_\eta = \mu_0 j_\eta$ by integrating over the island width W:

$$\begin{aligned} \mu_0 j_\eta &= \frac{1}{W}(B_{1\mu}(r_{\text{res}} - W/2) - B_{1\mu}(r_{\text{res}} + W/2)) \\ &= \frac{1}{W}(\psi_1'(r_{\text{res}} - W/2) - \psi_1'(r_{\text{res}} + W/2)) = \frac{\psi_1}{W}\Delta'(W) \end{aligned} \tag{2.16}$$

By writing r in terms of Ω, by using 2.15 for a thin island and by isolating the $\cos\alpha$-Fourier component, the general form of the magnetic island evolution equation can be written as:

$$\psi_1 \Delta'(W) = \mu_0 \int_{-1}^{\infty} d\Omega \oint d\alpha \, j_\eta < \cos\alpha >_\Omega \tag{2.17}$$

where $< \cos\alpha >_\Omega$ is averaged over the flux function Ω with the flux averaging operator

$$< X(\Omega,\alpha) >_\Omega = \frac{\oint d\alpha \frac{X(\Omega,\alpha)}{\sqrt{\Omega+\cos\alpha}}}{\oint d\alpha \frac{1}{\sqrt{\Omega+\cos\alpha}}} \tag{2.18}$$

The parameter Δ' ('delta prime'), which appears in equation 2.17, is defined as

$$\Delta' = \frac{\frac{d\psi_1}{dr}|_{r_{res}+\frac{W}{2}} - \frac{d\psi_1}{dr}|_{r_{res}-\frac{W}{2}}}{\psi_1} \tag{2.19}$$

and it defines the radial jump of the magnetic field perturbation $B_{1\mu}$ across the resistive layer where magnetic field lines reconnect [Rutherford(1973)]. It is a direct measure for the total perturbed parallel current within the island as one can interpret Δ' as a measure for the free energy available in the plasma to drive a tearing mode; in fact, the change of magnetic energy in the presence of an island is given by [Hegna(1994)]:

$$\delta W_{mag} = -\frac{1}{4} r_{res} \psi_1^2 \Delta' \tag{2.20}$$

so that a positive Δ' means that the plasma is in a lower, more favourable energy state. The value of Δ' is a property of the plasma equilibrium (toroidal current profile) and has to be evaluated by matching the ideal MHD solution for ψ_1 for the region $0 < r < r_{res} + \frac{W}{2}$ to the solution for $r_{res} - \frac{W}{2} < r < \infty$ which in general will give a jump in $\frac{d\psi_1}{dr}$. In cylindrical geometry, the perturbed flux ψ_1 is calculated with the tearing mode equation [Furth(1963)]:

$$\frac{d^2\psi_1}{dr^2} + \frac{1}{r}\frac{d\psi_1}{dr} - \left(\frac{m^2}{r^2} + \frac{dj/dr}{B_\theta(r)(1 - nq(r)/m)} \right) \psi_1 = 0 \tag{2.21}$$

whose solution is shown in figure 2.5. This equation must be in general solved numerically for a given current profile $j(r)$ and value of $q(a)$ to determine Δ'.

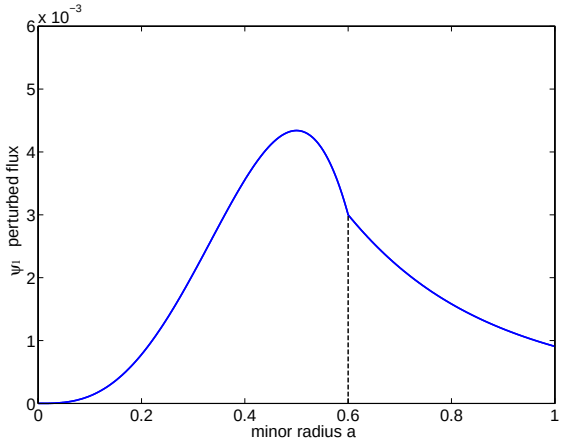

Figure 2.5: Solution of equation 2.21 for finding the perturbed flux ψ_1 in cylindrical geometry: the kick present at 0.6 a indicates the region of discontinuity at the resonant surface due to magnetic reconnection.

2.4 The 'classical' Rutherford equation

Equation 2.17 tells us how much current is flowing in the island but does not directly reveal how the island evolves in time. The time evolution only becomes evident if the mechanisms responsible for the perturbed parallel current j_η are specified. In the case of the classical tearing modes only the contribution of the Ohmic current is determining the evolution of the island that is $j_\eta = j_{\mathrm{Ohm}}$. In this case, the island evolution equation 2.17 reduces to the classical Rutherford equation for the island evolution [Rutherford(1973)]:

$$\frac{\tau_s}{r_{\mathrm{res}}}\frac{dW}{dt} = r_{\mathrm{res}}\Delta'(W) \tag{2.22}$$

where $\tau_s = \frac{\mu_0 r_{\mathrm{res}}^2}{1.22\eta_{\mathrm{NC}}}$ is the resistive time and 1.22 is the numerical integration factor obtained when integrating equation 2.15. In this case, a positive Δ' means a growing island as expected from the interpretation of Δ' as the available free energy. If Δ' is negative, the island is naturally stable; no island will develop. For small islands, Δ' is usually considered independent of W, so that the Rutherford equation predicts unstable islands to grow exponentially. In case of larger islands (W in the order of a), instead, the toroidal current distribution is considerably altered and hence a dependence of Δ' on W is expected which can be approximated by writing:

$$\Delta'(W) = \Delta'_0\left(1 - \frac{W}{W_{\mathrm{sat}}}\right) \tag{2.23}$$

where W_{sat} is the saturated island width (which can be experimentally determined).

2.5 Transport in a torus: banana orbits and the bootstrap current

In a toroidal plasma configuration, effects due to toroidicity modify both the particle and the heat transport properties of the plasma. In this case, transport is called 'neoclassical' in contrast to the 'classical' transport effects in a cylindrical plasma. In fact, what characterises transport in a torus is the presence of classes of passing and trapped particles due to the poloidal nonuniformity of the magnetic field ($B \propto \frac{1}{R}$). The trapped particles on the outer side of the torus, exhibit banana orbits as shown in figure 2.6 of typical width $W_b = \epsilon^{1/2}\rho_{\mathrm{pi}}$. These are typically several centimeters wide for ions where

$$\rho_{\mathrm{pi}} = \frac{v_{\mathrm{th}}}{\omega_{\mathrm{ci}}} = \frac{\sqrt{2m_i kT_i(r_{\mathrm{res}})}}{eB_{\mathrm{pol}}(r_{\mathrm{res}})} \tag{2.24}$$

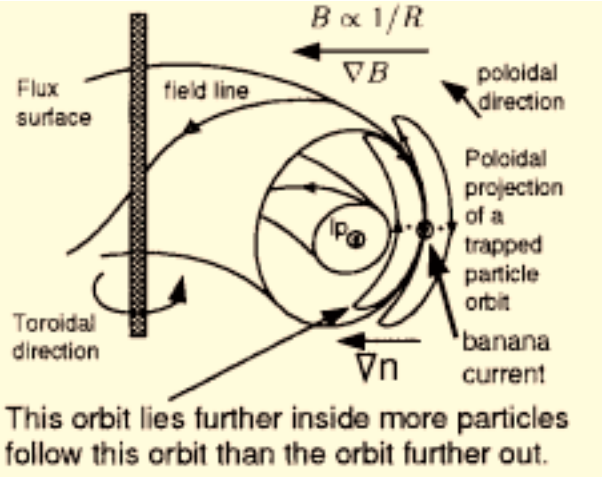

Figure 2.6: Physical mechanism for the bootstrap current generation

is the ion poloidal gyroradius for a given ion temperature T_i and mass m_i and with about $\epsilon^{1/2}$ of the particles which are being trapped into such orbits. In addition, a toroidal plasma is characterised by the presence of the so-called bootstrap current. The bootstrap current arises from the differences in diffusion and momentum exchange between electrons and ions and passing and trapped particles. The heuristic derivation [Peeters(2000)] of the bootstrap current density j_{BS} carried by passing electrons can be obtained by considering the electron charge $-e$ times the fraction of trapped particles $\epsilon^{1/2}$ times the typical parallel velocity $\epsilon^{1/2} v_{\mathrm{th}}$ where v_{th} is the thermal speed times the difference in electron density across the banana width $W_b \frac{dn}{dr}$ times a 'frictional' factor for passing electrons colliding with ions and trapped electrons $\nu_{\mathrm{ee}} / \epsilon \nu_{\mathrm{ei}} \approx \epsilon^{-1}$. This results in:

$$j_{\mathrm{BS}} \approx 1.46 \frac{\epsilon^{1/2}}{B_{\mathrm{pol}}} \frac{p}{L_p} \tag{2.25}$$

where

$$\frac{1}{L_p} = \frac{1}{L_n} + \frac{1}{L_T} \tag{2.26}$$

and

$$L_n = \frac{n}{\nabla n}, L_T = \frac{T}{\nabla T} \tag{2.27}$$

are the gradient length scales involved for density and temperature where $\nabla n = \frac{dn}{dr}$ and $\nabla T = \frac{dT}{dr}$ are the spatial derivatives for density and temperature respectively. The bootstrap current density turns out to be proportional to the pressure

gradient (more precisely the dependency on the density gradient ∇n is a factor 2 larger than on the temperature gradient ∇T [Perkins(2003)]); it increases with larger plasma pressure and can become a significant fraction of the total parallel current density j_{tot} at high β. For example, for $\beta_N = 2$ it is of the order $j_{\mathrm{BS}} / j_{\mathrm{tot}} \approx 20\%$.

2.6 The modified Rutherford equation

In case of neoclassical tearing modes, the induced ohmic current j_{Ohm} is not the only one contributing to the perturbed parallel current j_η: other currents which flow in the island region alter the evolution equation and need to be taken into consideration such that $j_\eta = j_{\mathrm{Ohm}} + j_{\mathrm{other}}$. The main currents which are known to affect the island evolution are the bootstrap current j_{BS}, the current generated by tokamak curvature j_{PS}, the polarisation current j_{pol} and the externally injected current j_{ECCD}. Therefore, a modified Rutherford equation having the form

$$\frac{\tau_s}{r_{\mathrm{res}}}\frac{dW}{dt} = r_{\mathrm{res}}\Delta'(W) + r_{\mathrm{res}}\Delta'_{\mathrm{BS}} + r_{\mathrm{res}}\Delta'_{\mathrm{GGJ}} + r_{\mathrm{res}}\Delta'_{\mathrm{pol}} + r_{\mathrm{res}}\Delta'_{\mathrm{ECCD}} \tag{2.28}$$

is built up starting from equation 2.17 as an extension of equation 2.22 where each Δ'-term is introduced to describe each of these additional currents affecting the evolution of magnetic islands. [2]

2.6.1 Δ': modification of the equilibrium current profile

As already mentioned in section 2.3, the parameter Δ' is introduced to quantify the radial jump across the resistive layer of the magnetic field and to link it to the perturbation current which enhances the growth of the tearing mode via the Ampére's law. It arises when matching the inner and outer solutions of the tearing mode equation 2.21. For a pure classical tearing mode, it has to be positive for the mode to be unstable. In the case of neoclassical NTMs, instead, the Δ' can also be negative, that is a system which is unstable to NTMs, does not necessarily have to be unstable to classical tearing modes. A rough estimate of the value of Δ' can be obtained assuming the perturbed flux ψ_1 to be exponentially decaying in the vacuum region at the edge of the plasma ($\psi_1 \approx \frac{1}{r^m}$) which is valid especially for large values of m. In this case, the value for Δ' which is obtained:

$$r_{\mathrm{res}}\Delta' = \frac{\frac{d\psi_1}{dr}|_{r_{\mathrm{res}+}} - \frac{d\psi_1}{dr}|_{r_{\mathrm{res}-}}}{\psi_1} = -2m \tag{2.29}$$

[2] the effect of j_{PS} has been first investigated by Greene, Glasser, Johnson. Therefore, the Δ'-term referring to it has the subscript GGJ

However, based on numerical simulations, the value

$$r_{\rm res}\Delta' = -m \tag{2.30}$$

is considered to be more realistic. In both cases, equations 2.30 and 2.29 have to be considered as very much simplified approximations just indicating the Δ' to be negative in case of neoclassical tearing modes. In the simulations, which will be presented in chapter 5 and 7, in case of a (3,2) NTM island a more precise fit [Yu(2004)] which has been used is:

$$r_{\rm res}\Delta' = -1.97\frac{r_{\rm res}}{a}(1+23.1\frac{W}{a}) \tag{2.31}$$

which is calculated using a non-linear cylindrical code which solves the MHD equations and includes the bootstrap current in equation 2.4. For a (2,1) NTM island $r_{\rm res}\Delta' = -m$ has been initially adopted and successively, for some cases, in order to get consistent results between (3,2) NTMs and (2,1) NTMs a value of $r_{\rm res}\Delta'$ has been set which is closer to $r_{\rm res}\Delta' = -1$. One would expect that since the (2,1) NTM is closer to the vacuum than the (3,2) NTM, equation 2.29 should apply. On the other hand, given the uncertainty in the estimation of Δ' (the Δ' is usually determined using numerical codes built on a cylindrical geometry which do not take into account toroidal effects at all) and considering the more unstable nature of the (2,1) NTMs, it seems also reasonable to have a scenario in which Δ' is closer to being positive (>0) and therefore is less stabilising for the mode.

2.6.2 $\Delta'_{\rm BS}$: missing of the bootstrap current inside the island

The main mechanism which underlies the growth of the NTMs is related to the fact that when the pressure gradient flattens in the island region due to enhanced transport of particles and heat towards the edge of the plasma, it leaves a 'hole' in the bootstrap current profile since, as already mentioned in section 2.5, the bootstrap current is proportional to the pressure gradient ($j_{\rm BS} \propto dp/dr$). For negative $\frac{dp}{dr} < 0$ and positive shear $\frac{dq}{dr} > 0$, this current perturbation opposes the induced current $j_{\rm Ohm}$ in the island and, therefore, it is destabilising and this is the reason why even islands with negative $\Delta' < 0$ can be destabilised. The bootstrap term at large island size is modelled as follows [Fitzpatrick(1995)]:

$$r_{\rm res}\Delta'_{\rm BS} = 9.25\sqrt{\epsilon}\frac{\beta'}{s}\frac{r_{\rm res}}{W} \tag{2.32}$$

By substituing $\beta' = -(\frac{q}{\epsilon})^2\frac{\mu_0 r_{\rm res}p'}{B_z^2}$, $B_z = \frac{qRB_\theta}{r}$ and $L_p = \frac{p}{p'}$ it becomes:

$$r_{\rm res}\Delta'_{\rm BS} = 4.63 r_{\rm res}\sqrt{\epsilon}\beta_{\rm p}\frac{L_q}{L_p}\frac{1}{W} \tag{2.33}$$

and by using equation 2.25 to express j_{BS} one gets:

$$r_{\mathrm{res}}\Delta'_{\mathrm{BS}} = 6.34 r_{\mathrm{res}}\mu_0 L_q \frac{j_{\mathrm{BS}}}{B_\theta}\frac{1}{W} \tag{2.34}$$

Equation 2.34 suggests that whenever the Δ'_{BS} dominates over the Δ', the island growth rate may always be positive. In addition, by considering the saturated phase (when $dW/dt = 0$), one can get a first estimate of the saturated island size W_{sat} as $W_{\mathrm{sat}} \approx \frac{\Delta'_{\mathrm{BS}}}{\Delta'}$ and observe that in the large island limit the following linear scaling is valid:

$$W_{\mathrm{sat}} \propto \beta_p \propto j_{\mathrm{BS}} \tag{2.35}$$

However, equation 2.34 does not fully consistently describe the experimental findings: the W^{-1} dependence would always imply the existence of destabilised NTMs whereas experimentally it is observed that NTMs are destabilised only above a certain threshold island width. So a 'seeding' island W_{seed} of sufficient width is needed. Seeding islands can be provided by any coincidental distortion of the plasma, for instance by the error field of a sawtooth precursor, fishbone or some turbulence. One physical mechanism which can explain this threshold at small island physics is provided by considering that incomplete flattening of the pressure profile inside the magnetic island can occur below a critical width W_d [Fitzpatrick(1995)] when perpendicular transport $\chi_\perp$ across the (small) island dominates over parallel transport $\chi_\parallel$:

$$W_{\mathrm{d}} = 5.1\sqrt{\frac{R_{\mathrm{maj}}L_q q}{m}}\left(\frac{\chi_\perp}{\chi_\parallel}\right)^{1/4} \tag{2.36}$$

Above this critical island width, in fact, the electron temperature can be considered a flux function. In equation 2.36, several quantities are used which are defined as follows:

- $\chi_{Sp} = \frac{26.4\sqrt{\pi}T_e^{5/2}\epsilon_0^2}{2m_e\epsilon^{3/2}ln\Lambda n_e}$ is the Spitzer conductivity from the classical transport theory [Wesson(1997)]
- $L_\parallel = \frac{R_{\mathrm{maj}}L_q}{4nW}$ is the so-called connection length [Meskat(2001)]
- $\chi_\perp = \chi_{GB} = \frac{3.25\sqrt{T_i}}{B_T^2}\frac{1}{a}\frac{\sqrt{A}}{Z^2}$ is the Gyro-Bohm model for perpendicular heat conductivity [3]
- $\chi_\parallel = \frac{\chi_{Sp}}{\sqrt{1+(3.16\frac{380}{L_\parallel})}}$ is the modified parallel heat conductivity [Meskat(2001)]

[3] the transport scaling is gyro-Bohm, i.e., local ion heat diffusivity scales as $\chi_{\mathrm{GB}} \propto \frac{\rho_{\mathrm{pi}}}{a}\chi_B$ where $\chi_B \sim cT/eB$

By considering the limit to the modified parallel heat conductivity, the values calculated with the formula 2.36 agree well with the experimental observation that $W_d \approx 2-3$ cm. An other physical mechanism which affects the small island physics is provided by those particles which drift inside the banana orbits and therefore give a contribution to the increase of the bootstrap current inside the island [Poli(2002)]. This is significant when the island width W is of the order of the banana width W_{b} which has been introduced in section 2.5 and whose formula is repeated here:

$$W_b = \epsilon^{1/2}\rho_{\mathrm{pi}} \tag{2.37}$$

Therefore, by taking these two mechanisms into account at small island width the Δ'_{BS} term is corrected and becomes:

$$r_{\mathrm{res}}\Delta'_{\mathrm{BS}} = r_{\mathrm{res}}\frac{6.34}{2}\mu_0 L_q \frac{j_{\mathrm{BS}}}{B_{\mathrm{pol}}}\left(\frac{W}{W^2+W_d^2}+\frac{W}{W^2+28W_b^2}\right) \tag{2.38}$$

2.6.3 Δ'_{GGJ}: effect of the tokamak curvature

The effects of magnetic field curvature can be stabilising for neoclassical tearing modes as first pointed by Glasser, Greene and Johnson [Glasser(1975)] so that it is often called the GGJ effect and it is indicated as Δ'_{GGJ} in the modified Rutherford equation. The magnetic island associated to the NTM bends or curves the field lines in such a way to increase magnetic energy; in terms of currents affecting the evolution of the mode, this effect can be seen as related to the so-called Pfirsch-Schlüter current, which also depends on the pressure gradient $j_{\mathrm{PS}} \propto \frac{dp}{dr}$ [Wesson(1997)] and which, for a typical pressure profile $\frac{dp}{dr} < 0$, is enhanced and exerts a stabilising effect on the NTM. Large aspect-ratio approximation predicts that $\Delta'_{GGJ} \approx D_R / W$ which has the same W^{-1} dependence as the bootstrap term. In toroidal geometry the resistive interchange parameter D_R [Shafranov(1967)] is approximated as $D_R = -\frac{2p'(1-q^2)q^2}{rB_z^2 q'^2}$ and it results to be a factor $(\epsilon/q)^2$ smaller the Δ'_{BS} term. The curvature term is only dominant at small island width and it depends on the pressure profile, hence to the β. In particular, there is an island width thereshold provided by the W_d island below which the pressure and curvature dominate over Δ' [Lütjens(2001)]. Therefore, the following form for the Δ'_{GGJ} is used in the modified Rutherford equation:

$$r_{\mathrm{res}}\Delta'_{\mathrm{GGJ}} = \frac{\mu_0 r_{\mathrm{res}} D_R}{\sqrt{W^2+0.65W_d^2}} \tag{2.39}$$

2.6.4 Δ'_{pol}: effect of the polarisation current

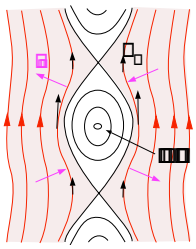

An other current which affects the island evolution equation is the so-called polarisation current which is a consequence of different response to a rotating island of ions and electrons [Smolyakov(2004)]: in fact, if one considers an island propagating at frequency ω in the frame of plasma flow, a time varying field results since the electrons respond faster to this electric field than do the ions, thus a polarisation current j_{pol} results. It is still very much under debate whether this current is stabilising or destabilising since it depends on the sign of ω. Both theoretical calculation and experimental measurements of ω are difficult and in general a simplified (stabilising) form for this term has been taken by modelers:

$$\Delta'_{\mathrm{pol}} \approx r_{\mathrm{res}}\beta_p\left(\frac{L_q}{L_p}\rho_{\mathrm{pi}}\right)^2\frac{1}{W^3} \tag{2.40}$$

In case of the polarisation term, the threshold for the magnetic island width to grow is given by:

$$W_{\mathrm{pol}} \approx \left(\frac{L_q}{L_p}\right)^{1/2} W_b \tag{2.41}$$

2.6.5 Δ'_{ECCD}: effect of externally applied current for stabilisation

As it will be shown in more detail in chapter 4, during an NTM stabilisation experiment Electron Cyclotron Current Drive (ECCD) is injected in the magnetic island present in the plasma in order to replace the missing bootstrap current with EC driven current. The modelling of the externally applied current to counteract the loss of j_{BS} inside the island follows the same approach as the other terms included in the Modified Rutherford Equation (using equation 2.17 and inserting in it a current density contribution to j_η). The effect of injecting an external current in the island region has been modeled in a cylindrical approximation as [Giruzzi(1999)]:

$$\Delta'_{ECCD} = \frac{16\Delta'}{nsq_a}\frac{I_{\mathrm{ECCD}}}{I_p}\frac{a^2}{W^2}\eta_{\mathrm{ECCD}} \tag{2.42}$$

where m and n are the poloidal and toroidal mode number, q_a is the safety factor at the plasma surface, $s = r_{\mathrm{res}}\frac{q'}{q}$ is the shear on the resonant surface. By using equation 2.29, the poloidal current expressed as $I_{\mathrm{p}} = \frac{2\pi r_{\mathrm{res}}}{\mu_0}B_\theta$, the ECCD current $I_{\mathrm{ECCD}} = 2\pi^{3/2}r_{\mathrm{res}}\frac{d}{2}j_{\mathrm{ECCD}}$ and the full deposition width d at $\frac{1}{e}$ of the injected gaussian profile, equation 2.42 takes the form

$$r_{\mathrm{res}}\Delta'_{\mathrm{ECCD}} = -32\mu_0 r_{\mathrm{res}}L_q\sqrt{\pi}\frac{d}{2}\frac{j_{\mathrm{ECCD}}}{B_\theta}\frac{1}{W^2}\eta_{\mathrm{ECCD}} \tag{2.43}$$

This term is describing only the effect due to the injection of the ECCD current flowing in the helical direction (the (m,n) component).

2.6.6 The efficiency function η_{ECCD}

In equation 2.43 the function η_{ECCD} is introduced to model the efficiency of the ECCD injection in stabilising the NTM. The η_{ECCD} function is defined in such a way that it is 1 in case the injected current is a δ-function injected in the O-point of the island. The ECCD current can be injected as a continuous (DC) current (plotted in figure 2.7) or a modulated (AC) one in phase with the rotation of the O-point of the island. The η_{ECCD} is determined by averaging the ECCD current

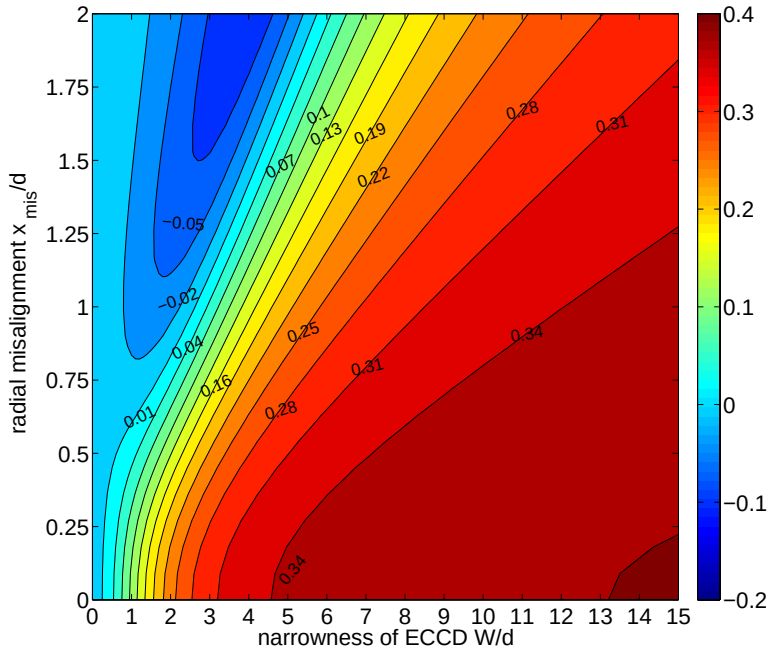

Figure 2.7: η_{ECCD} function characterising the efficiency of ECCD current injection for continuous case (DC) plotted versus $\frac{W}{d}$ and normalised radial misalignment x_{mis}/d: for $\frac{W}{d} >> 1$ and $\frac{x_{\mathrm{mis}}}{d} = 0$ the $\eta_{\mathrm{ECCD}} = constant \sim 0.37$ whereas for larger values of x_{mis} it can even become negative indicating destabilisation.

density written in the form

$$j_{\mathrm{ECCD}} = j_{\mathrm{ECCD},0}\, e^{-C(\frac{x-x_{\mathrm{mis}}}{d})^2} \tag{2.44}$$

with $x = r - r_{\mathrm{res}}$ and $x_{\mathrm{mis}} = r_{\mathrm{dep}} - r_{\mathrm{res}}$, $C = 4\ln 2$ and $j_{\mathrm{ECCD},0}$ is calculated from the total ECCD current I_{ECCD}.

The analytical formula for the η_{ECCD} is [Hegna and Callen(1997)]:

$$\eta_{\mathrm{ECCD}} = \frac{\int_{-1}^{\infty} d\Omega S(\Omega) J(\Omega)}{\int_{-1}^{\infty} d\Omega J(\Omega)} \tag{2.45}$$

where the functions $S(\Omega)$ and $J(\Omega)$ are in case of a symmetrical island:

$$S(\Omega) = \oint d\alpha \frac{\cos\alpha}{\sqrt{\Omega + \cos\alpha}} \tag{2.46}$$

$$J(\Omega) = \frac{\oint d\alpha M(\tau) \frac{j_{\mathrm{ECCD},0} e^{-C(x-x_{\mathrm{mis}})^2/d^2}}{\sqrt{\Omega+\cos\alpha}}}{\oint d\alpha \frac{1}{\sqrt{\Omega+\cos\alpha}}} \tag{2.47}$$

and the integration extends from:

$$\begin{array}{cc} -\pi < \alpha < \pi & \text{for } \Omega > 1 \text{ (outside the island)} \\ -\cos^{-1}(-\Omega) < \alpha < \cos^{-1}(-\Omega) & \text{for } -1 < \Omega < 1 \text{ (inside the island)} \end{array}$$

The quantity $S(\Omega)$ accounts for the projection of the current injected in the island which allows for the island to develop whereas $J(\Omega)$ is the flux surface averaged current source. $M(\tau)$ describes the modulation of the source with τ being the fraction of a period the source is on. In case of 50% modulation, the injected power P_{ECRH} is halved in comparison with the case of continous injection and this is a major benefit in terms of minimisation of the P_{ECRH} injected for NTM stabilisation. However, in this work, mainly experiments with continuous injection have been analysed since for modulation a very limited database has been available. The difference between DC injection and modulated one is dominant when $\frac{W}{d} < 1$ due to the functional difference ($\approx \frac{W}{d}$ versus $\approx (\frac{W}{d})^2$) between modulation and continuous injection which favours the modulated scenario in terms of efficiency. On the other hand, when $\frac{W}{d} >> 1$ and $x_{\mathrm{mis}} = 0$, both modulated and continuous injection efficiencies tend to a constant value which is at around $\sim 0.35 \div 0.4$. In the case of a large misalignment, the η_{ECCD} can become negative (and therefore destabilising) as figure 2.7 shows.

2.6.7 The efficiency function η_{ECCD} for an asymmetrical island

To evaluate the efficiency function in case of an asymmetrical island determined by the relation 2.13 and whose orbits are described by equation 2.12 the integrals present in equation 2.45 have to be computed in two distinct regions 1 and 2

where the symmetric / asymmetric shape is assumed respectively, e.g:

region 1	$0 < \alpha < \pi$	for $\Omega > 1$ (outside the island)
	$0 < \alpha < \cos^{-1}(-\Omega)$	for $-1 < \Omega < 1$ (inside the island)
region 2	$-\pi < \alpha < 0$	for $\Omega > 1$ (outside the island)
	$-\cos^{-1}(\Omega) < \alpha < 0$	for $-1 < \Omega < 1$ (inside the island)

In this case $S(\Omega)$ has two contributions which can be summed up together as:

$$\begin{aligned} S(\Omega) &= S_1(\Omega) + S_2(\Omega) = \\ &= (\frac{1}{\gamma} + 1) \oint d\alpha \frac{\cos\alpha}{\sqrt{\Omega + \cos\alpha}} \end{aligned}$$

whereas the flux-averaged function $J(\Omega)$ in case of an asymmetrical island is the current flowing in region 1 and region 2 normalised over the arc length of the island which is $d\alpha = d\alpha_1 + d\alpha_2$ so that $J(\Omega)$ reads:

$$\begin{aligned} J(\Omega) &= \frac{\int_1 j_{\mathrm{ECCD}} d\alpha + \int_2 j_{\mathrm{ECCD}} d\alpha}{\int_1 d\alpha + \int_2 d\alpha} \qquad (2.48) \\ &= \frac{M(\tau) j_{\mathrm{ECCD},0} \left(\int_1 d\alpha \frac{e^{-C(\frac{W}{d})^2 (\sqrt{\frac{\Omega+\cos\alpha}{8}} - \frac{x_{\mathrm{mis}}}{W})^2}}{\sqrt{\Omega + \cos\alpha}} + \int_2 d\alpha \frac{e^{-C(\frac{W}{d})^2 (\gamma\sqrt{\frac{\Omega+\cos\alpha}{8}} - \frac{x_{\mathrm{mis}}}{W})^2}}{\gamma\sqrt{\Omega + \cos\alpha}} \right)}{(\frac{1}{\gamma} + 1) \oint d\alpha \frac{1}{\sqrt{\Omega+\cos\alpha}}} \end{aligned}$$

The efficiency of the ECCD injection expressed by the η_{ECCD} is expected to be smaller in case of an asymmetrical island. To clarify this statement, it is useful to consider the simplified case in which the island and the ECCD beam are perfectly aligned: for a symmetric island rotating with respect to the ECCD beam, the current will always be injected by the same amount inside the island no matter on which side of the island it faces; on the other hand for an asymmetric island, some of the current which is injected on the smaller side will be lost compared to the symmetric case and therefore ECCD will be less efficient. As far as the difference between continuous injection and modulation is concerned, it is expected that because during modulation the ECCD beam is in phase with the O-point of the island, the difference between symmetrical and asymmetrical case is less prominent that in the continuous injection case. The results of the integration for η_{ECCD} considering an asymmetric island with $\gamma = 0.5$ are plotted in figure 2.8. In order to consistently compare the η_{ECCD} for different values of γ the island width W for the asymmetric case ($\gamma < 1$) needs to be re-scaled by a factor $\frac{1+\gamma}{2}$. In the case of an asymmetrical island, η_{ECCD} is smaller than in the symmetric case by a factor 2 and 1.2 in the range $\frac{W}{d} \leq 1$ for continuous and modulated injection respectively. On the other hand, this difference disappears for $\frac{W}{d} >> 1$.

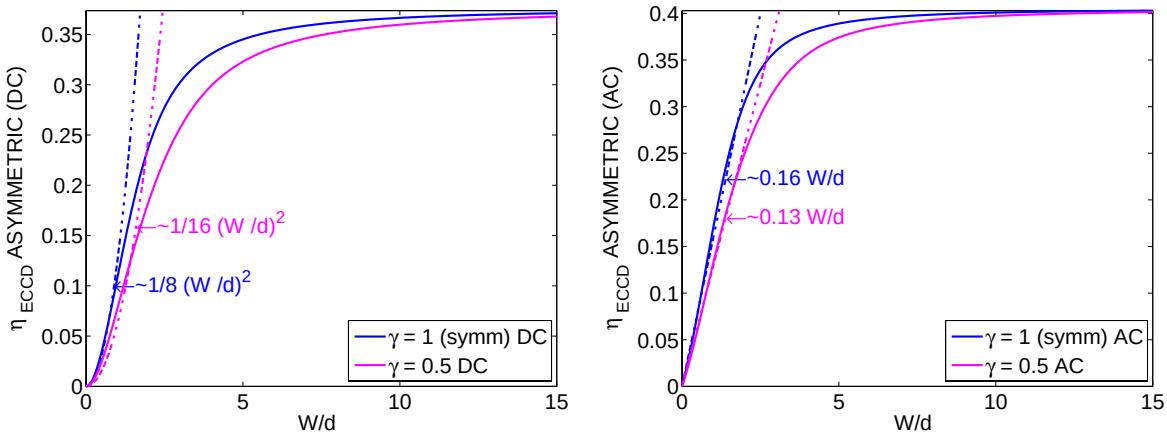

Figure 2.8: Behaviour of the efficiency function η_{ECCD} for $\gamma = 1$ (symmetric island) and $\gamma = 0.5$ with perfect alignment $x_{\mathrm{mis}} = 0$ in the case of continuous injection (left) and 50% modulation (right). The η_{ECCD} decreases if the island is asymmetric. However for $\frac{W}{d} >> 1$ this effect tends to be less prominent and $\eta_{\mathrm{ECCD}} \rightarrow 0.3 \div 0.4$ for both the cases $\gamma = 0.5$ and $\gamma = 1$. In the range $\frac{W}{d} \leq 1$ the analytical limits for η_{ECCD} are $\approx 0.16\frac{W}{d}$ for modulation and $\approx \frac{1}{8}(\frac{W}{d})^2$ for continuous injection for a symmetric island. In this range η_{ECCD} decreases when assuming an asymmetrical island with $\gamma = 0.5$ by roughly a factor 2 and 1.2 for continuous and modulated injection respectively.

2.7 The modelling of Modified Rutherford Equation

In order to model NTM stabilisation experiments, a Modified form of the Rutherford equation is proposed in this work which includes the terms:

1. the Δ' (equation 2.31 or 2.30) which is a stabilising term
2. the Δ'_{BS} (equation 2.38) which is the main destabilising term
3. the Δ'_{GGJ} (equation 2.39) which is a stabilising term mainly relevant at small island width
4. the Δ'_{ECCD} (equation 2.43) which describes the stabilising external injection of the ECCD beam inside the island to counteract the loss of bootstrap current.

By considering the physics which is included in these terms, some characteristic features of this model can be already envisaged. In particular,

- the threshold island W_{seed} allowing the NTM to grow will be of the order of some averaged value between W_d and W_b

- the W_{sat} will be $W_{sat} \sim \frac{\Delta'_{BS}+\Delta'_{GGJ}}{\Delta'}$
- the stabilisation term Δ'_{ECCD} will take into account the mere helical (m,n) component of the ECCD injected current.

In this model, for the sake of simplicity, some physical mechanisms are intentionally not included such as the polarisation term Δ'_{pol}, which is not taken into account because of its high uncertainty, the additional stabilising effect of the local heating of the ECCD [Hegna and Callen(1997)] and the stabilising effect of the (0,0) component of j_{ECCD} [Pletzer and Perkins(1999)]. As far as the Δ'_{pol} is concerned, the type of analysis which will be carried out in the following chapters does not intrinsically require a clear discrimination between the different seeding processes allowing for the NTM evolution; as far as the additional stabilising effects of ECCD are concerned, instead, there is experimental evidence that effects due to heating are small [LaHaye(2006)] whereas the stabilising effect of the (0,0) component of j_{ECCD} is only modelled for thin islands ($\frac{W}{d} << 1$) which is not fully consistent with the experimental set-up of a real experiment. However, neglecting these terms implies that the results for NTM stabilisation will have to be considered as upper limits of the possible power requirements predictions. The coefficients in the terms 2.31, 2.34, 2.39 and 2.43 have been derived in cylindrical geometry with large aspect-ratio expansion and, therefore, for realistic comparison with the experiments, the model for the Modified Rutherford Equation proposed in this work introduces two fitting parameters c_{sat} and c_{stab} to account for deviations mainly due to the geometry and other physics possibly not covered in the modeled terms. In particular, the coefficient c_{sat} is introduced in front of the β-dependent terms $\Delta'_{BS} + \Delta'_{GGJ}$ and the coefficient c_{stab} is introduced in front of the Δ'_{ECCD} term. Considering these assumptions, the Modified Rutherford Equation studied in this work has the following form:

$$\begin{aligned}\frac{\tau_s}{r_{res}}\frac{dW}{dt} &= -1.97\frac{r_{res}}{a}\left(1+23.1\frac{W}{a}\right) \\ &+ \mathbf{c_{sat}}\left[r_{res}\frac{6.34}{2}\mu_0 L_q \frac{j_{BS}}{B_{pol}}\left(\frac{W}{W^2+W_d^2}+\frac{W}{W^2+28W_b^2}\right)-\frac{r_{res}6.35\mu_0 D_R}{\sqrt{W^2+0.65W_d^2}}\right] \\ &- \mathbf{c_{stab}}32\sqrt{\pi}\mu_0 r_{res}L_q\frac{j_{ECCD}}{B_{pol}}\frac{d}{2}\frac{\eta_{ECCD}}{W^2}\end{aligned} \tag{2.49}$$

The coefficients c_{sat} and c_{stab} can be determined from analysing NTM stabilisation experiment as described in detail in chapter 4 and chapter 5. If the physics included in equation 2.49 is enough complete to describe the experimental observations, these coefficients are expected to be of the order of unity and are expected to be independent from the size and the parameters of the different devices.

2.8 The Modified Rutherford Equation and its phase diagram

The Modified Rutherford Equation 2.49 is a non-linear equation which can, at first, be solved analytically. The behaviour of the stationary solutions can be studied by setting the growth rate $\frac{dW}{dt}$ to zero and solving the resultant for the island width W in dependance of the β and by considering the phase diagram (W, $\frac{dW}{dt}$) as the one plotted in figure 2.9. Usually, the island associated to the NTM grows till it reaches its saturated value W_{sat}. The marginal value after which the mode naturally decays away is reached either by ramping down the sustaining power (NBI) and lowering the β_p till it gets to the marginal value $\beta_{\mathrm{p,marg}}$ or by injecting ECCD current till it gets to the $\beta_{\mathrm{p,marg,ECCD}}$ value. In both cases, as the marginal island width W_{marg} (related to $\beta_{\mathrm{p,marg}}$) or $W_{\mathrm{marg,ECCD}}$ (related to $\beta_{\mathrm{p,marg,ECCD}}$) is reached the mode is to be considered stabilised. The model (2.49) can be simpli-

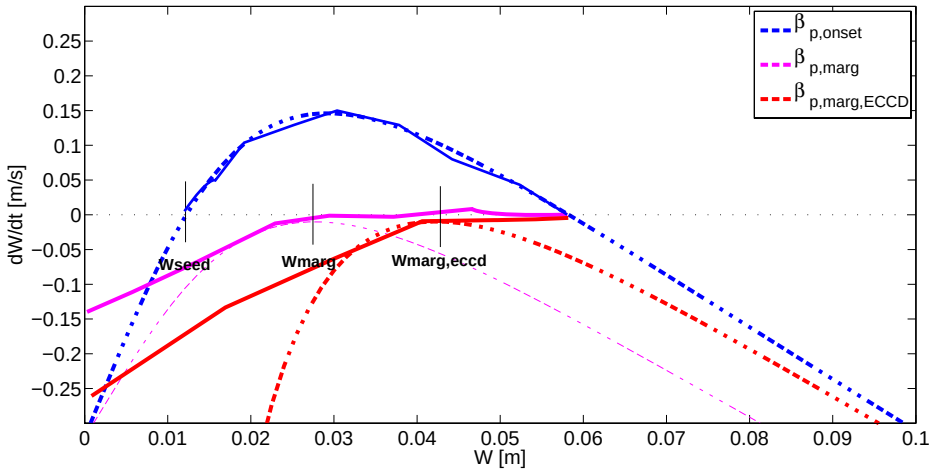

Figure 2.9: Phase diagram of the magnetic island width evolution and its stationary points: the NTM starts to grow ($dW/dt > 0$) as a wide enough seed island W_{seed} forms in the plasma at a certain value of β_p indicated as $\beta_{\mathrm{p,onset}}$ (blue curve). The solid lines sketch the typical time evolution of an NTM during the experiment, while these curves move with the evolution of β_p.

fied in order to study the characteristics of the stable and unstable solutions of the MRE which affect the evolution of the NTM as shown in figure **??**. Due to the large error bars in the experimental measurements it is not possible to discriminate between the dominating small island width effects in the MRE, so that to simplify (2.49) we choose to neglect the W_{b} term (usually W_{d} is 2-3 times bigger than W_{b}) and the curvature term Δ'_{GGJ}. In this way, (2.49) can be written in terms of β_{p} as:

$$\frac{\tau_s}{r_{\mathrm{res}}}\frac{dW}{dt} = -c_1 + c_2\beta_{\mathrm{p}}\frac{W}{W^2+W_{\mathrm{d}}^2} - c_3\frac{1}{W^2} \tag{2.50}$$

where $c_1 = r_{\rm res}\Delta'$, $c_2 = r_{\rm res}\sqrt{\epsilon}L_q/L_p$ and $c_3 = 16\sqrt{\pi}dL_q j_{\rm ECCD}\frac{\mu_0 r_{\rm res}}{B_{\rm pol}}\eta_{\rm ECCD}$ are abbreviations for the local quantities present in the $r_{\rm res}\Delta'$, $r_{\rm res}\Delta'_{\rm BS}$ and $r_{\rm res}\Delta'_{\rm ECCD}$ term respectively and $c_{\rm sat}$ and $c_{\rm stab}$ are set to 1. In order to analytically recover the solutions of (2.50), the functions f and g are defined:

$$f(W) = -c_1 + c_2\frac{\beta_{\rm marg}W}{W^2+W_{\rm d}^2} \tag{2.51}$$

$$g(W) = -c_1 + c_2\frac{\beta_{\rm marg}W}{W^2+W_{\rm d}^2} - \frac{c_3}{W^2} \tag{2.52}$$

and the derivative over W is carried out:

$$f'(W) = c_2\beta_{\rm marg}\frac{-W^2+W_{\rm d}^2}{(W^2+W_{\rm d}^2)^2} \tag{2.53}$$

$$g'(W) = c_2\beta_{\rm marg}\frac{-W^2+W_{\rm d}^2}{(W^2+W_{\rm d}^2)^2} + \frac{2c_3}{W^3} \tag{2.54}$$

f and g are equation (2.50) with no ECCD and with ECCD term, respectively. Marginal stabilisation obtained by simply lowering the β (ramp-down experiments) is given by the conditions $f = 0$ and $f' = 0$ for $W = W_{\rm marg}$:

$$f(W_{\rm marg}) = -c_1 + c_2\frac{\beta_{\rm marg}W_{\rm marg}}{W_{\rm marg}^2+W_{\rm d}^2} = 0 \tag{2.55}$$

$$f'(W_{\rm marg}) = c_2\beta_{\rm marg}\frac{-W_{\rm marg}^2+W_{\rm d}^2}{(W_{\rm marg}^2+W_{\rm d}^2)^2} = 0 \tag{2.56}$$

On the other hand, marginal stabilisation obtained by injecting ECCD current fulfills the conditions $g = 0$ and $g' = 0$ for $W = W_{\rm marg,ECCD}$:

$$g(W_{\rm marg,ECCD}) = -c_1 + c_2\frac{\beta_{\rm marg,ECCD}W_{\rm marg,ECCD}}{W_{\rm marg,ECCD}^2+W_{\rm d}^2} - \frac{c_3}{W_{\rm marg,ECCD}^2} = 0 \tag{2.57}$$

$$g'(W_{\rm marg,ECCD}) = c_2\beta_{\rm marg,ECCD}\frac{-W_{\rm marg,ECCD}^2+W_{\rm d}^2}{(W_{\rm marg,ECCD}^2+W_{\rm d}^2)^2} + \frac{2c_3}{W_{\rm marg,ECCD}^3} = 0 \tag{2.58}$$

From (2.55) and (2.56) the following relations between the marginal island width $W_{\rm marg}$, $W_{\rm d}$ and $\beta_{\rm mrg}$ are obtained:

$$W_{\rm marg} = W_{\rm d} \tag{2.59}$$

$$c_1 = \frac{\beta_{\rm marg}}{2W_{\rm marg}c_2} \tag{2.60}$$

These describe the natural decay of the mode as the β_p drops. On the other hand, a third solution $W_{\rm marg,ECCD}$, to which $\beta_{\rm p,marg,ECCD}$ corresponds, is found when

the ECCD term is taken into account. In fact, from (2.58) the following relation can be recovered:

$$c_3 = -\frac{\beta_{\text{marg,ECCD}} W^3_{\text{marg,ECCD}}}{2} \frac{W^2_{\text{marg}} - W^2_{\text{marg,ECCD}}}{(W^2_{\text{marg}} + W^2_{\text{marg,ECCD}})^2} c_2 \tag{2.61}$$

By substituting (2.59) and (2.61) in (2.57) one obtains:

$$c_2\left(-\frac{\beta_{\text{marg}}}{2W_{\text{marg}}} + \frac{\beta_{\text{marg,ECCD}} W}{W^2_{\text{marg}} + W^2_{\text{marg,ECCD}}} + \frac{\beta_{\text{marg,ECCD}} W_{\text{marg,ECCD}}(W^2_{\text{marg}} - W^2_{\text{marg,ECCD}})}{(W^2_{\text{marg}} + W^2_{\text{marg,ECCD}})^2}\right) = 0 \tag{2.62}$$

Since $c_2 \neq 0$, the term into brackets of (2.62) has to be zero and the relation between β_{marg} and $\beta_{\text{marg,ECCD}}$ can be recovered:

$$\frac{\beta_{\text{marg,ECCD}}}{\beta_{\text{marg}}} = \frac{(W^2_{\text{marg}} + W^2_{\text{marg,ECCD}})^2}{W_{\text{marg}} W_{\text{marg,ECCD}}} \frac{1}{3W^2_{\text{marg}} + W^2_{\text{marg,ECCD}}} \tag{2.63}$$

Equation (2.63) can be re-written in a more compact form as:

$$\beta_0 = \frac{(W_0^2 + 1)^2}{W_0(W_0^2 + 3)} \tag{2.64}$$

by defining $\beta_0 = \beta_{\text{marg,ECCD}} / \beta_{\text{marg}}$ and $W_0 = W_{\text{marg,ECCD}} / W_{\text{marg}}$. The resulting function is plotted in figure 2.10 using the typical local ASDEX Upgrade parameters for (3,2) NTM $c_1 = -3$, $r_{\text{res}} = 0.24$ m, $B_{\text{pol}} = 0.28$ T, $L_p = -0.3$ m, $\epsilon = 0.14$, $d = 0.03$ m, $W_{\text{d}} = 0.025$ m and $\eta_{\text{ECCD}} = 0.4$. Equation (2.64) indicates that if no ECCD has to be applied, the marginal island size is $W_{\text{marg,ECCD}} = W_{\text{marg}}$ and consequently $\beta_{\text{p,marg,ECCD}} = \beta_{\text{p,marg}}$. But if j_{ECCD} is injected, since $c_3 > 0$, $W_{\text{marg,ECCD}} > W_{\text{marg}}$ and therefore $\beta_{\text{p,marg,ECCD}} > \beta_{\text{p,marg}}$. The result is quite general and device-dependent parameters are not necessary. On the other hand, device-dependent parameters affect the degree of increment of β_0. This implies that during a stabilisation experiment with ECCD, saturated islands need to be reduced to a value $W_{\text{marg,ECCD}}$ which is larger than the marginal island W_{marg}. The function for estimating how much $\beta_{\text{marg,ECCD}}$ changes with respect to β_{marg} when j_{ECCD} is injected for partial stabilisation, instead, can be obtained from (2.60) and (2.61) as:

$$\beta_0 = \frac{c_3}{c_1} \frac{1}{W^2_{\text{d}}} \frac{W_0^2 + 1)^2}{(W_0^2 - 1) W_0^3} \tag{2.65}$$

In contrast to (2.64), β_0 depends on c_3 and therefore the amount of j_{ECCD} injected is not univocally determined.

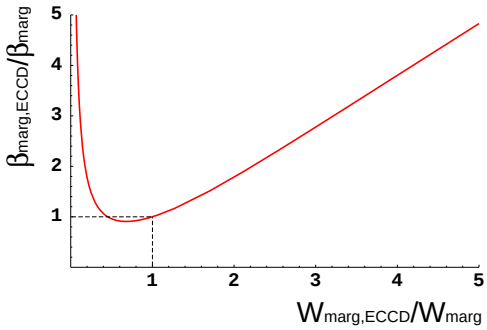

Figure 2.10: The marginal island width and the marginal β value with ECCD are larger than those without ECCD

2.8.1 Power requirements limits for the stabilisation of NTMs

Additional information can be gained by the modelled Rutherford equation 2.49 when written in the form [Zohm(2007)]:

$$\frac{\tau_s}{r_{res}}\frac{dW}{dt} = r_{res}\Delta' + c_{sat}6.34 r_{res}\frac{\mu_0 L_q}{B_\theta} j_{BS} f_{GGJ}\frac{1}{W} - c_{stab}32\sqrt{\pi}\frac{\mu_0 r_{res} L_q}{B_\theta}\frac{d}{2} j_{ECCD}\eta_{ECCD}\frac{1}{W^2}$$

This form of equation 2.49 neglects the small island terms and parametrises the curvature term with $f_{GGJ} = 1 - 1.37(\frac{q^2-1}{q^2})L_q\frac{(r_{res})^{1/2}}{R^{3/2}}$. Therefore, studying the properties of equation 2.66 provides the upper limits for the power requirements for the stabilisation in terms of the fitting parameters c_{sat} and c_{stab}. The requirement for complete stabilisation can be obtained by setting equation 2.66 to zero and dividing it by the Δ'_{BS} term. In this way one obtains:

$$-\frac{W}{W_{sat}} + 1 - 5.05\sqrt{\pi}\frac{c_{stab}}{f_{GGJ}c_{sat}}\frac{d}{W}\frac{j_{ECCD}}{j_{BS}}\eta_{ECCD} = 0 \qquad (2.66)$$

where $W_{sat} = \Delta'_{BS}/\Delta'$ has been used. In the case of small deposition profile experiments $d << W_{marg}$ and therefore, both for modulation and continuous drive, $\eta_{ECCD} \sim 0.4$. In this case, the root of equation 2.66 is such that by postulating unconditional stability the following condition has to be fulfilled:

$$\frac{d}{W_{sat}}\frac{j_{ECCD}}{j_{BS}} > \frac{1}{14} f_{GGJ}\frac{c_{sat}}{c_{stab}} \qquad (2.67)$$

On the other hand, when $d > W_{marg}$, the η_{ECCD} behaves differently in case of modulation and continuous injection. For the modulated case, as figure 2.8 shows $\eta_{ECCD} \sim 0.16\frac{W}{d}$ whereas for the continuous case $\eta_{ECCD} \sim \frac{1}{8}(\frac{W}{d})^2$ for a symmetrical island or $\eta_{ECCD} \sim 0.13(\frac{W}{d})$ and $\eta_{ECCD} \sim \frac{1}{16}(\frac{W}{d})^2$ for an asymmetrical island with $\gamma = 0.5$. Since in ITER a relatively high-β will be achieved such that

$W_{sat} >> W_{marg}$, by applying also this assumption, the figure of merit for modulation which is obtained is:

$$\frac{j_{ECCD}}{j_{BS}} > 0.7 f_{GGJ} \frac{c_{sat}}{c_{stab}} \quad \text{SYMMETRICAL ISLAND} \tag{2.68}$$

$$\frac{j_{ECCD}}{j_{BS}} > 0.9 f_{GGJ} \frac{c_{sat}}{c_{stab}} \quad \text{ASYMMETRICAL ISLAND} \tag{2.69}$$

whereas in the case of continuous injection, it becomes:

$$\frac{j_{ECCD}}{j_{BS}} > 0.9 f_{GGJ} \frac{c_{sat}}{c_{stab}} \frac{d}{W} \quad \text{SYMMETRICAL ISLAND} \tag{2.70}$$

$$\frac{j_{ECCD}}{j_{BS}} > 1.8 f_{GGJ} \frac{c_{sat}}{c_{stab}} \frac{d}{W} \quad \text{ASYMMETRICAL ISLAND} \tag{2.71}$$

In the design of the ITER ECCD system for NTM stabilisation the figure of merit $\Lambda = j_{ECCD}/j_{BS}$ has been adopted and in particular the value $\Lambda = \frac{j_{ECCD}}{j_{BS}} > 1.2$ [Pletzer and Perkins(1999)] has been used as requirement for complete stabilisation in case of modulation and $\Lambda = \frac{j_{ECCD}}{j_{BS}} > 1.6$ in case of continuous injection. In our case, the figure of merit obtained by using the modelled Rutherford equation 2.49 ranges between $0.6 < \frac{j_{ECCD}}{j_{BS}} < 0.8$ for 50% modulation and between $0.8 < \frac{j_{ECCD}}{j_{BS}} < 1.6$ in case of continuous injection when assuming $f_{GGJ} \sim 0.9$, $c_{sat}/c_{stab} \sim 1$ and considering as lower and upper boundary the symmetrical and asymmetrical case respectively.

Chapter 3

Measurements

The comparison between the experimental behavior of NTM during the stabilization experiments with ECCD and the theoretical model provided by equation 2.49 requires the determination of many different plasma quantities . These can be either measured directly from the experiment or can be calculated a posteriori with tools such as numerical codes and specific softwares. In this chapter, the tools and the techniques used to measure the parameters needed for the analysis which follows are presented both for ASDEX Upgrade and JT-60U tokamaks. In general, the measured quantities need to be obtained in the core of the plasma $0 < r/a < 0.8$ where the NTMs develop; nevertheless, in this work, edge measurements are also considered mainly for consistency as they do not have a direct impact on the results. For two (3,2) NTM discharges (#18036 with $\beta_N \sim 2.2$ for ASDEX Upgrade and #41666 with $\beta_N \sim 1.5$ for JT-60U) the profiles which have been measured and used for the analysis are presented. In each plot the measured quantities are normalised in a way to be able to compare them in terms of machine independent parameters since if $q(r)$ and $\beta_p(r)$ are the same the NTM physics is expected to be the same (leading to the same fitting coefficients c_{sat} and c_{stab}). At the edge of the plasma the following relation is approximately valid:

$$q_{95} = s\frac{a^2 B_T}{R_{\text{maj}} I_p} \tag{3.1}$$

where s is a numerical factor indicating how different the plasma shape is among the discharges. By accounting for this relation, it is useful to normalise the magnetic field B_{pol} and the bootstrap current density j_{BS} by the factors $\frac{a}{R_{\text{maj}}}\frac{B_T}{q_{95}}$ and $\frac{B_T}{R_{\text{maj}} q_{95}}$ respectively; the resistivity η_{NC}, on the other hand, can be normalised to $\frac{T_e^{3/2}}{Z_{\text{eff}}}$ where T_e is the local value of the electron temperature profile since, as it will be shown later in the chapter, it depends on $\frac{Z_{\text{eff}}}{T_e^{3/2}}$. In each plot the dotted vertical lines indicate the mode position at which the local value needed in equation

2.49 has been taken which are $r/a \sim 0.49$ for #41666 and $r/a \sim 0.51$ for #18036 respectively. In general, for fitting the free coefficients c_{sat} and c_{stab} the plasma quantities which need to be measured are the following:

1. the kinetic profiles: the electron density n_e ($n_i \approx n_e$ is assumed), the electron temperature T_e, the ion temperature T_i and their gradient lengths L_{ne}, L_{Te},L_{Ti}
2. the safety factor profile q and its gradient length L_q
3. the saturated magnetic island width W_{sat} and its radial position in the plasma r_{res}
4. the experimental magnetic island evolution $W(t)$
5. the toroidal magnetic field B_T and the local poloidal magnetic field B_{pol}
6. the bootstrap current density j_{BS}
7. the ECCD current density j_{ECCD} and the deposition width d
8. the neoclassical resistivity η_{NC}

However, before determining these quantities, the plasma equilibrium for each discharge has to be taken into account and a proper mapping between the flux surfaces and the natural coordinates of each diagnostic needs to be done.

3.1 Plasma equilibrium reconstruction and mapping

In a tokamak, the plasma equilibrium is determined in terms of poloidal magnetic flux ψ by solving the so-called Grad-Shafranov (GSE) equation [Freidberg(1987)]:

$$-\Delta^* \psi = \mu_0 R^2 p'(\Psi) + FF'(\Psi) \tag{3.2}$$

where the pressure p and the poloidal current F are functions of ψ alone. The Grad-Shafranov equation is a non-linear elliptic PDE which is solved by specifying the functions $p = p(\psi)$ and $F = F(\psi)$, together with boundary conditions or externally imposed constraints on ψ, and then inverting equation 3.2 to determine the flux surfaces $\psi = \psi(R,z) = const.$ For ASDEX Upgrade, equilibrium reconstruction is carried out using CLISTE. The CLISTE code [McCarthy(1999)] finds a numerical solution to the Grad-Shafranov equation 3.2 for a given set of poloidal field coil currents and limiter structures by varying the free parameters in the parameterisation of the $p'(\psi)$ and $FF'(\psi)$ source profiles which define the toroidal current density profile j_ϕ so as to obtain a best fit in the least squares

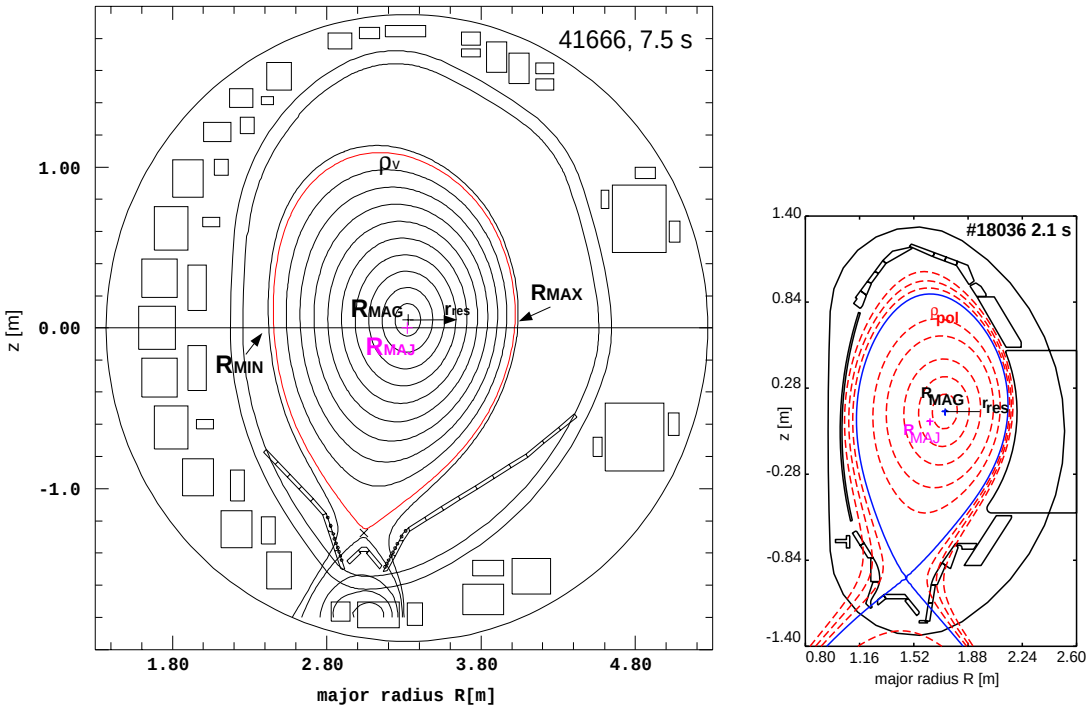

Figure 3.1: Plasma equilibrium at JT60 (left) and ASDEX Upgrade (right) for two of the considered discharges: for similar aspect ratio R_{maj}/a, the plasma is slightly more elongated for the ASDEX Upgrade case and has a smaller triangularity

sense to a set of experimental measurements. In the case of the present analysis, the experimental measurements have included external magnetic data and kinetic data [McCarthy(2001)] from AUGPED (described in section 3.3.7) and for one discharge (#22186) also data available from MSE diagnostic (described in section 3.3.6). In addition, the safety factor on axis has been constrained to $q = 1$, since in the considered discharges there is evidence of the presence of sawteeth or fishbones. For JT-60U discharges, equilibrium reconstruction is carried out in a similar way, using FBEQU equilibrium solver [Azumi(1980)] which accounts for the magnetic signal for the boundary conditions at the edge and which constraints $q = 1$ in the core of the plasma. The coordinate system which is commonly used at ASDEX Upgrade and which is used on most profile plots is $\rho_{\mathrm{pol}} = \sqrt{\frac{\psi-\psi_0}{\psi_s-\psi_0}}$, where ψ_0 is the flux at the magnetic axis and ψ_s is the value of ψ at the separatrix (last closed surface). The normalization is such that $\rho_{\mathrm{pol}} = 0.0$ at the magnetic axis and $\rho_{\mathrm{pol}} = 1.0$ at the separatrix. At JT-60U, on the other hand, the mapping quantity mostly used is $\rho_v = \sqrt{\frac{V}{2\pi R_{\mathrm{maj}}}}$ with $\rho_v = 0$ at the magnetic axis and $\rho_v = 1.0$ at the separatrix. The square root, in both cases, is introduced to transform the resulting coordinate, which is about proportional to the cylindrical volume, to a more linear behavior across the radius. The minor radius a, the major radius R_{maj}, the radius at the resonant surface of the NTM r_{res} and the inverse aspect-ratio ϵ

are calculated as follows:

$$a = \frac{R_{\max} - R_{\min}}{2} \tag{3.3}$$

$$R_{\mathrm{maj}} = \frac{R_{\max} + R_{\min}}{2} \tag{3.4}$$

$$r_{\mathrm{res}} = r_N = R - R_{\mathrm{MAG}} \tag{3.5}$$

$$\epsilon = \frac{r_{\mathrm{res}}}{R_{\mathrm{MAG}}} \tag{3.6}$$

where R_{MAG} is the radius at magnetic axis, $R_{\max}$ and $R_{\min}$ are the major radius at the high field side of the plasma (HFS) and at the low field side (LFS) of the plasma at the midplane, r_N is the so-called $r_{Neuhauser}$ coordinate with R being the major radius of the intersection of the corresponding flux surface where the NTM is sitting with a horizontal line through the magnetic axis on the LFS. In figure 3.1, the similar plasma shapes used for NTM stabilisation experiments at ASDEX Upgrade and JT-60U are plotted and the above mentioned coordinates are indicated. As mentioned in the introduction, ASDEX Upgrade and JT-60U are characterised by very similar aspect ratio ($R_{\mathrm{maj}}/a = 3.3$ and $R_{\mathrm{maj}}/a = 3.1$ respectively). In the case shown in figure 3.1, the elongation k of the plasma is higher at ASDEX Upgrade ($k \approx 1.7$ versus $k \approx 1.6$) with a smaller triangularity δ at the separatrix compared to JT-60U ($\delta \approx 0.04$ versus $\delta \approx 0.17$). A mapping between $\rho_{\mathrm{pol}} \leftrightarrow a$ and $\rho_v \leftrightarrow a$ has been applied to ASDEX Upgrade and JT-60U respectively and consequently to the coordinate r_N.

3.2 Poloidal magnetic field B_{pol} and toroidal magnetic field B_T

The poloidal magnetic field B_{pol} is the averaged value over each flux surface and is calculated with the cylindrical formula:

$$B_{\mathrm{pol}} = \sqrt{B_z^2 + B_R^2} \tag{3.7}$$

where B_r and B_z are calculated from CLISTE using the flux matrix ψ given by :

$$B_R = -\frac{1}{R}\frac{\partial \psi}{\partial z} \qquad B_z = \frac{1}{R}\frac{\partial \psi}{\partial R}$$

As figure 3.2 shows, the profile shape at the edge is quite different for JT-60U and ASDEX Upgrade. This is mainly due to the fact that the bootstrap current flowing in the plasma is especially influencing the total toroidal current at the edge for a higher pressure gradient p'. As it will be addressed in the following sections, the ASDEX Upgrade kinetic profiles are systematically more peaked at the edge than

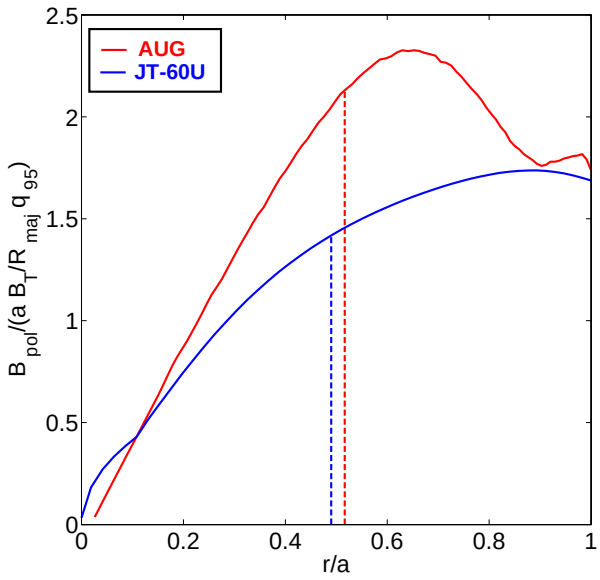

Figure 3.2: Typical poloidal magnetic field profile B_{pol} normalised to $\frac{a}{R}\frac{B_T}{q_{95}}$ for JT-60U (#41666 with $\beta_N \sim 1.5$) and ASDEX Upgrade (#18036 with $\beta_N \sim 2.2$). The dotted lines indicate the local value measured at the resonant surface position of the NTM. The ASDEX Upgrade profile has a more peaked shape towards the edge than the JT-60U one due to the typically steeper pressure profiles in this region at ASDEX Upgrade which affect the bootstrap current contributing to the total current profile shape.

at JT-60U and, therefore, the diamagnetic effects at the edge become more evident as in the case of B_{pol}. The value of toroidal magnetic field B_T, instead, is taken at the magnetic axis R_{MAG} and measured from the current I_{TF} in the toroidal field coils.

3.3 Kinetic profiles: T_e, T_i, n_e

3.3.1 Electron Cyclotron Emission (ECE)

The ECE diagnostic determines electron temperatures by radiometry of electron cyclotron emission from the fusion plasma. Hot electrons in the plasma gyrate around field lines with cyclotron frequency $\omega_c = \frac{eB}{m}$, where e is the elementary charge, B the magnetic field, and m_e the electron mass. At the 2^{nd} harmonic of the electron cyclotron frequency, the plasma usually emits locally like a blackbody source as long as optical thickness is sufficiently high. Then the intensity of the cyclotron radiation is a direct measure of electron temperature given by :

$$I(\omega) = \frac{\omega^2 T_e}{8\pi^2 c^2} \tag{3.8}$$

Since the magnetic field (and consequently the emission frequency $f = 2\pi\omega_c$) depends on the radius, the power spectrum represents a radial electron temperature profile. A limit to this diagnostic which can affect high density discharges is due to the high density limit which leads to a cut-off condition. In fact, in the case of second harmonic absorption, a critical electron density can be reached

$$n_{\mathrm{crit}}^{X2} = 1.94 \cdot 10^{19} \cdot B^2 \left[m^{-3}T^{-2}\right] \tag{3.9}$$

such that the accessibility of the resonant location from the outside of the plasma is blocked. In this case the emission in the cut-off density interval drops to a low value and the measurement is not representative for T_e anymore. At ASDEX Upgrade, the ECE diagnostics provides the electron temperature over the whole plasma cross-section with a time resolution of approximately 32 kHz. The radial resolution of each channel is about 0.01 m and the distance between the channels is 0.01-0.03 m [Suttrop(1996)]. At JT-60U the ECE diagnostics is equipped with 48 channels having a temporal resolution of 20 μs and a spatial one of 1.2 cm [Isayama(2001)].

3.3.2 Thomson scattering diagnostic

Standard laser scattering measurements are based on Thomson scattering of monochromatic light on free electrons. The geometry is chosen in such a way that the wave vector $k = k_i \perp k_s$ (where subscript i denotes the incident and s the scattered radiation) satisfies $k\lambda_D \gg 1$ (λ_D is the Debye-shielding length) and thus the light is scattered on uncorrelated free electrons. With a Maxwellian velocity distribution characterized by the temperature T_e of the electrons, a continuous spectrum around the primary laser frequency

$$I_s \propto \sqrt{\frac{m_e}{2\pi T_e}} n_e e^{-m_e\omega^2/(2k^2T_e)} \tag{3.10}$$

is observed from which the electron temperature can be derived. The scattering intensity I_s is proportional to the number of scattering centers and therefore to the electron density. This diagnostics therefore gives local information about electron density and temperature. In this work, it has been used for determining both electron density and temperature profiles at JT-60U and electron density profiles at ASDEX Upgrade. ASDEX Upgrade is equipped with a Thomson system featuring 16 vertical channels with 5-6 YAG laser beams each which acquire a full radial profile ($\Delta R = 3 - 4$ cm) every 8.3 ms [Murmann(1992)]. At JT- 60U the Thomson scattering system consists of a Ruby Laser system with spatial resolution of 22 mm with measurements obtained every 0.02-2 s and a YAG laser system which consists of 14 spatial measuring points in the plasma available every 0.2 ms [Yoshida(1999)].

3.3.3 Lithium beam diagnostic

The principle of the lithium beam diagnostic is based on the injection of a collimated beam of neutral Li-atoms directed to the plasma axis. Beam energy and electron density in the plasma determine the penetration depth. With energies of some 10 KeV it is of order of 2-5 cm. In electronic collision the beam atoms are excited

$$Li(E_0) + e^- \rightarrow Li* + e^- \tag{3.11}$$
$$Li* = Li(2p) \rightarrow Li(2s) + \hbar\omega \tag{3.12}$$

and the intensity of the resonance line (670.8 nm) from 2p to 2s transition is being detected perpendicular to the beam. Arrays of detectors allow for the simultaneous observation along the beam. The intensity reflects almost directly the electron density, which can be determined in this way in the edge region of the plasma. In this work, this diagnostic has ben used for fitting density profiles at ASDEX Upgrade. In ASDEX Upgrade the time resolution is usually restricted to several milliseconds for one profile due to insufficient signal-to-noise ratio. The spatial resolution of about 5 mm is determined by the fiber optics used to transfer the emitted light to the photomultipliers for acquisition of the emission profile [Fischer(2008)].

3.3.4 Interferometry diagnostic

A method for electron density measurements which is widely used is the laser interferometry. Its functioning principle is based on the fact that the refractive index depends on the electron density via the plasma frequency. The measurement is done by comparing the optical path difference between a microwave signal through the plasma and one through free space which can easily be deduced from the phase difference of the two signals given the following relation:

$$\phi = \frac{2\pi}{\lambda}\int_{z1}^{z2}(N_V - N(z))dz \propto \int_{z1}^{z2} n(z)dz \text{ for } \omega >> \omega_p \tag{3.13}$$

The integral quantity determined in this way is the line density $[m^{-2}]$ which requires deconvolution algorithms to be converted into profile information $[m^{-3}]$. In this work, interferometer data is used in both machines as an additional consistency check for the profiles of electron density measured by the Thomson scattering diagnostic. At ASDEX Upgrade, a far-infrared (DCN) laser interferometer is used with a time resolution of 300 μs and sampling rate of 10-20 kHz for measuring the line integrated electron densities along several horizontal and vertical lines of sight [McCormick(1997)]. At JT-60U a FIR laser interferometer and CO2 laser interferometer are used with a time resolution of 5 ms and 5 μs- 1 ms respectively [Kawano(1996)], [Fukuda(1989)].

3.3.5 Charge Exchange Recombination Spectroscopy (CXRS)

The CXRS diagnostic makes use of the line emitted by impurity carbon ions that undergo a charge exchange reaction with the neutral particles of the Neutral Beam Injectors (NBI). Therefore, CXRS is only available when NBI is on. The Doppler-width of the spectral line at wavelength λ emitted in the de-excitation process then reflects the ion temperature of the plasma bulk ions since the system can be considered to be in thermal equilibrium. In this work, the CXRS diagnostics has been used to measure ion temperatures both at ASDEX Upgrade and at JT-60U. At ASDEX Upgrade, the ion temperature profile is measured with the core diagnostics CEZ and CHZ (the first is focused on source 3 of the NBI and the second on source 8 of the NBI). It is available with a resolution $\Delta t \sim 50ms$, $\Delta r \sim 3-4$ cm [Meister(2001)]. At JT-60U it is available when source 14 of NBI is on and it is characterised by a spatial resolution of 0.8 / 1.5 cm every 16.7 ms [Koide(2001)].

3.3.6 Motional Stark effect diagnostic (MSE)

The motional Stark effect (MSE), which measures the internal local poloidal magnetic field, is an important method for the determination of the total current density j_{TOT}. The MSE diagnostic relies on the splitting of the high energy (60 keV) neutral beam Balmer line (D), as a result of the strong motional $E = v \times B$ electric field produced in the rest frame of the neutral deuterium atoms. Since Deuterium exhibits a linear and thus very strong Stark effect, compared to the Zeeman-effect, the line spectrum is dominated by the motional stark effect. At ASDEX Upgrade a 10-channel MSE diagnostic [Wolf(1997)], using the modulation technique and observing one of the 2.5 MW, 60 keV neutral ion heating beams is in use. The diagnostic measures the direction of polarization of the emitted radiation to determine the magnetic field pitch angle , with a resolution of 3 ms. The measured MSE polarisation angles are included in the equilibrium reconstruction which allows the number of free parameters of the inferred current or q-profiles to be increased to the extent that even non-monotonic q-profiles can be represented. At JT-60U, the MSE diagnostics consists of 10 channels with 10-15 cm spatial resolution and 10 ms temporal resolution [Fujita(1997)].

3.3.7 Profile reconstruction procedure at ASDEX Upgrade

This data analysis makes use of a database which has been collected over a wide time range (from discharge #12000 to #22000); therefore when dealing with the kinetic profiles most attention was at fitting the profiles making use of empirical knowledge of certain diagnostics peculiarities, calibration errors and by getting the most information from similar but better diagnosed discharges. To do this,

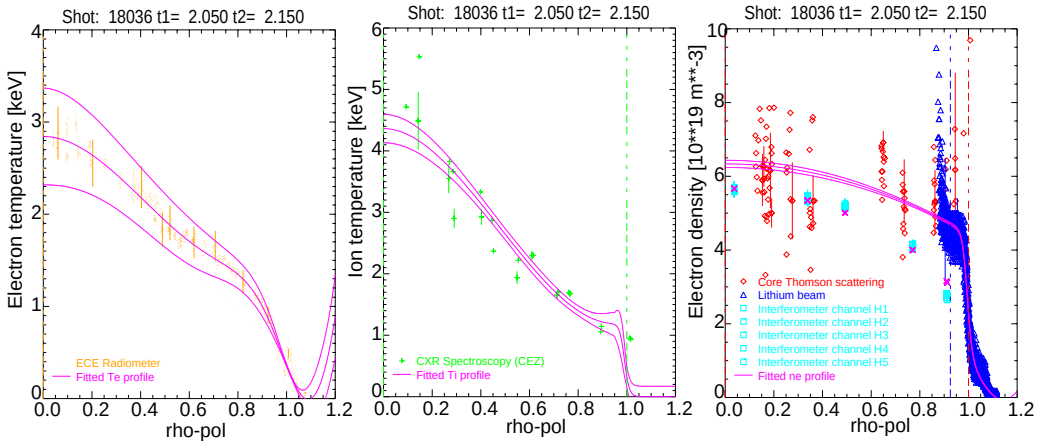

Figure 3.3: Kinetic profiles for ASDEX Upgrade: the electron temperature profile is fitted using ECE diagnostic (left), the ion temperature profile is fitted using CXRS data (center) and the density profile (left) is fitted by combining Thomson scattering data (up to $\rho_{\mathrm{pol}} = 1.0$) , Lithium beam data (starting from $\rho_{\mathrm{pol}} = 0.93$) and by matching the integrated values of the 5 interferometry channels data.

the "AUGPED" software (a tool created by L.D. Horton) has been used, which is an IDL based program initially written for the purpose of determining pedestal properties. It applies a modified hyperbolic tangent fit to the combined data of several edge and core density and temperature diagnostics and it gives the possibility to improve the resultant global profile. AUGPED reads the data of many ASDEX Upgrade diagnostics (T_e, T_i, n_e) along with their natural coordinate. It also uses a selectable magnetic equilibrium and maps data to the common coordinate, in general the normalized poloidal magnetic flux radius ρ_{pol}. It can do arbitrary radial shifts of each individual data set before applying the mapping. The profiles are always plotted with ρ_{pol}, but internally the program uses a real space coordinate on the outer midplane (unit: m) for the shifts. The time range for the profiles to be fitted has been $\Delta t = 100$ ms during a stable phase of the plasma. This relatively large time window is used to reduce the random errors on the single time measurements. The density profile has ben fitted by combining as many diagnostics as possible: in general, the Lithium Beam diagnostic information at the edge with the Thomson scattering in the core give a reliable density profile in terms of shape but not in terms of absolute value. This, instead, has been calibrated by shifting the data points of the Thomson diagnostics up or down so to match the integrated signal of the 5 channels of the inteferometer (DCN). The ion temperature profile has been fitted for the analyzed discharges with no edge measurements available. Therefore, the profile has been fitted by assuming for the edge a fixed pedestal width of 0.02 m which is an averaged value found at ASDEX Upgrade for the pedestal width of electron temperature profile using ECE in the core and Thomson scattering in the edge. As already mentioned, for

high density discharges and a given magnetic field ECE can be in cut-off. In ASDEX Upgrade discharges, cut-off is present on the LFS when $n_e > 6 \cdot 10^{19} m^{-3}$ and $B_T \leq 2.0$ T; in this case the electron temperature profile has been taken as closest estimate at a later time window in the same discharge with a phase of lower density or even from a similar discharge.

3.3.8 Profile reconstruction procedure at JT-60U

At JT-60U a third order polynomial function has been used to fit the kinetic profiles and the software SLICE has been used for this purpose. SLICE gives the possibility of adding or deleting data points to improve the fit. The choice of a third order polynomial is reasonable giving the fact that the number of data points from the Thomson diagnostic (which is the main diagnostic used for electron temperature and electron density) and the CXRS diagnostics for the ion temperature is not high and the fitted profile is smooth. The profiles have been fitted using one set of data for each time acquisition. In addition for the electron density measurements the absolute values have also been calibrated using the interferometer data (nelcu2).

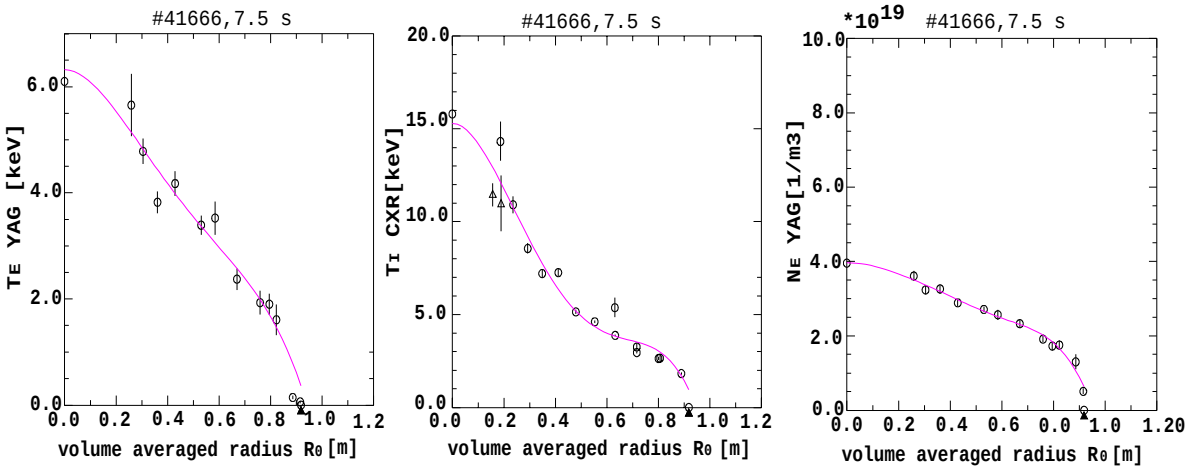

Figure 3.4: kinetic profiles for JT-60U plotted versus the volume averaged minor radius R_0: the electron temperature profile and the density profile (left) are fitted by using Thomson scattering diagnostic whereas the ion temperature profile is fitted using CXRS data (center).

3.3.9 Characteristic gradient lengths: L_{Te}, L_{Ti}, L_{ne}

The gradient lengths are defined using equations 2.27 and the spatial derivatives are calculated over the minor radius a. The value of the gradient lengths enter

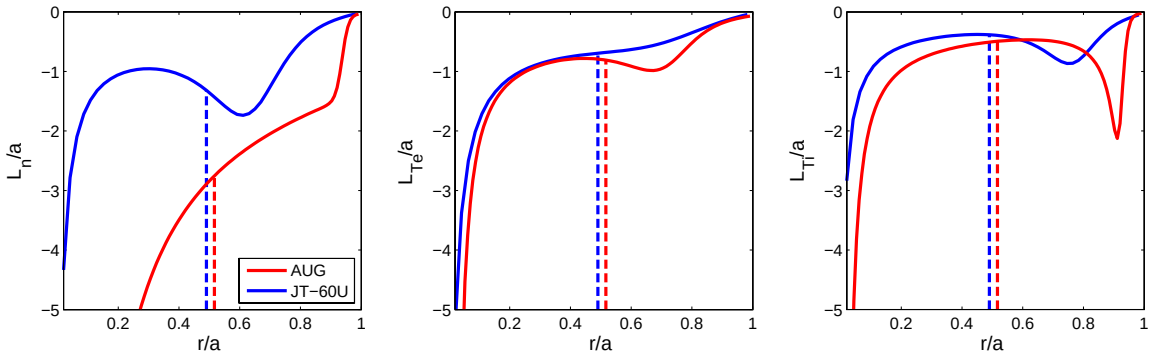

Figure 3.5: Gradient lengths of the the kinetic profiles for JT-60U and AUG. The local value of gradient length L_{ne} is the most delicate profile to determine since the density profile is in general not stiff as in the case of the electron and ion temperature profiles. The absolute value of L_{ne} interpolated at the resonant surface of the mode (dotted lines) is larger at ASDEX Upgrade than at JT-60U by almost a factor 2 and this is in agreement with the observation that for lower collisionality (JT-60U case) the density profile is expected to be more peaked.

in the Modified Rutherford equation via the curvature term Δ'_{GGJ} (introduced in section 2.39) through the dependency on p' of the resistive interchange parameter D_R. They also affect the calculation of the bootstrap current density profile j_{BS} and, therefore, their stiffness is very important. In general, the electron temperature T_e and the ion temperature T_i have stiff profiles in both ASDEX Upgrade and JT-60U as shown in figure 3.3 and figure 3.4. The electron density, instead, is flatter for ASDEX Upgrade than JT-60U and this is consistent with the fact that for lower collisionality $\nu^* \propto \frac{n_e}{T_e^2}$ (JT-60U case) higher density peaking is expected [Angioni(2003)]. As a consequence, the density gradient L_{ne} at JT-60U is expected to be characterised by higher values than in ASDEX Upgrade. In figure 3.5, the gradient lengths profiles of the kinetic measurements are shown normalised to the minor radius: the gradient lengths for electron and ion temperature have similar profiles whereas a difference between ASDEX Upgrade and JT-60U is evident in the local absolute value of the density gradient length L_{ne} which has almost a factor 2 difference and is larger for ASDEX Upgrade. In addition, one also should take into account that the method to calculate the derivatives of the profiles also affects the determination of the gradient lengths; at ASDEX Upgrade the hyperbolic tangent fit applied to the edge of the kinetic profiles determines steeper profiles in this region whereas in JT-60U, due the polynomial fit applied to the data, the fitted profile are characterised by more 'wiggles' throughout the minor radius.

3.4 Safety factor profile q and its gradient length L_q

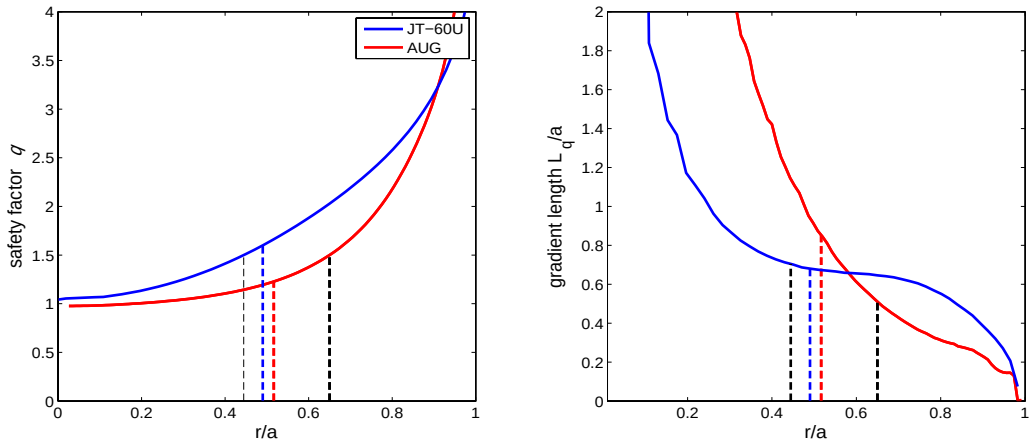

Figure 3.6: Safety factor profile and the gradient length L_q for JT-60U and ASDEX Upgrade discharge: the local value at the mode position (from the ECE measurement) is indicated in coloured dotted lines (blue for JT-60U and red for AUG) whereas the value of the mode position with respect to the $q = 1.5$ surface (from the equilibrium) is indicated in black dotted lines.

The safety factor profile q has been determined relying on the Motional-Stark-effect (MSE) diagnostic at JT-60U whereas for ASDEX Upgrade it has been evaluated using the equilibrium reconstruction from CLISTE. In general, the shape of the reconstructed q-profile at the edge it's robustly measured because of the constraint provided by magnetic data although important information from diamagnetic effects and fast particles contributions may be missing. In the core its information is more limited although the presence of some $q = 1$ surface activity such as sawteeth or fishbones for some discharges suggests that the central value of q can't be so far away from $q(0) = 1$. As in the case of the kinetic profiles, the shape of the q-profile affects mostly the accuracy in the determination of its gradient length L_q as shown in figure 3.6. At ASDEX Upgrade the q-profile is steeper towards the edge and its gradient length varies sharply. This steepness introduces a larger discrepancy between the mode position measured from ECE and the one given from the equilibrium both indicated in figure 3.6; in JT-60U, on the other hand, in the range $0.3 < r/a < 0.7$ the gradient length L_q changes only slightly and the mode position from ECE is in better agreement with the one provided by the equilibrium.

3.5 Determination of saturated island size W_{sat} and mode position

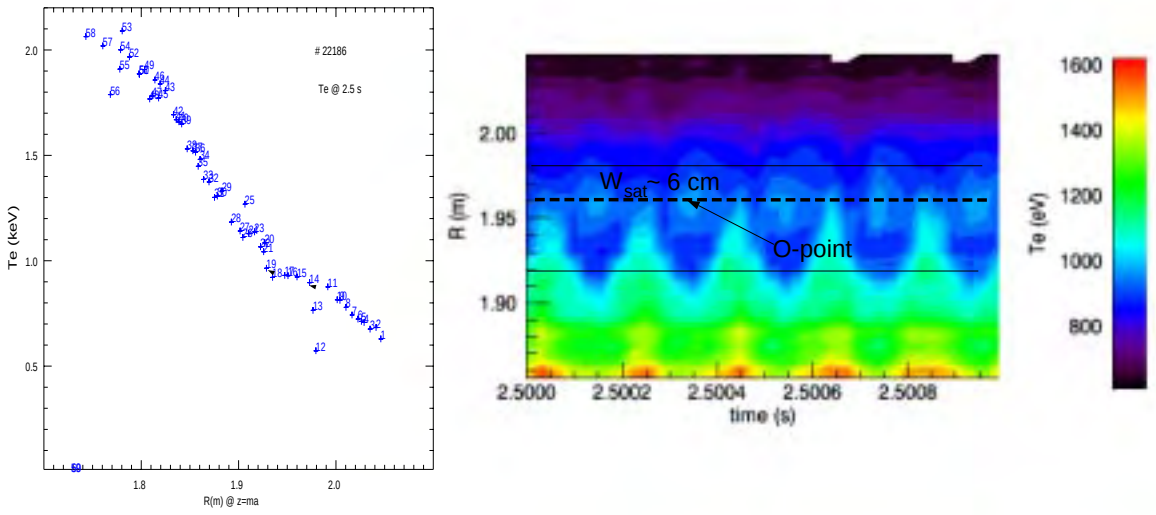

Figure 3.7: Electron temperature profile for #22186 together with the contour plot which nicely shows the (2,1) magnetic island chain ant the asymmetric shape of the magnetic island: the O-point of the island is at $R = 1.96$ m which corresponds to $r_{res} = 0.25$ m

The structure of magnetic islands is experimentally observed by the electron temperature profile measured by electron cyclotron emission diagnostic (ECE). In fact, due to the helicity of the magnetic eld lines the toroidally rotating plasma seems to rotate in the poloidal cross section and thus the temperature profile of the perturbed plasma ideally gives a sine signal outside the island and a periodic signal with flat phases inside the island corresponding to a sine signal with harmonics. Therefore, a clear flattening of temperature profile is visible and it is enough to determine the width and the position of the magnetic island width as one period in time corresponds to the helical angle range of one island. Figure 3.7 shows the global temperature profile for discharge #22186 (AUG) with the visible local flattening due to the presence of a (2,1) magnetic island. For well resolved measurements, the contour plot of the raw signal (R, T_e) is already enough for establishing how wide is the island width. Nevertheless, in case the island width is not well resolved an other method is used [Fitzpatrick(1995)] which is to recover the amplitude of the temperature perturbation $\tilde{T}_e$ determined by the island and characterized by two maxima indicating the X-point of the island and by the phase jump at the resonant position O-point of the island. This is achieved

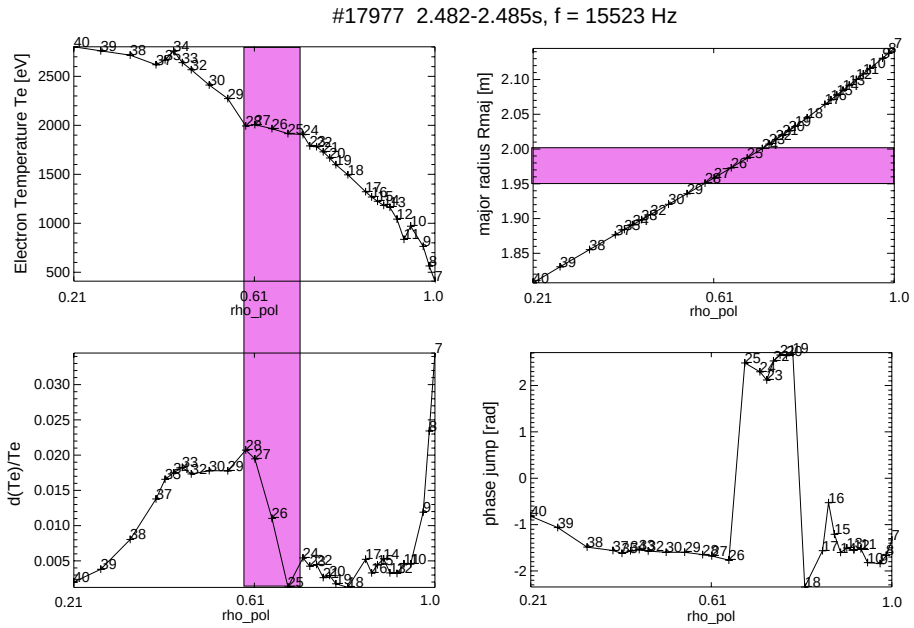

Figure 3.8: Fast Fourier Transform analysis for discharge #17977 at ASDEX Upgrade: the electron temperature profile (left) where the flattening due to a (3,2) NTM is visible. The amplitude perturbation $\tilde{T}_e$ obtained with the FFT analysis is plotted below it and it shows that together with the (3,2) island also a coupled (2,2) is present (channels 32-37) [Meskat(2001)]. On the right the projection on the minor radius of the ECE channels gives a saturated island width $W_{\mathrm{sat}} = 0.05$ m. Below the phase jump shows that the O-point of the island is located at channel 26.

by using a Fast-Fourier-Transform (FFT) filter at the frequency of the NTM. The information from the first dominant harmonic of the mode is enough for determining its width and position. In general, the location of the mode r_{res} is the position of the O-point of the island and is established directly from contour plot (as in figure 3.7) or by localising the position of the phase jump in the $\tilde{T}_e / T_e$ plot (as in figure 3.8). In the measurements, the O-point is not symmetrical within the island whereas in the Modified Rutherford equation the island width is assumed to be symmetrical. This, as it will be shown in chapter 5, has important consequences on the results of this analysis. At ASDEX Upgrade, the standard data acquisition system of the ECE diagnostic has a sample frequency of 32 kHz which is far too low for resolving the signal of a (3,2) NTM which has a frequency typically in the range 15-25 kHz. For ASDEX Upgrade, the FFT analysis mentioned above together with the contour plot and the local electron temperature profile behaviour have been used for determining the island width and position. For the (2,1) NTMs the island structure looks very clear from the contour plot, but for the (3,2) NTM this is not always the case since the frequency is higher and the ECE data during the experiments has been detected with a sample every 32 KHz and therefore not enough time resolution is available for this data.

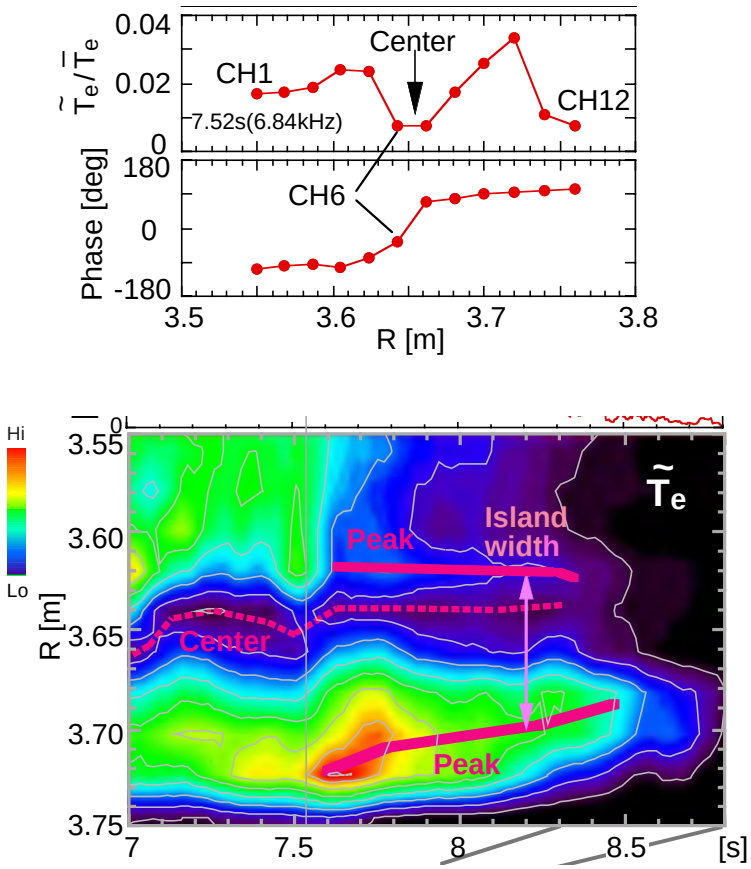

Figure 3.9: Island width measurement at JT-60U for #41666: on the left the FFT analysis for the saturation time $t = 7.5$s and on the right the evolution in time of the $\tilde{T}_e$ signal during stabilisation phase with ECCD which occurs at $t \sim 8.7$ s

A first estimate can be given by looking directly at the temperature profiles. For JT-60U discharges, the determination of the island width at saturation has also been done by using the FFT analysis as shown in figure 3.9. For some discharges, since the electron temperature profile from ECE is not available, the flattening of T_i has been used as indicative width of the magnetic island. Figure 3.9 shows on the top the amplitude perturbation $\tilde{T}_e / T_e$ obtained with the FFT analysis (in this case $\tilde{T}_e$ is divided by the averaged T_e profile to avoid calibration errors) and on the bottom the same signal evolving in time towards zero during the stabilisation experiment. Also in the case of JT-60U discharges, the measured magnetic islands have an asymmetrical shape.

3.6 The experimental time evolution of the magnetic island width $W(t)$

The time derivative of the magnetic field $\dot{B}(t)$ can be measured locally with a loop of magnetic coils positioned around the plasma, called Mirnov coils. The diagnostic measures the voltage $V = -\frac{d\Phi}{dt}$ where Φ is the linking flux. Since the equilibrium current changes very slowly compared to the mode rotation velocity, the Mirnov coils in general detect only perturbation currents and therefore they are useful to detect instabilities in the plasma such as NTMs. Indeed, during an experiment the presence of an NTM is noticed not only by the drop in β but also by looking at the spectrogram obtained with the Mirnov coil signal as shown in figure 3.10. By making measurements with coils located in different positions around the plasma it is also possible to identify the mode number (m,n). At ASDEX Upgrade, the (3,2) and (2,1) NTMs are easily recognizable by looking at the dominant frequencies in the spectrogram as the frequency of the (3,2) lies in the range 10-20 KHz and the (2,1) lies below 6-7 KHz. AT JT-60U, the NTM is also identified with the Mirnov coils and often the mode number is cross-checked using the toroidal velocity v_T measurement which, to a first approximation, is related to the mode frequency and the toroidal mode number n by the formula $f \sim \frac{v_T n}{2\pi R_{\mathrm{maj}}}$. The crucial feature of this diagnostic for the purpose of this work is that it provides an almost direct observation of the experimental island width evolution $W(t)$. In fact, according to the island model described in chapter 2, the island width W is proportional to the square root of the amplitude of the perturbed magnetic eld $W \propto \sqrt{B_\theta(r_{\mathrm{res}})}$ which in practice can be isolated by filtering the signal at the NTM mode frequency f. An important point, though, is that from the magnetic measurements detected outside the plasma alone neither the position of the mode nor the spatial mode structure can be resolved. Even more difficult is the investigation of coupled modes, resonant at different magnetic surfaces. Nevertheless a rough estimate of the island width can be obtained by considering that magnetic perturbations, in a cylinder, fall off with distance $B_\theta(r_{\mathrm{coil}}) = B_\theta(r_{\mathrm{res}})(\frac{r_{\mathrm{res}}}{r_{\mathrm{coil}}})^{m+1}$ [Zohm(1990)] where $B_\theta(r_{\mathrm{coil}})$ is the value of the perturbation field measured at the position of the detecting coil and $B_\theta(r_{\mathrm{res}})$ is the value of the perturbation where the mode is located. Therefore, the relation

$$W \sim C\sqrt{B_\theta(r_{\mathrm{res}})} \sim C\sqrt{B_\theta(r_{\mathrm{coil}})(\frac{r_{\mathrm{coil}}}{r_{\mathrm{res}}})^{m+1}} \tag{3.14}$$

is valid and can be used to approximately scale the measured island width $W(t)$ from one discharge where the island width measurement is available from ECE diagnostic (to get the calibration factor C) to other similar discharges for which the island width measurements by ECE are not available. In order to scale properly the island width value, though, an offset needs to be subtracted to the experimental W(t) resulting from the background noise of the Mirnov coil signal and

this is a main source of error in the final estimate of the island width W. Indeed, a comparison has been carried out for the ASDEX Upgrade database between the values of W_{sat} obtained by direct measurement with ECE for each discharge and by the values obtained using the Mirnov coil signal calibrated to the best ECE measurement available for one discharge and they do not differ for more than 40% (see section 4.3.2).

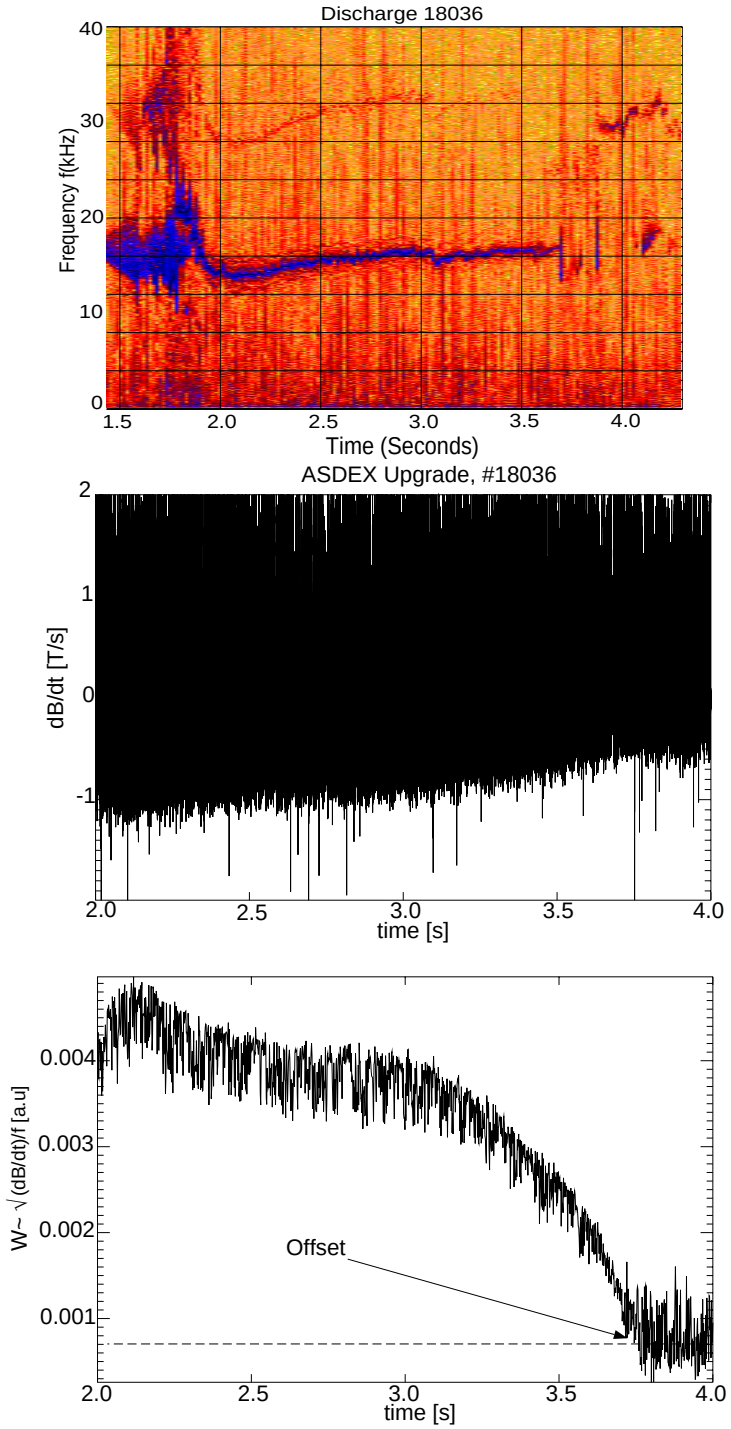

Figure 3.10: The NTM frequency of (3,2) NTM together and its harmonics for discharge #18036 in the frequency spectrum obtained with the Mirnov coil diagnostics. Below $\dot{B}_\theta$ signal and $W(t) \propto \sqrt{\dot{B}_\theta / f}$ for discharge #18036 at ASDEX Upgrade obtained by filtering the signal at the mode frequency $f \sim 15KHz$. An offset (dotted line) is subtracted due to the noise of the Mirnov diagnostic

3.7 j_{BS}, j_{ECCD} and ECCD deposition width d

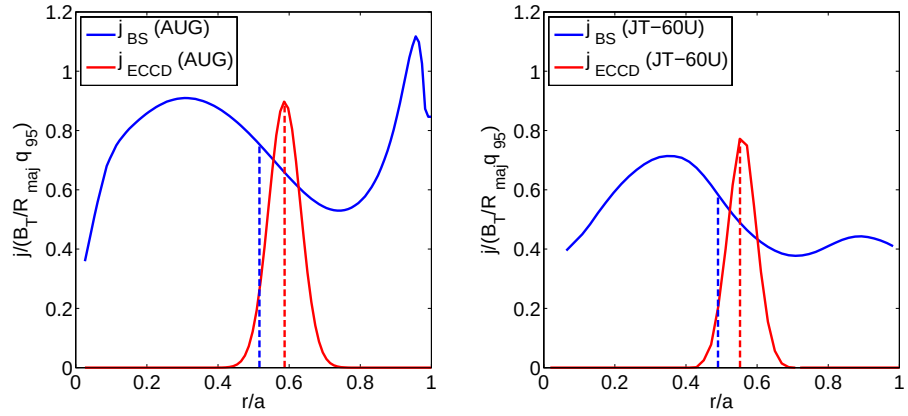

Figure 3.11: Bootstrap current density profile j_{BS} for ASDEX Upgrade and JT-60U discharges together with the gaussian profile of the injected j_{ECCD} current density of width d for discharge #18036 (left) with $\beta_N \sim 2.2$ and discharge #41666 (right) with $\beta_N \sim 1.5$ both normalised to $\frac{B_T}{R_{maj} q_{95}}$. The j_{BS} is steeper at the edge for AUG because of steeper pressure gradient. The local j_{BS} is higher for ASDEX Upgrade than for JT-60U as the bootstrap current density mainly depends by the value of the β, which is larger for AUG discharge. The j_{ECCD} current is characterised by a Gaussian profile and the mismatch between the mode location (blue dotted line) and the injection location (red dotted line) indicates the presence of a possible misalignment between the center of the island and the ECCD beam.

In this study in order to determine the bootstrap current density j_{BS}, two transport codes have been used, ASTRA [Pereverzev(1991)] which is the main tool for transport studies in ASDEX Upgrade and ACCOME [Tani(1992)], which is the main tool for transport studies at JT-60U. They are codes for predictive and interpretative transport modelling and for processing experimental data. ASTRA incorporates a system of two-dimensional equilibrium equation, one-dimensional diffusion equations for densities and temperature of different plasma components and a variety of other modules describing additional heating, current drive and other non-diffusive processes in tokamak plasmas. The transport coefficients can be specified in the code or also given externally. In our case, the calculation of the bootstrap current density j_{BS} has been done in both machines using the Hirshman and Sigmar model [Hirshman and Sigmar(1977)] for a multi-species plasma with carbon as only impurity. Z_{eff} is assumed constant and equal to 2.5 in JT-60U and it is determined by comparing the neutron emission rate with the experimental one. In ASDEX Upgrade, Z_{eff} is set equal to 2 and it is a value taken from Bremsstrahlung measurements (discharge #17797)[Meister(2004)]. Figure 3.11 shows that in ASDEX Upgrade the bootstrap is more peaked at the edge

than at JT-60U and this is an effect due to the density gradient in the edge region of the plasma which is steeper at ASDEX Upgrade than at JT-60U. Usually, in order to determine the ECCD current density j_{ECCD} and its deposition width d the beam-tracing technique for drawing the propagation of the EC beam with a Gaussian cross-section in cold plasma is adopted. In this work, for ASDEX Upgrade discharges the EC deposition parameters have been calculated by the TORBEAM code [Poli(2001)] and in JT-60U by the ECH code [Suzuki(2002)]. In the linear theory the fraction of the absorbed EC power in the plasma is

$$\frac{P_{\mathrm{abs}}}{P_0} = 1 - e^{-\int \alpha ds} \tag{3.15}$$

where $\alpha = 2k$" is the absorption coefficient and the integral is over the beam path s. The absorption of the EC beam propagating in the plasma begins when a part of its phase front satisfies the wave-particle resonance condition:

$$\omega - \frac{n\omega_{ce}}{\gamma} = v_{\parallel} k_{\parallel} \tag{3.16}$$

The absorption profile is then determined according to equation 3.15 from the local values of the absorption coefficient α and the geometry of the beam in the resonant region. Therefore, EC deposition parameters such as j_{ECCD} and d are sensitive to many factors: magnetic field B and equilibrium, plasma density n_e and electron temperature T_e , which are flux functions, and a variety of geometrical factors such as launching angles, launcher position and initial shape of the beam. In general, the ECCD current density had the following dependency:

$$j_{\mathrm{ECCD}} \sim \frac{P_{\mathrm{ECRH}} T_e}{n_e} \frac{1}{r_{\mathrm{res}} d} \tag{3.17}$$

where P_{ECRH} is the injected ECRH power and d the deposition width. The deposition width d depends mainly on the electron temperature $d \propto \sqrt{T_e}$ because of relativistic effects due to the Doppler shift and on the geometric width of the injected beam, which is mainly depending on the experimental set-up of the ECRH system. In figure 3.11 the typical gaussian deposition profile for the ECCD current density j_{ECCD} is indicated for both ASDEX Upgrade and JT-60U. The centre of the deposited current calculated with the two codes results to be slightly shifted compared to the mode location, indicating a possible misalignment between the island and the injected ECCD beam.

3.8 Neoclassical Resistivity η_{NC}

The neoclassical resistivity is in general a function of Z_{eff}, trapped particle fraction $\sqrt{\epsilon}$ and it depends mainly on $T_e^{-3/2}$ [Wesson(1997)]:

$$\eta_{\mathrm{NC}} \sim \frac{Z_{\mathrm{eff}}}{T_e^{3/2}} (1 - \epsilon^{1/2})^2 \tag{3.18}$$

Both at ASDEX Upgrade and JT-60U it has been calculated numerically (with ASTRA and Topics code [Hayashi(2004)] respectively) using as neoclassical transport coefficients those provided by [Hirshman and Sigmar(1977)]. In general, the resistivity in ASDEX Upgrade is smaller than in JT-60U as the electron temperature is 1-2 times higher at JT-60U for a similar position $r/a \sim 0.5$ of the mode in the plasma. In figure 3.12 the neoclassical resistivity profiles normalised to the local electron temperature T_e and the Z_{eff} are shown. As a consequence, the resistive time $\tau_s \sim r_{\mathrm{res}}^2/\eta_{\mathrm{NC}}$ is larger at JT-60U than at ASDEX Upgrade due to the increased size of the machine.

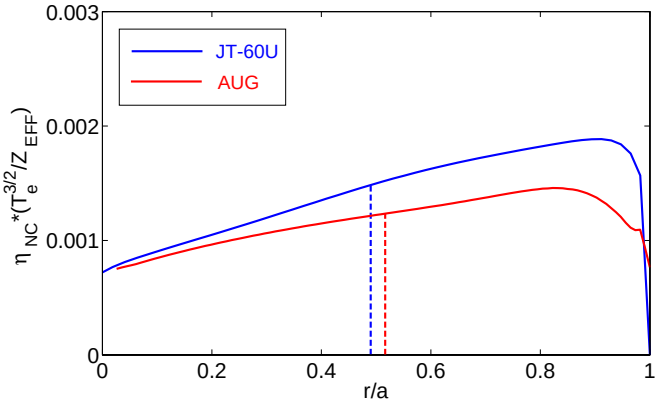

Figure 3.12: Neoclassical resistivity profile for ASDEX Upgrade and JT-60U normalised to $\frac{T_e^{3/2}}{Z_{\mathrm{eff}}}$: the normalised resistivity is in both JT-60U and ASDEX Upgrade almost constant and the small difference between the two profiles is due to the realistic geometry adopted in the codes to calculate η_{NC}

Chapter 4

NTM stabilisation experiments with Electron Cyclotron Current Drive

As described in chapter 2, the dominant mechanism which allows for the growth of the NTMs in the plasma is the missing of the bootstrap current within the magnetic island. A well established technique to control NTMs is by replacing the missing bootstrap current density j_{BS} with an externally injected one. This is provided by exploiting the interaction between electromagnetic waves and the plasma, which can become resonant and transfer energy to each other. In particular, by using Electron Cyclotron Resonance Heating (ECRH) the energy of electromagnetic waves is transferred to the electrons of the plasma when its frequency is equal to a harmonic of the electron cyclotron frequency $\omega_c = \frac{eB}{m}$. If the injection of the electromagnetic wave is oblique with respect to the resonant layer a current density j_{ECCD} is generated in the region where the resonance takes place. This scheme is referred to as Electron Cyclotron Current Drive (ECCD). The occurrence of an NTM is called NTM destabilisation. If the NTM amplitude can be decreased by using ECCD till its disappearance , the mode is completely stabilised. In this chapter, the ECRH systems and the experiments for stabilising (3,2) and (2,1) NTMs with ECCD at ASDEX Upgrade and at JT-60U used for this analysis are presented.

4.1 Electron Cyclotron Resonance Heating system at ASDEX Upgrade

In ASDEX Upgrade the ECRH system which has been used for the analysed NTM stabilisation experiments consists of 4 gyrotrons (sources for generating electromagnetic waves) working at 140 GHz. At the usual value of the toroidal magnetic field $|B_T| \approx 2.5$ T, this corresponds to the second harmonic X-mode of the

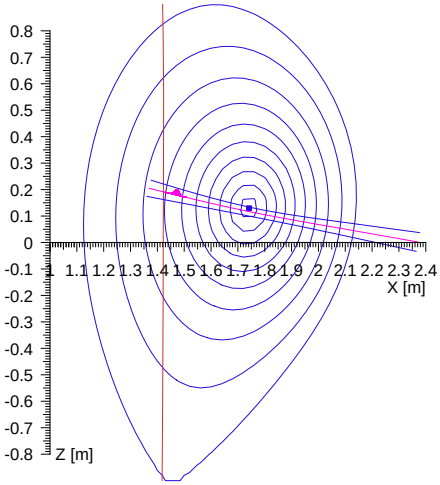

Figure 4.1: Poloidal cross-section of ASDEX Upgrade with ECCD beam injection for discharge #18036

EC wave which is launched into the plasma from the low field side (LFS) of the equatorial mid-plane as shown in figure 4.1. In the usual ASDEX Upgrade divertor configuration, the magnetic axis is accessible when the beams are launched at a poloidal angle $\theta \approx 10°$. A further change of θ in the range $\pm 32°$ displaces the EC absorption vertically along the resonance layer, which can also be shifted radially by changing the toroidal magnetic field B_T. By changing the toroidal launching angle ϕ in the range $\pm 30°$ the EC beam can be launched obliquely to produce current drive (co-or ctr-ECCD). All gyrotrons are able to deliver $P_{\mathrm{ECRH}} = 0.5$ MW for 2 s, of which 0.4 MW are absorbed by the plasma. At the end of each transmission line a steerable mirror allows the launching of the focused beam in the desired poloidal and toroidal directions. However, the steerable mirror is fixed at the beginning of each experiment and can only be actively changed between discharges; therefore to optimise the oblique injection in the plasma a linear scan of about 20% of the B_T field characterises the experiments.

4.2 Electron Cyclotron Resonance Heating system at JT-60U

In JT-60U the ECRH system consists of four gyrotrons which heat at the fundamental O-mode or in the 2^{nd} harmonic X-mode with a frequency of 110 GHz and inject from the low field side (LFS) of the plasma. The resonance condition is reached at $B_T \approx 1.7$ T in the O-mode case and at $B_T \approx 3.7$ T in the X-mode case.

The total injection power P_{ECRH} reaches 3 MW. In JT-60U the toroidal injection angle ϕ is kept fixed whereas the poloidal injection angle θ can be slightly varied for profile control by changing the position of the mirror by 2-3 degrees. Fig.4.2 illustrates a typical poloidal cross-section of JT-60U and the position of the injected ECCD beams on the resonant surface.

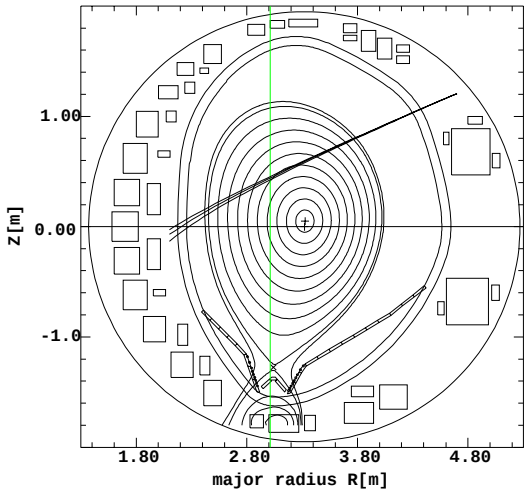

Figure 4.2: Poloidal cross-section of JT-60U with beam injection for discharge 41666

4.3 NTM stabilisation experiments with ECCD

In a typical NTM stabilisation experiment, an NTM is destabilised and a saturated mode (of width W_{sat} and $dw/dt \approx 0$) is allowed to form. Subsequently, the ECCD power P_{ECRH} is applied which generates a highly localised current in the region where the resonant surface is located. If the necessary criteria for stabilisation such as having enough P_{ECRH} and having a not too large radial misalignment $x_{\mathrm{mis}} = r_{\mathrm{dep}} - r_{\mathrm{res}}$ between the ECCD beam deposition radius and the radius at the resonant surface of the island are fulfilled then the NTM is stabilised and the plasma confinement can be recovered. As already mentioned, two different approaches are used to hit the resonant surface in the two devices. At ASDEX Upgrade, a scan of the toroidal magnetic field B_T of about 0.2 T is made to hit the resonant surface, starting on one side of the island. This corresponds to a radial shift ΔR of about 10 cm in 2 s [Maraschek(2004)]. At JT-60U, instead, the hitting position of the ECCD beam is optimised from discharge to discharge. With the help of the electron temperature radial profile, the amplitude and the phase at the mode frequency allow for the identification of the resonant surface location so that the mirror of the ECCD system is consequently tilted for better alignment [Isayama(2003)]. It typically takes several 100 ms to stabilise an NTM during the

B_T scan whereas in discharges with a constant optimised magnetic field the stabilisation typically takes less than 100 ms. The selection of the discharges used in

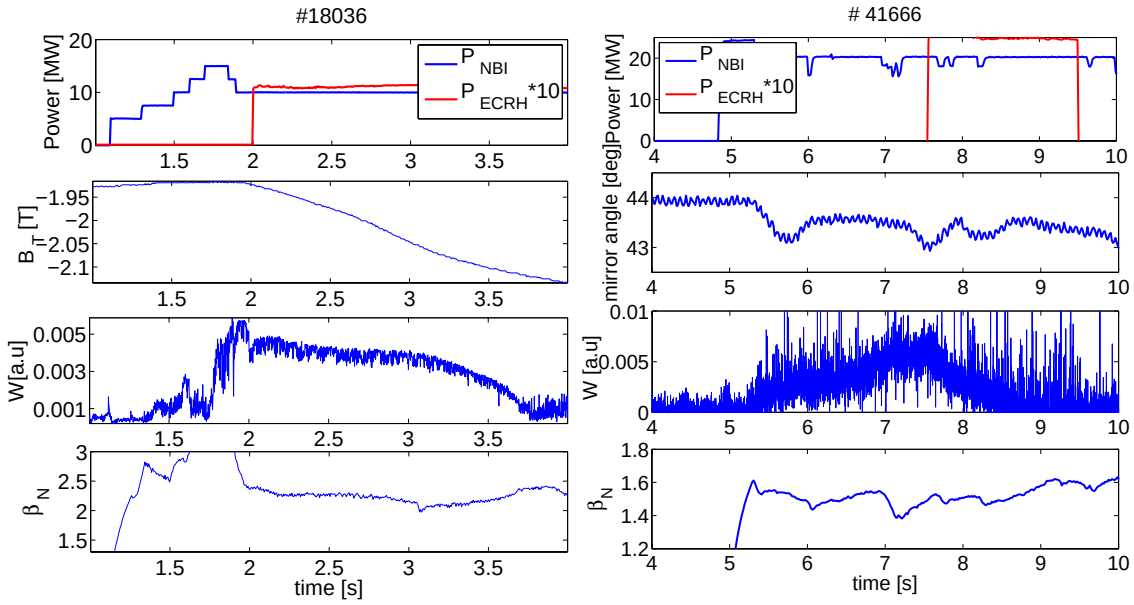

Figure 4.3: Typical time slices for NTM stabilisation experiments for #18036 with $\beta_N \sim 2.2$ (AUG) and for #41666 with $\beta_N \sim 1.5$ (JT-60U): the NBI power P_{NBI} is increased till the NTM is destabilised. Then, once the mode is triggered the P_{NBI} is stepped down to a level for which the available P_{ECRH} power is enough to effectively suppress the mode. As a consequence β_N increases. In ASDEX Upgrade (left), the resonance surface is hit by scanning the toroidal field B_T whereas in JT-60U (right) the mirror angle is slightly varied (1-2 degrees) during the discharge so to optimise the ECCD position of injection.

this work is done based on various criteria: first of all, the necessary data for the analysis has to be available in particular the electron temperature measurement, the electron density measurement and a good equilibrium profile in order to be able to produce a reasonable β profile. Secondly, the Mirnov coil signal $W \sim \sqrt{B_\theta}$ has to clearly show a decay during the stabilisation without major unclear behaviours in order to compare it to the simulation obtained with the Modified Rutherford equation. Some information on misalignment x_{mis} is required either from the magnetic field scan or from the increase of local temperature profile due to ECCD. In addition, it was useful to work with similar discharges done preferably in sequence to get trends and consistent measurements. In order to understand how much do the discharges which are analysed and compared at JT-60U and ASDEX Upgrade differ among themselves in terms of geometry and shape, table 4.1 resumes the global plasma parameters which have been set during the experiment together with the geometrical factor s (introduced in chapter 3) for the five different sets of NTM stabilisation discharges. The difference in the

value of s between the two machines is about 20% whereas within ASDEX Upgrade and JT-60U database the difference in the geometrical set-up among (3,2) and (2,1) NTMs discharges is below 10% .

NTM	I_p [MA]	B_T [T]	$\frac{a^2}{R_{maj}}$	q_{95}	s
(2,1) NTM AUG	0.8	1.85	0.14	4.4	14.2
(2,1) NTM - a JT-60U	1.5	3.7	0.19	3.9	8.3
(2,1) NTM - b JT-60U	0.85	1.7	0.19	3.5	10.0
(3,2) NTM AUG	0.8	2.1	0.14	4.8	12.5
(3,2) NTM JT-60U	1.5	3.7	0.19	3.75	8.0

Table 4.1: Global parameters set for the NTM discharges and resulting shaping factor s

4.3.1 NTM stabilisation experiments at ASDEX Upgrade

The NTM stabilisation experiments of ASDEX Upgrade used in this work are done in standard H-mode scenario, with $I_p = 0.8$ MA and $B_T \approx 2.0$ T for the (3,2) NTM or $B_T \approx 1.85$ T for the (2,1) NTM and conventional monotonic q-profiles [Maraschek(2004)]. The more detailed difference of ASDEX Upgrade discharges in terms of plasma shape and q_{95} is reported in figure 4.4 where the value of the profile averaged β_p versus β_N interpolated at the time t_{sat} when the NTM saturates shows a clear linear trend confirming the similarity in the plasma shape. The short high power phase during which the NTM is triggered is done with $P_{NBI} \approx 10 - 20$ MW. For the (2,1) NTM this reduction of P_{NBI} is necessary due to finite available ECCD power. For the (3,2) NTM the available P_{ECRH} is sufficient to always stabilise the mode but the β_N needs not to be greater than 2.3 as this would bring the mode in its FIR regime [Günter(1998)] for which a description with the Modified Rutherford equation would not be fully consistent due to mode coupling and different physics mechanisms to be accounted for. The value of marginal β_N for the (3,2) case is

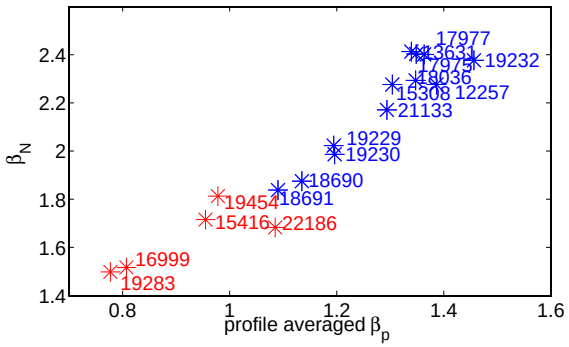

Figure 4.4: Value of the profile averaged β_p versus β_N interpolated at the time t_{sat} when the NTM saturates (and measurements are taken) for ASDEX Upgrade discharges: the (2,1) NTMs is characterised by lower β consistently with the fact that they are located more towards the outside of the plasma. The clear linear trend verifies that these discharges have similar plasma shape and q_{95}.

$\beta_{\mathrm{Nmarg}} < 1.8$ (#17057) whereas for the (2,1) case it is $\beta_{\mathrm{Nmarg}} < 1.2$ (#15416). For the (3,2) NTM the typical q_{95} is around 4.8 whereas the (2,1) NTMs a lower $q_{95} \approx 4.4$ has been used in order to be able to hit the resonant surface of the mode with the available ECCD set-up in terms of magnetic field and positioning of the ECCD beam. When the (2,1) NTMs are triggered they are usually locked for a certain time, that it they couple to the wall and stop rotating. However by the reduced NBI power, since the local β_p is reduced and $W_{\mathrm{sat}} \sim \beta_P$ holds, the mode gets smaller and starts to rotate again.

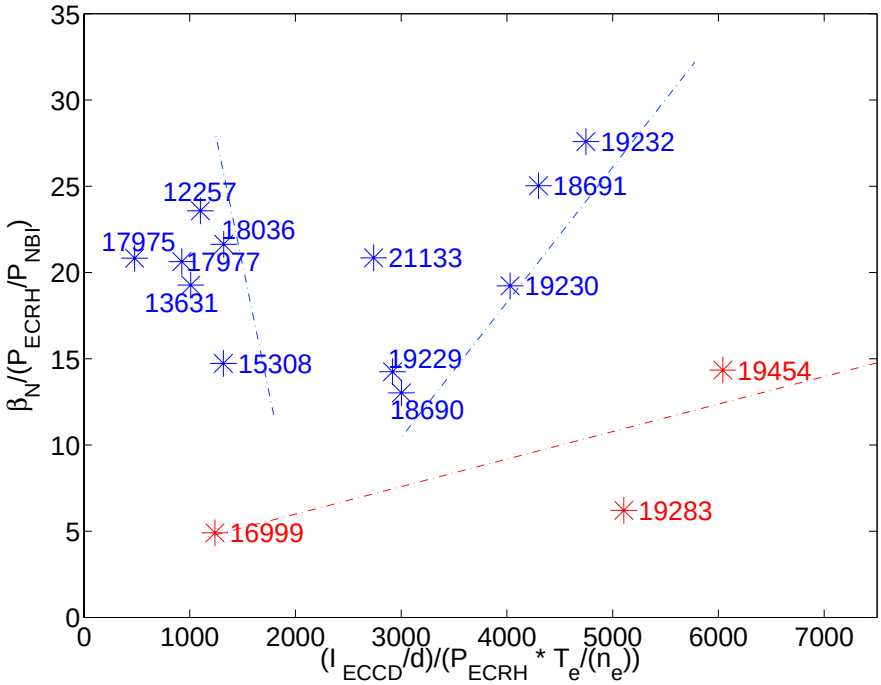

Figure 4.5: The maximal $\beta_N / (P_{\mathrm{ECRH}} / P_{\mathrm{NBI}})$ as a function of $(I_{\mathrm{ECCD}} / d) / (P_{\mathrm{ECRH}} \frac{T_e}{n_e})$ for AUG discharges; the dashed lines guide the eye to the three groups of discharges: on the left the (3,2) large deposition profile (blue), in the middle the (3,2) NTM small deposition profile (blue) which have the highest increase of β_N after stabilisation, on the right the (2,1) NTM discharges with small deposition profile which do not show an increase of β_N due to lower T_e and therefore lower efficiency of ECCD.

With this scenario, the (3,2) NTM could be stabilised at a maximal $\beta_N \approx 2.4$ with $P_{\mathrm{NBI}} = 12.5$ MW (#19232). For the (2,1) NTM a maximal $\beta_N \approx 1.9$ with $P_{\mathrm{NBI}} \approx 6.25$ MW and $P_{\mathrm{ECRH}} = 1.8$ MW could be achieved (#19454). The higher required ECRH

Table 4.2: Descriptive parameters for the (3,2) NTMs (in blue) and the (2,1) NTMs (in red) discharges of ASDEX Upgrade

#	P_{NBI} [MW]	P_{ECRH} [MW]	θ [deg]	ϕ [deg]	$j_{\mathrm{ECCD}}[MA/m^2]$	d [m]
12257	10	0.9	10	15	0.087	0.061
13631	10	1.2	10	15	0.167	0.071
15308	10	1.5	10	12	0.192	0.048
17975	10	1.1	10	20	0.070	0.17
17977	10	1.1	10	15	0.135	0.08
18036	10	1.1	10	12	0.236	0.051
18690	10	1.5	10	8	0.442	0.0184
18691	10	0.75	10	5	0.456	0.01
19229	10	1.3	10	7	0.432	0.021
19230	10	1.1	10	3	0.600	0.007
19232	12	1.1	10	5	0.700	0.01
21133	10	1.1	10	5	0.389	0.016
16999	6.25	1.8	10	12	0.150	0.042
19283	6.25	1.3	10	5	0.315	0.0074
19454	10	1.3	10	5	0.327	0.0066

power for the (2,1) NTM, together with the lower achievable β_N can be explained by the reduced ECCD current drive efficiency at lower temperatures T_e and the reduced β_{Nmarg} compared to the (3,2) NTM [Maraschek(2003)]. The NTM stabilisation experiments at ASDEX Upgrade are done with a deposition width of the ECCD beam d which can vary depending on the toroidal launching angle ϕ as mentioned before. Two different regimes have been used in the modelling of the Rutherford Equation: the case of a large deposition profile, where the deposition width $d > W_{\mathrm{sat}}$ and the case of a small deposition profile where $d < W_{\mathrm{sat}}$. In both cases, the W_{marg} was estimated to be of the order of W_{d} that is $\approx 2 - 2.5$ cm in agreement with the value established once the Mirnov coil signal is calibrated from W_{sat}. In table 4.2, the important parameters for analysing the efficiency of the ECCD stabilisation are shown for (3,2) NTMs and the (2,1) NTMs (indicated in red in the table): for large toroidal launching angles ϕ, the current density j_{ECCD} decreases and the deposition width is large > 4 cm, therefore part of the I_{ECCD} is injected also outside the island. The highest value of current density, instead, is reached at $\phi \approx 5°$. In the case of small toroidal launching angle, the calculated deposition width given from TORBEAM results in a very small value

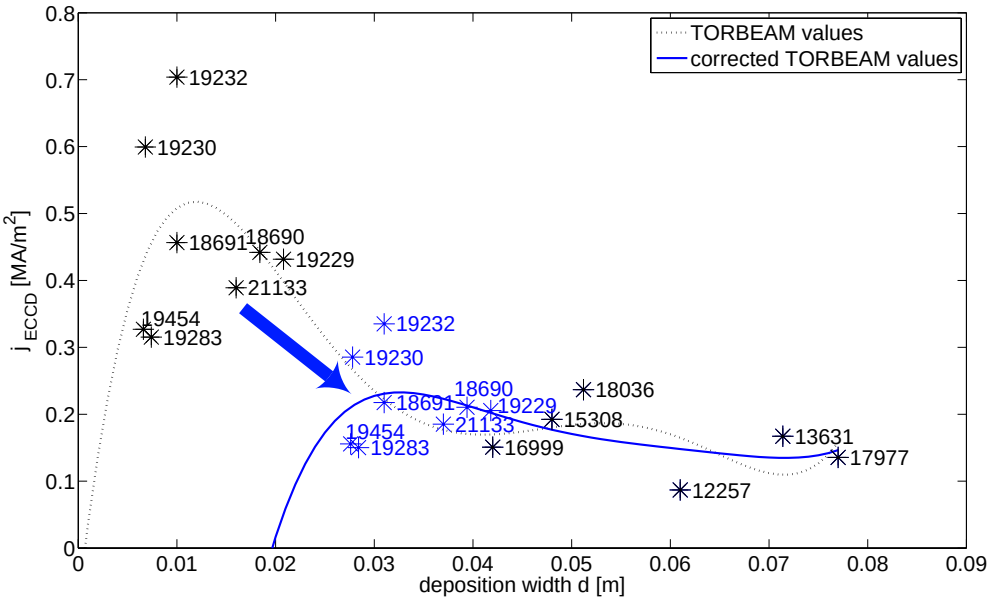

Figure 4.6: TORBEAM calculations for the j_{ECCD} and d values for ASDEX Upgrade discharges: the black points indicate the original output of TORBEAM for each discharge and the black line is the fitted polynomial function underlying these. The blue points are the corrected values for the discharges with small deposition profile which are assumed to have a minimum realistic deposition width larger than $d = 0.02$ cm. The blue line is the polynomial fit obtained by assuming a deposition width d of about 2 cm for the discharge #19230 with the smallest d. The arrow indicates the shift towards more realistic values of j_{ECCD} and d for the small deposition profile discharges.

$\leq 1-2$ cm. Almost a factor 2 difference in the value of deposition width d is obtained for #21133 and #19454 due to the more external mode position of the (2,1) NTM. A detailed transport analysis [Kirov(2002)] with ASTRA on the local effects of ECCD deposition on temperature profiles showed that the deposition width can't be smaller than about 2 cm. Therefore, taking this value as a lower limit for d, in the simulations of the NTM stabilisation with the Modified Rutherford equation 2.49 the values for j_{ECCD} and d have been modified in order to take this into account. In particular, the deposition widths smaller than 2 cm have been re-scaled (and consequently also j_{ECCD} since equation 3.17 is valid) so that 2 cm be the minimum possible value for the deposition width. This re-scaling is consistent with the values provided by TORBEAM for larger deposition profiles and is shown in figure 4.6: the strong peak in case of $d < 0.02$ cm that relates j_{ECCD} and d becomes smaller as d is corrected to realistic values. Nevertheless, for the large deposition cases the dependance of j_{ECCD} versus d provided by TORBEAM remains unchanged.

4.3.2 Comparison between W_{sat} from ECE and W_{sat} from Mirnov coils

In chapter 3, the method used to measure the saturated island width W_{sat} has been described which relied on ECE measurement of the electron temperature flattening when the NTM and therefore the magnetic island becomes very large and saturates. In addition, it has been mentioned that the measurement of the magnetic field perturbation ($\dot{B}_\theta$ detected using the Mirnov coil diagnostic) is a direct experimental observation of the island width evolution $W(t)$. Therefore, an other way of estimating the island width at saturation for discharges which do not have ECE data available, is to calibrate their Mirnov coil signal B_θ with the Mirnov coil signal of some discharge for which instead the value of W_{sat} is clearly measured by using the cylindrical approximation This exercise has been done for

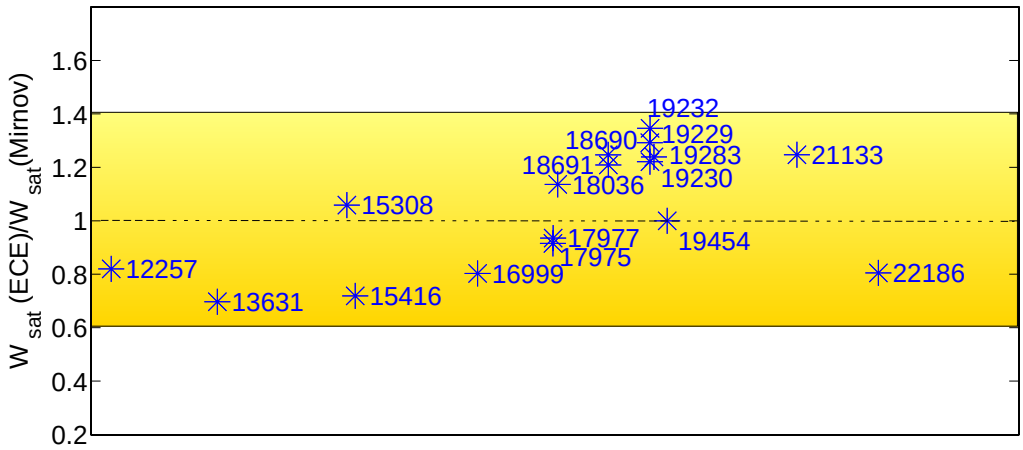

Figure 4.7: Comparison between the values for W_{sat} determined via ECE and those determined with calibration from Mirnov coils; discharge #19454 is used for calibration with ECE: for the oldest discharges the ECE measurement underestimates by $\sim 30\%$ the value obtained by calibrating to the Mirnov coil whereas for the newest ones the ECE measurement overestimates the value from the Mirnov coil calibration by the same amount. Although no clear trend could be found by using this approximative method to establish the island width size, it confirmed that the range in which W_{sat} lies with ECE measurement is consistent when using the Mirnov coil calibration.

the ASDEX Upgrade discharges in order to double check the consistency of the measurements with ECE, which in the case of (3,2) NTMs with $f \sim 16$ Khz are just at the Niquist frequency and are less accurate than other cases. For direct comparison the measurements from a poloidal coil ($C09-01$) situated on the LFS at $(R,z) = (2.5, 0.14)$ m have been used and the good island width measurement for discharge #19454 has been taken to calibrate the signal and proper offset has been subtracted. The error on the evaluation of the saturated island width is larger with this technique as more sources of error appear: the formula 3.14 comes from a cylindrical calculation; in addition, when calibrating to the Mirnov coil signal

the estimate of the offset directly affects the evaluation of the absolute value of the island width W_{sat}. Nevertheless, the estimate of the island width W_{sat} is consistent within $30\% - 40\%$ between the two methods. Figure 4.7 shows the ratio between the island width W_{sat} measured with ECE and the one calibrated from Mirnov coil signal: for the oldest discharges the ECE measurement underestimates by $\sim 30\%$ the value obtained by calibrating to the Mirnov coil whereas for the newest ones the ECE measurement overestimates the value from the Mirnov coil calibration by the same amount. This may be due to slight changes in time of the diagnostic systems (ECE or Mirnov).

4.3.3 NTM stabilisation experiments at JT-60U

Table 4.3: Descriptive parameters for the (3,2) NTMs (in blue) and the (2,1) NTMs (in red) discharges of JT-60U

#	P_{NBI} [MW]	P_{ECRH} [MW]	ϕ [deg]	θ [deg]	$j_{\mathrm{ECCD}}\,[MA/m^2]$	$d\,[m]$
41647	11.2	2.6	23.6	21.9	0.27	0.1
41650	16	1.2	23.4	20.9	0.15	0.09
41652	16	2.5	23.4	20.9	0.28	0.09
41666	20	2.6	23.6	21.9	0.23	0.01
41671	23	2.0	23.6	21.9	0.15	0.11
41695	22	2.6	23.6	21.9	0.25	0.12
46367	11.5	0.6	22.8	16.9	0.029	0.09
46368	11.5	0.9	22.8	16.9	0.041	0.09
47788	6.0	1.45	22.1	13.0	0.046	0.07
47793	6.0	0.9	22.1	13.2	0.03	0.07
47796	6.0	0.55	22.1	13.2	0.014	0.07

The NTM stabilisation experiments from JT-60U under investigation in this work are selected from recent JT-60U experimental campaigns and are standard H-mode scenario with conventional monotonic q-profile. The (3,2) NTM discharges are done with $I_p = 1.5$ MA and $B_T = 3.7$ T at $q_{95} = 3.5$ and their marginal β_{Nmarg} is is about 0.9. For these discharges, up to 2.7 MW of P_{ECRH} is injected to stabilise the mode [Isayama(2003)] using the ECRH system in fundamental O-mode. The W_{marg} is small compared to the deposition width d and the marginal island obtained from $W_d \sim 1.5 - 2$ cm from the formula and the island decay prediction are consistent. Of the five (2,1)-NTM discharges, #46367 – #46368 are done with $I_p = 1.5$ MA, $B_T = 3.7$ T with $q_{95} \approx 4.0$. The NBI power is increased up to 25 MW to trigger the mode at $\beta_N = 2.0$ and then lowered till $\beta_N \sim 1$. The marginal β_{Nmarg} for these discharges is 0.4 and the ECCD resonance is reached using the

fundamental O-mode. The other three (2,1) NTM discharges #47788, #47793 and #47796, instead, are done with $I_p = 0.85$ MA, $B_T = 1.7$ T with $q_{95} = 3.5$ with $\beta_{\mathrm{Nmarg}} = 0.9$ and using the 2$^{\mathrm{nd}}$ harmonic of the X-mode resonance. These discharges were set and run remotely from Garching [Ozeki(2008)] and were done to study the marginal ECCD power requirement for NTM stabilisation. So from one discharge to the other, after having optimised the injection angle to $\theta = 13.2°$, the P_{ECRH} was reduced till the mode was marginally stable. This was achieved in #47796 where only $P_{\mathrm{ECRH}} = 0.5$ MW has been injected. A characteristic of the (2,1) NTM stabilisation discharges at JT-60U which we analysed is the co-presence of a (3,2) NTM mode with the (2,1) NTM as the spectrogram in figure 4.8 shows and as verified by calculation the rotation frequency of the mode using CXRS toroidal velocity. In particular, the two modes do not seem to be coupled as the (2,1) NTM has a frequency $f \sim 5$ kHz and the (3,2) NTM has a frequency $f \sim 13$ kHz. The

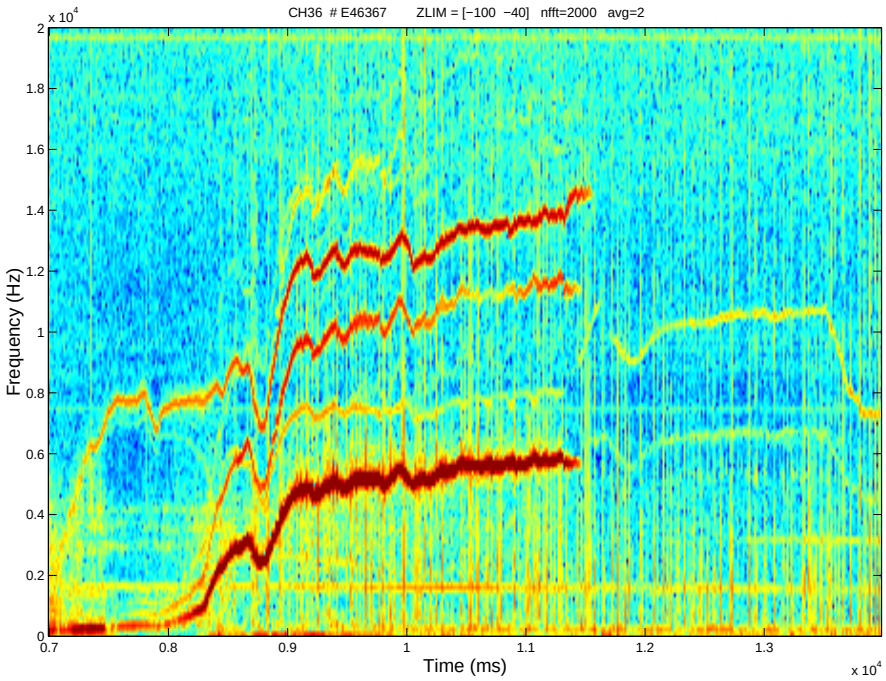

Figure 4.8: spectrogram of #46367: Co-existance of a (3,2) NTM and a (2,1) NTM: the two modes are coupled creating a beat wave with $\omega = (\omega_{32} + \omega_{21})/2 \sim 8.5$ kHz

optimised angles for ECCD stabilisation at JT-60U discharges are such that the ECCD current injected is characterised by a large deposition profile d as table 4.3 indicates whereas the experimental decay evolution suggests that the marginal island width at stabilisation measures roughly $W_{\mathrm{marg,ECCD}} \approx W_{\mathrm{sat}}/2$.

4.4 Consistency of the scaling between ASDEX Upgrade and JT-60U

As mentioned in chapter 2, the fitting coefficient c_{sat} is expected to be a constant value among all the discharges. One of the most important aspects in order to robustly evaluate this coefficient is to understand how the measured quantities are consistently related to each other. In general, the local values are calculated at the mode position inferred from the ECE measurement, which is at about $\sim 0.4 - 0.5a$ for the (3,2)-NTMs and $\sim 0.6 - 0.7a$ for the (2,1)-NTMs in both machines. Once the mode position is estimated, all the plasma parameters required for the Modified Rutherford Equation are determined by interpolating the profiles at this position in the plasma. The calculated value of the radius at the resonant surface r_{res} m is ≈ 0.25 m for (3,2)-NTMs and ≈ 0.3 m for the (2,1)-NTMs at ASDEX Upgrade and $\approx 0.35 - 0.4$ m for (3,2)-NTMs and ≈ 0.6 m for (2,1)-NTMs at JT-60U. The local electron density at ASDEX Upgrade is in the usual H-mode scenario used for NTMs' experiments $n_e \approx 5.5 \cdot 10^{19}\, m^{-3}$ and the local electron temperature T_e and the ion temperature T_i are $\approx 1.5 - 2$ keV. In JT-60U, the electron density is lower than at ASDEX Upgrade and it is in the range $n_e = 2 - 3 \cdot 10^{19}\, m^{-3}$, the electron temperature is in the range $T_e \approx 1 - 4$ keV and ion temperature is in the range $T_i \approx 1 - 6$ keV. In general, as far as the kinetic profiles are concerned (as shown in chapter 3), local values are smaller for the (2,1)-NTMs than for the (3,2)-NTMs since the (2,1)-NTM resonant surface lies more outside than the (3,2)-NTM one. The absolute values for the gradient lengths are $L_{\mathrm{ne}} \approx 1 - 2$ m ,$L_{\mathrm{Te}} \approx 0.3 - 0.4$ m ,$L_{\mathrm{Ti}} \approx 0.2 - 0.3$ m in both machines. The absolute value of the gradient length L_q of the safety factor q at ASDEX Upgrade is ≈ 0.3 m for the (3,2)-NTM and ≈ 0.2 m for the (2,1) NTM whereas in JT-60U it is in both types of NTMs $L_q \approx 0.5$ m (the safety factor profile is systematically less steep towards the edge in comparison with ASDEX Upgrade as discussed in chapter 3). The resistive time τ_s lies in the range $1 - 1.5$ s at ASDEX Upgrade whereas in JT-60U it is higher for the (3,2) NTMs $\tau_s \approx 8 - 9$ s and lower for the (2,1) NTMs ≈ 3 s.

4.4.1 Linearity among β_p, W_{sat} and j_{BS}

One of the main trends which has been analysed is the linear intrinsic dependence among the island width at saturation W_{sat}, the local β_p and the local value of the bootstrap current density j_{BS} which has been mentioned in chapter 2 and how this dependence is fulfilled given the independent measurements of the kinetic profiles, island width at saturation and the poloidal magnetic field. This trend is important since it gives an idea of how strong the assumption $W_{\mathrm{sat}} >> W_{\mathrm{marg}}$ applies to our database. This would mainly make the analysis more independent of the small island physics and therefore the determination of c_{sat} more robust. In chapter 3, the measurements for the saturated island width W_{sat}, the quanti-

ties that enter in the calculation of the local $\beta_p = \frac{2\mu_0 < p >}{B_{\rm pol}^2}$ and in the calculation of the local bootstrap current density $j_{\rm BS} \sim \epsilon^{1/2} \frac{p}{B_{\rm pol}} (\frac{n_e}{n_e'} + \frac{T_e}{T_e'})$ have already been presented. In figure 4.9, the normalised saturated island width $W_{\rm sat}/a$ vs. the local β_p , the normalised saturated island width $W_{\rm sat}$ vs. the local bootstrap current density $j_{\rm BS}$ calculated from ASTRA are shown in the first, second and third plot respectively. The dependency of $W_{\rm sat}/a$ versus the local β_p and the local $j_{\rm BS}$ is different for the (2,1) NTMs and (3,2) NTMs both at ASDEX Upgrade and JT-60U and this is due to the fact that the island width is also influenced by the local shear present at the resonant surface. The trend in the linear scaling is very clear for the (2,1) NTM discharges: the (2,1) NTMs under analysis are very large, are positioned more towards the edge of the plasma and therefore their profiles clearly show the effect of the presence of the associated magnetic island (e.g clear flattening in the pressure profile). On the other hand, the linear scaling for the (3,2) NTM discharges is less conclusive: the values of $j_{\rm BS}$ are affected by the plasma equilibration during the relaxation times of the plasma profiles in the transport simulations and no clear linear scaling is found between β_p and $j_{\rm BS}$. In addition, for ASDEX Upgrade discharges with a higher β ($>$ #18690) the island width at saturation $W_{\rm sat}$ is on average smaller than in JT-60U for the same local β_p and $j_{\rm BS}$; this may be due to different reasons:

- the discharges under question are characterised by a frequency $f \sim 16$ KHz just below the sampling frequency of the ECE diagnostic leading to a higher uncertainty in the measurement of $W_{\rm sat}$.
- the condition $\frac{W_{\rm sat}}{W_{\rm marg}} >> 1$ which underlies the dependency $W_{\rm sat} \approx \beta_p / \Delta'$ is not entirely valid since in these discharges $\frac{W_{\rm sat}}{W_{\rm marg}} = 2 \div 3$ and an indication is given by the comparison with the Mirnov coil plotted in figure 4.7 which shows that for these discharges $W_{\rm sat}$ may have been overestimated when measured directly with ECE.
- the (3,2) NTM discharges at JT-60U whose island size varies sharply with β_p and $j_{\rm BS}$ have a wider range of variation of the $P_{\rm NBI}$ power at which the mode saturates and this leads to clearer differences in the kinetic profiles and in the magnetic island width.

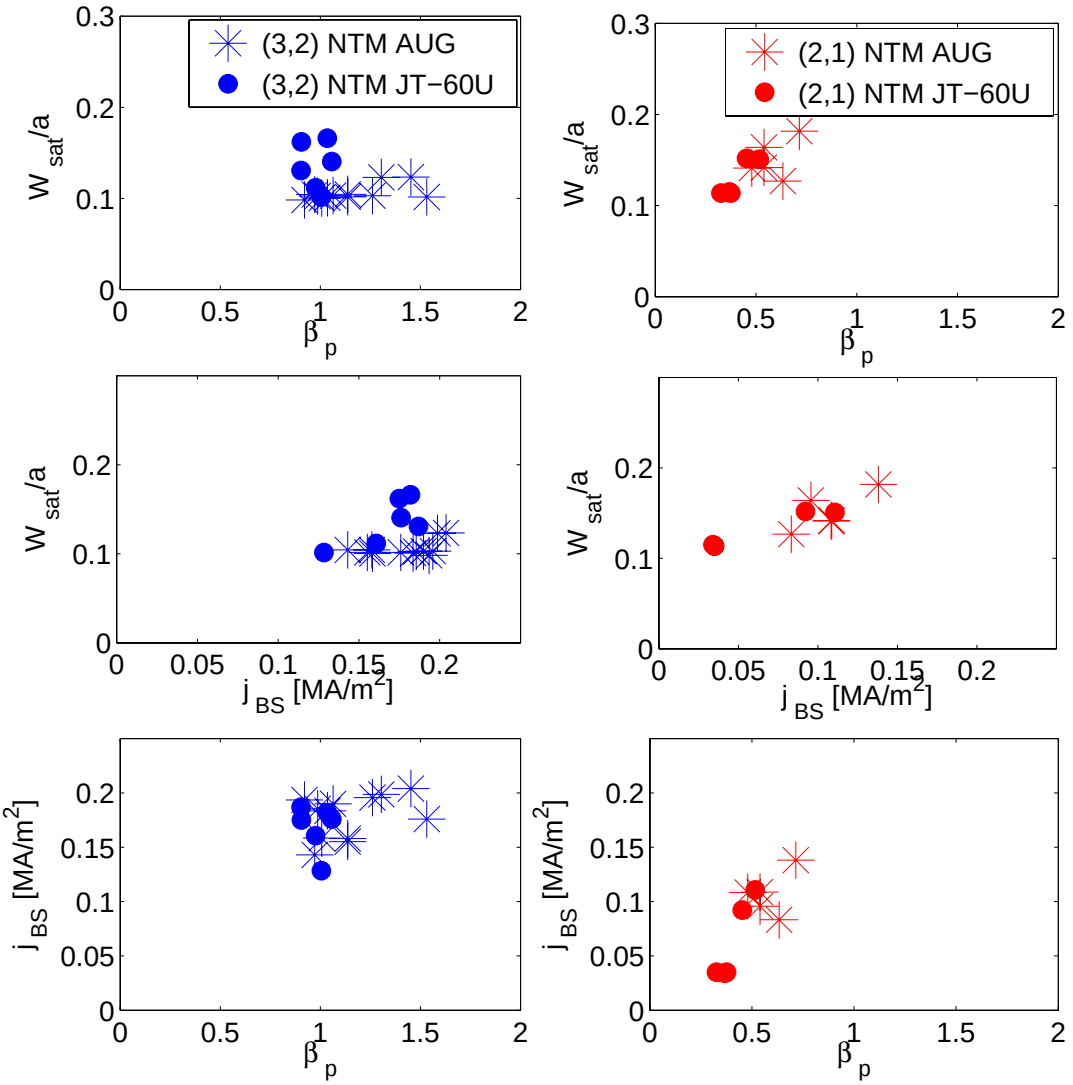

Figure 4.9: Scaling consistency among the normalised saturated island width W_{sat}/a and the local β_p, the normalised saturated island width W_{sat}/a and the local bootstrap current density j_{BS}, the local β_p and the local bootstrap current density j_{BS} for (3,2) NTMs at AUG (blue stars) and at JT-60U (blue dots) and (2,1) NTMs at AUG (red stars) and (2,1) NTMs at JT-60U (red dots). The linear trend is very clear in case of the (2,1) NTMs whereas for the (3,2) NTMs it is less conclusive. However, for some discharges of ASDEX Upgrade W_{sat} of the (3,2) NTM is determined with less accuracy. The (2,1) NTMs are also more easily measurable since they are larger and sit more outside towards the edge of the plasma. In addition, the values of j_{BS} are slightly dependent on the time evolution of the current diffusion during the transport simulations. Also, differences in the kinetic profile determination (the database collects discharges which were run over a time of 5 years) and differences in the local plasma characteristics (for the same β_N) should be taken into account.

Chapter 5

Fitting of c_{sat} and c_{stab}

The type of analysis applied to the set of NTM stabilisation experiments with ECCD described in chapter 4 in order to evaluate the two fitting coefficients c_{sat} and c_{stab} is done in the following steps:

a) the required plasma parameters at t_{sat} are measured

b) the coefficient c_{sat} is calculated

c) the calculated c_{sat} is inserted in the Modified Rutherford equation 2.49 and the Δ'_{ECCD} term is 'switched' on

d) the required plasma parameters at t_{ECCD} are measured

e) the coefficient c_{stab} is evaluated by integrating the $\frac{dW}{dt}$ and by matching the experimental time evolution $W(t)$ from the Mirnov coil signal

In chapter 2 and 3, points a and d have been addressed. In the following chapter, instead, points b, c and e, that is the technique adopted for fitting of c_{sat} and c_{stab} together with the fitting results are presented and discussed.

5.1 Determination of c_{sat}

c_{sat} is the coefficient included in the Modified Rutherford equation 2.49 accounting for the uncertainty in the cylindrical assumptions underlying the theoretical model for the NTMs and for possible missing physics at saturation which is not included in the Modified Rutherford equation. It is calculated by considering equation 2.49 and by setting $dW/dt = 0$ and $W = W_{sat}$ when the ECCD current is not yet injected in the plasma, that is $\Delta'_{ECCD} = 0$. Therefore, the equation which

needs to be solved is:

$$c_{sat} = \frac{-\Delta'}{\Delta'_{BS} + \Delta'_{GGJ}} = \tag{5.1}$$
$$= -\Delta' / \left(\frac{6.34}{2} \mu_0 L_q \frac{j_{BS}}{B_{pol}} \left(\frac{W_{sat}}{W_{sat}^2 + W_d^2} + \frac{W_{sat}}{W_{sat}^2 + 28 W_b^2} \right) - \frac{6.35 \mu_0 D_R}{\sqrt{W_{sat}^2 + 0.65 W_d^2}} \right)$$

where $\Delta' = -1.97 \frac{1}{a}(1 + 23.1 \frac{W}{a})$ in the case of (3,2) NTMs and $\Delta' = -m / r_{res}$ in the case of (2,1) NTM. The fitting results for the determination of c_{sat} using the collected database of discharges from ASDEX Upgrade and JT-60U are shown in figure 5.1.
The two important results are that:

- c_{sat} has a mean value 0.81 ± 0.13 and is found to be a constant value of the order of unity for both ASDEX Upgrade and JT-60U discharges
- c_{sat} is found to be independent over a large range of values in which the determining plasma parameters such as β_p, j_{bs}, L_q and W_{sat} are measured

These results confirm the theoretical expectations presented in chapter 2 although, given the type of measurements involved, the scatter in the value of c_{sat} is quite large. One has to consider that in equation 5.1, the dominant competing effects are the modification of the equilibrium current profile (modelled by Δ' at the numerator) and the missing of the bootstrap current density (modelled by Δ'_{BS} at the denominator). Therefore, c_{sat} is mainly a measure of the uncertainty on the strength of these two mechanisms since at saturation for $W_{sat} >> W_{marg}$ all the other small island effects are negligible. As already discussed, the effect of Δ' is mostly unknown in the Rutherford equation since the cylindrical approximation which is used in the model does not take into account possible important effects due to toroidicity. The main difference between (3,2) NTMs and (2,1) NTMs in the model is the linear dependence of Δ' on the island width W. This effect is included for the modelling of the (3,2) case but not in the (2,1) case. This is, however, a small difference since for a (3,2) NTM, $r_{res}\Delta'(W_{sat}) = -3.33$ which only affects $r_{res}\Delta'$ by $\sim 10\%$ at saturation so that, in principle, the uncertainty on $r_{res}\Delta'$ is entering in c_{sat} as a constant value for all the discharges. For example, the (2,1) NTM discharges for ASDEX Upgrade have consistent values of c_{sat} if the value of $r_{res}\Delta'$ is set to $r_{res}\Delta' = -1$. This value is somehow unexpected as closer to the vacuum the cylindrical approximated formula 2.29 is assumed to be more valid. On the other hand this could be questioned by the fact that for very strong (2,1) NTMs, as in this case, even the Δ' may start being close to be destabilising as the bootstrap current density inside the island is almost totally missing. In addition, for some references where similar analysis was carried out [Petty(2004)] the value of Δ' for (2,1) NTM has also been set to values close to unity ($r_{res}\Delta' \approx -1.3$). At

JT-60U, instead, the (2,1) NTM discharges are fitted with $r_{res}\Delta' = -2$ but, as mentioned in chapter 4, these discharges are characterised by a co-existance between a (2,1) and a (3,2) NTM, so that the discrepancy in $r_{res}\Delta'$ between the two devices needs to be considered in light of the fact that at ASDEX Upgrade the (2,1) NTM is very unstable whereas at JT-60U the present mode coupling is not fully considered when using the simplistic cylindrical approximation for $r_{res}\Delta'$. The other source of error for c_{sat} comes from the Δ'_{BS} term and this basically reflects the uncertainty in the linear scaling between W_{sat}, j_{BS} and β_p, which, as already discussed in chapter 4, is very robust for the (2,1) NTMs and has a less clear trend for the (3,2) NTMs. As figure 5.1 shows, in fact, for some (3,2) NTMs discharges of ASDEX Upgrade (blue stars) the range in which c_{sat} changes is quite large compared to the small range of variation for W_{sat}. On one hand, this is the effect of the uncertainty on the island width measurement and from the physics point of view it can indicate that for these discharges the assumption $W_{sat} >> W_{marg}$ does not fully apply and that small island physics plays a stronger role for these shots.

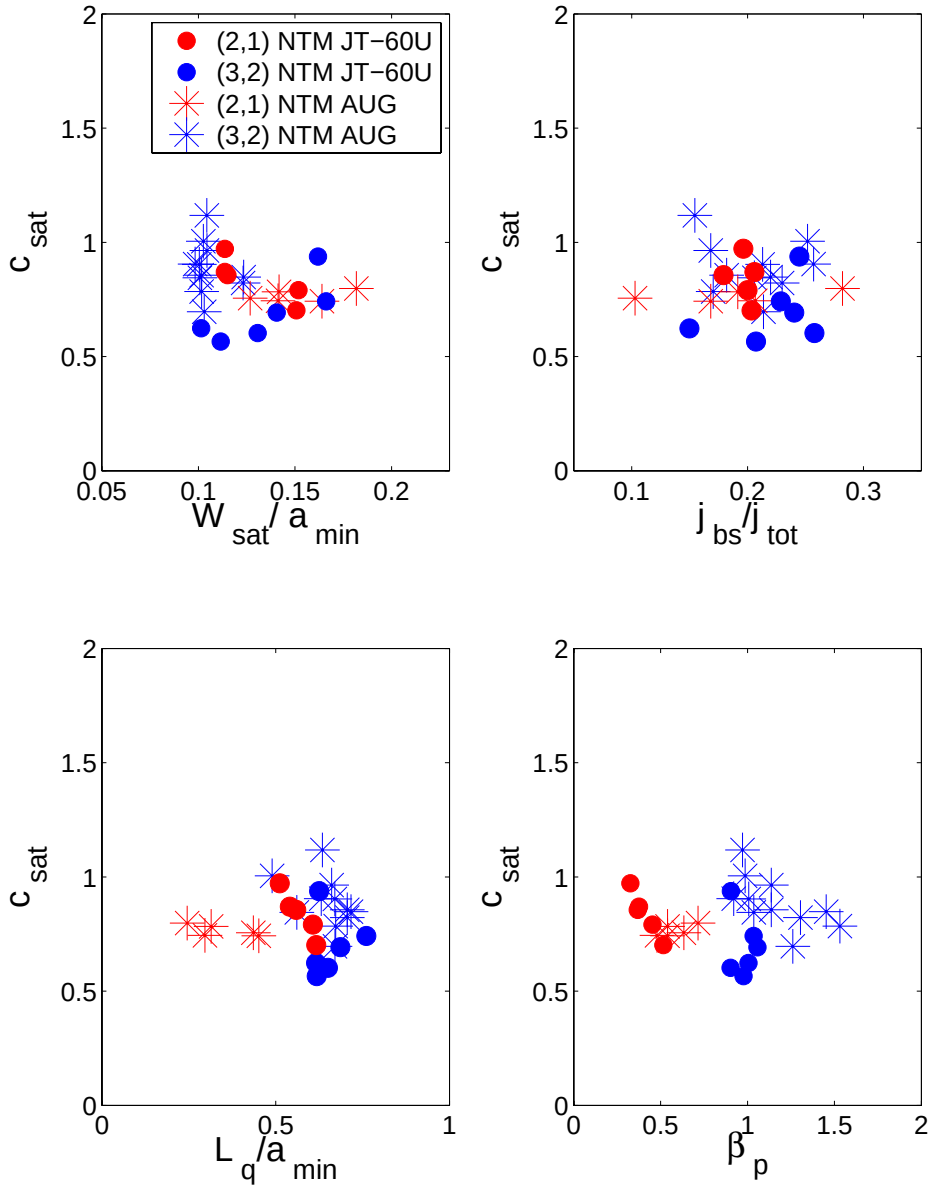

Figure 5.1: Determination of c_{sat} for the complete database from ASDEX Upgrade and JT-60U discharges: the calculated values of c_{sat} lie in the range $0.5 \div 1$ and show to be independent over a large range of values for the normalised quantities j_{BS}/j, W_{sat}/a, L_q/a and β_p. This is very clear for the (2,1) NTMs discharges of ASDEX Upgrade (red stars) which are the best diagnosed ones. On the other hand, for some (3,2) and (2,1) NTM discharges, the scatter in the values of c_{sat} is quite large and this mainly reflects the uncertainty in the linear scaling among W_{sat}, j_{BS} and β_p (discussed in chapter 4) and the theoretical uncertainty in the model for Δ'.

5.2 Determination of c_{stab}: integration of the Modified Rutherford equation

c_{stab} is the coefficient in equation 2.49 to consider the uncertainty in the modelling of the ECCD stabilisation term Δ'_{ECCD} and it mainly accounts for toroidal corrections to the cylindrical derivation [Giruzzi(1999)], [Morris(1992)]. It can be calculated from the Modified Rutherford Equation once c_{sat} has been evaluated and by switching on the Δ'_{ECCD} term:

$$c_{stab} = \frac{\frac{\tau_s}{r_{res}}\frac{dW}{dt} - \Delta' - c_{sat}(\Delta'_{BS} + \Delta'_{GGJ})}{\Delta'_{ECCD}} \tag{5.2}$$

The determination of c_{stab} using equation 5.2 has two take into account two main aspects:

- the decay rate can be different from zero $\frac{dW}{dt} \leq 0$ since the condition $dW/dt = 0$ is only valid in case of marginal stabilisation
- it is necessary to make some assumptions on the experimental value of the radial misalignment $x_{mis} = r_{dep} - r_{res}$ (which enters via the efficiency function $\eta(W/d, x_{mis})$ as mentioned in chapter 2) and on the marginal island width $W_{marg,ECCD}$ after which the mode decays spontaneously

Useful information on x_{mis} and $W_{marg,ECCD}$ can be gained from the experimental island width evolution $W(t)$ provided by the Mirnov coil signal, as described in chapter 3. Therefore, the approach used for determining the fitting coefficient c_{stab} has been to simulate the island width time evolution by integrating the Modified Rutherford equation $\frac{dW}{dt} = (r_{res}/\tau_s)(\Delta' + ...)$ by setting the values of $(c_{stab}, x_{mis}, W_{marg,ECCD})$ which best allow the matching between the simulated curve and the experimental one. The integration of the Modified Rutherford equation $W(t) = \int_{t_{ECCD}}^{t_{sat}} \frac{dW}{dt}\, dt$ is done numerically using a Runge-Kutta integration over the decay time $\Delta t = |t_{ECCD} - t_{sat}|$ during which the island from its saturated value W_{sat} shrinks to zero because of the injection of ECCD. The numerical scheme adopted for simulation of the island evolution in time is presented in figure 5.2 where the cases of fixed misalignment (JT-60U) or misalignment changing in time (ASDEX Upgrade) are described.

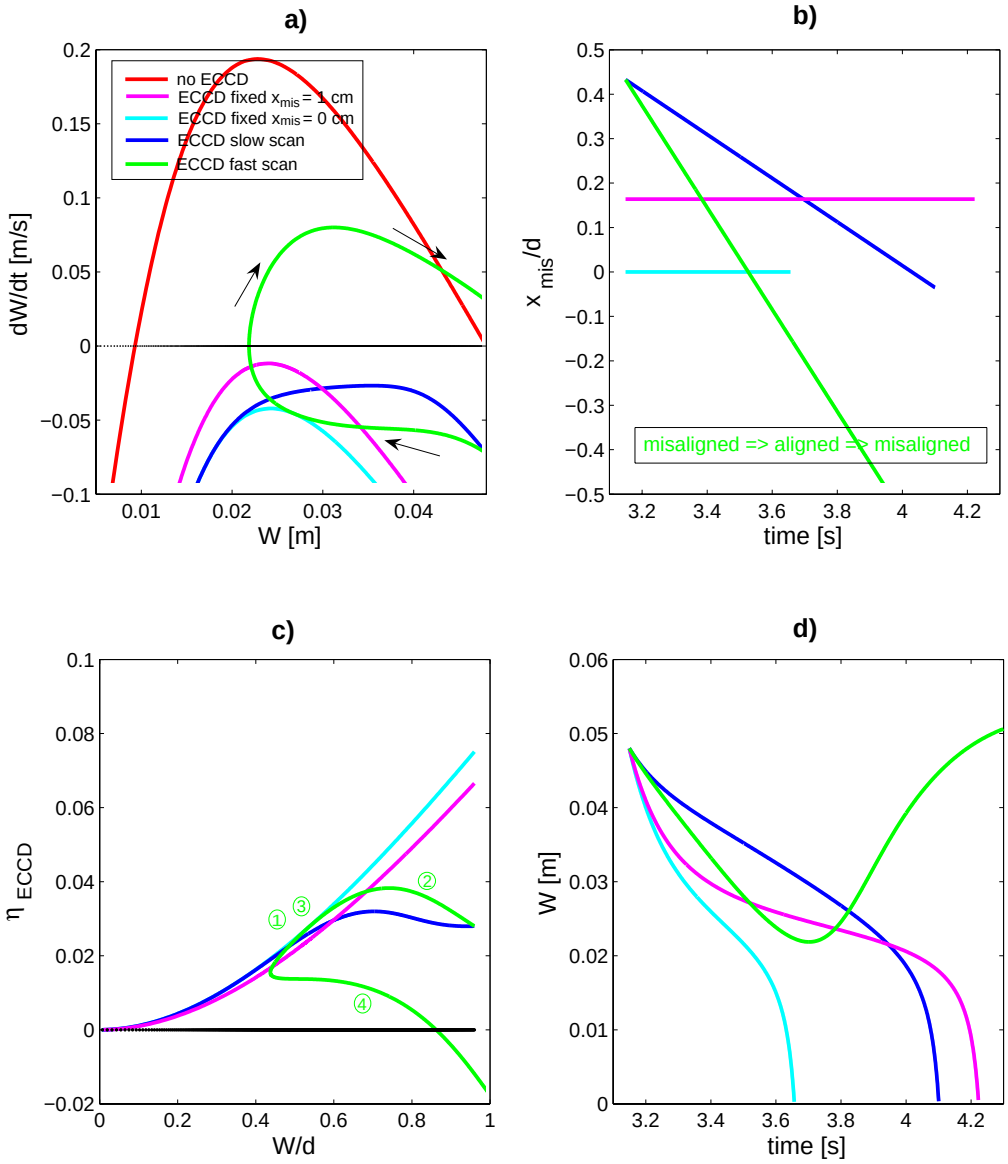

Figure 5.2: Simulation of the island time evolution during ECCD injection for a fixed value of c_{stab} and different misalignment. In (a) the phase diagram $(dW/dt, W)$ is obtained with the Modified Rutherford equation 2.49 in case of no ECCD injection (red curve) and in the cases when ECCD is switched on and the mode starts to be controlled (other curves). For the 4 different cases of radial misalignment x_{mis} the behaviour of the η_{ECCD} during the stabilisation is shown in (c) and the consequent simulated island width decay is shown in (d). The magenta and cyan curves are the cases in which x_{mis} is set constant to 0 or 1 cm whereas the blue and the green curves are the cases in which x_{mis} is varied linearly in time from an initial value x_{mis0} with a certain velocity v. In case the velocity of the scan is too fast, the mode first decreases but once the resonant surface of the mode is largely overcome starts to increase again and the η_{ECCD} becomes negative.

5.3 Fitting of c_{stab} at ASDEX Upgrade

ASDEX Upgrade discharges for NTMs' stabilisation with ECCD are characterised by a linear ramp of the toroidal magnetic field B_T which scans the plasma till it crosses the resonant surface of the NTM where the radial misalignment $x_{mis} = r_{dep} - r_{res}$ becomes zero. This experimental method for hitting the resonant surface is modelled in the Modified Rutherford equation by assuming a linear change in time of the radial misalignment $x_{mis}(t) = x_{mis0} - vdt$ starting from an initial value x_{mis0} and evolving in time with a certain velocity v which is related to the velocity of the magnetic field scan. In the simulations of the NTM stabilisation process, the initial value of the radial misalignment is estimated for each discharge by calculating with TORBEAM at each time point the shifting radial position of position of the injection r of the ECCD beam till $r_{dep} = r_{res}$. The resonant surface of the mode during the scan of B_T is found at $B_T \sim -1.8 \div 1.85$ T for the (2,1) NTMs and at $B_T \sim -2.1 \div 2.15$ T for the (3,2) NTMs. The velocity of the scan is set for all discharges to $v = 0.05\ m/s$ and it corresponds to a radial scan through the plasma of $\Delta r \approx 10$ cm during the 2 s in which the ECCD is on and the magnetic field ramp is changed of the amount $\Delta B_T = |0.2|$ T [Maraschek(2004)]. The determination of c_{stab} for the ASDEX Upgrade discharges is characterised by a difference in the experimental evolution of the magnetic island width $W(t)$ between the discharges with large deposition profile of the ECCD beam ($d > 4$ cm) and those with small deposition profile ($d < 4$ cm). In particular, the discharges for NTM stabilisation with large deposition profile of the ECCD (corresponding to toroidal injection angle between $10^\circ < \phi < 15^\circ$ in table 4.2) are characterised by an experimental slower decay of the magnetic island width $W(t)$ compared to the small deposition experiments where, as figure 5.3 shows, for a long time during ECCD injection, the island width stays constant till it rapidly decays. This effect is expected since in case of large deposition profile experiments the

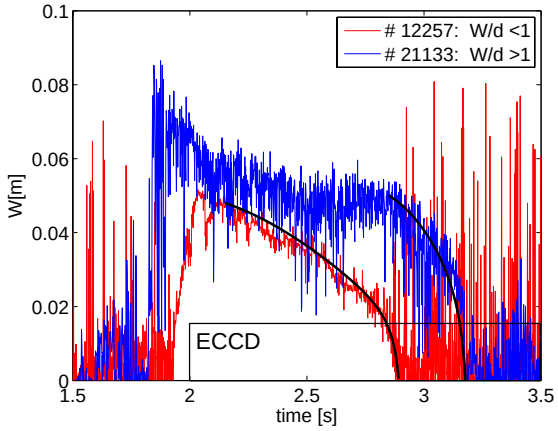

Figure 5.3: Island width decay in case of small (blue) and large (red) deposition profiles of ECCD injection beam at ASDEX Upgrade: during the ECCD phase, for the small deposition profile case (#21133) the mode remains saturated for longer time before it decays as the ECCD needs to be well inside the island to be effective.

stabilisation mechanism can happen earlier as the relative distance between the O-point of the island and the ECCD beam is smaller. Instead, in case of small deposition profile experiments, the ECCD beam needs to be well inside the island before it can become effective. Indeed, as mentioned in chapter 2, as the ECCD beam overlaps the island, an initial phase in which the ECCD is negative should take place and a destabilising effect should be visible from the Mirnov coils and this is not observed.

5.4 Fitting of c_{stab} at JT-60U

JT-60U discharges for NTM stabilisation with ECCD are characterised by large deposition width profiles $d \approx 7 \div 10$ cm and by a fixed ECCD location of injection (the slight variation due to the mirror tilting described in 4 is only $2-3\%$) so that in the simulations the value of the radial misalignment x_{mis} is set to a constant value. Most of the (3,2) NTM simulations have been carried out assuming the misalignment to be $x_{mis} = 2$ cm. In the case of both the (3,2) NTM and (2,1) NTM discharges, the value $x_{mis} = 2$ cm is partially supported by the electron temperature profile measurements during the ECCD phase which show a local increase of the temperature 2 cm away from the O-point of the magnetic island for #41666 and this is an upper limit to the possible values for misalignment for which complete stabilisation still occurs in the simulations. In addition, for the (2,1) NTM discharges, the experimental island width signal from the Mirnov coils shows a rapid decay at a value of the marginal island width W_{marg} which significantly deviates from the values calculated by using the W_d or W_b models which give values of the order of 1.5-2.5 cm; therefore, for these cases, W_{marg} is set to a realistic value of half of the saturated island width $W_{marg} \sim W_{sat}/2$.

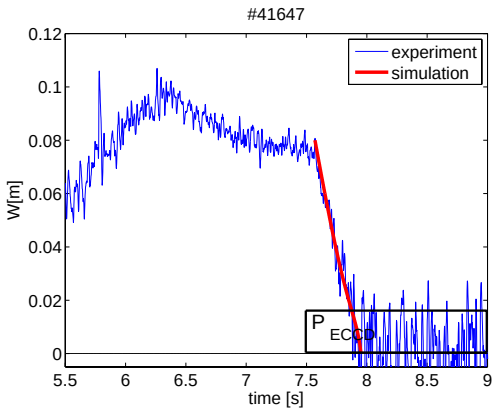

Figure 5.4: Fitting of the (3,2) NTM experimental evolution (#41647 with $c_{stab} = 1.2$, $x_{mis} = 0.02$ cm). In JT-60U mode decay occurs as soon as ECCD is switched on due to optimised injection position

5.5 c_{stab}: comparison between ASDEX Upgrade and JT-60U discharges

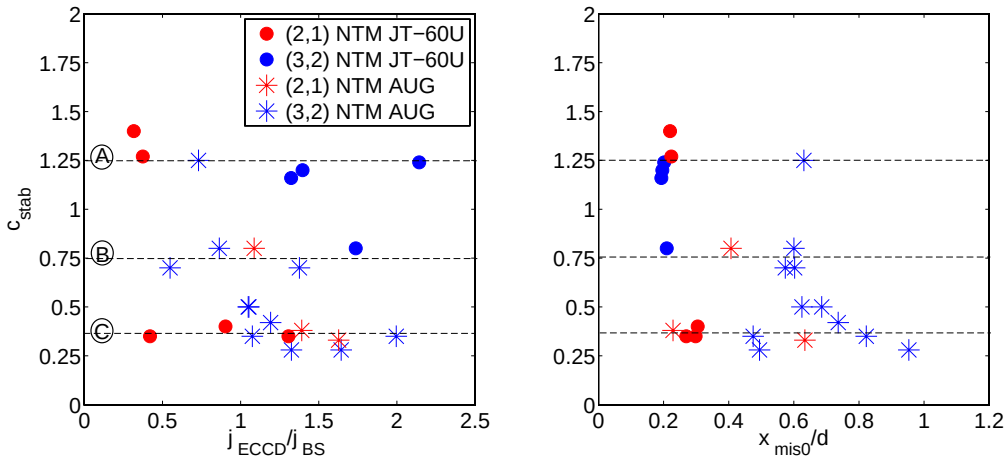

Figure 5.5: Initial fitting results for c_{stab} plotted versus $\frac{j_{ECCD}}{j_{BS}}$ (left) and $\frac{x_{mis0}}{d}$ (right) obtained considering a symmetrical island ($\gamma = 1$) and by assuming for JT-60U discharges a radial misalignment $x_{mis} = 2$ cm. Three different trends are found for the value of c_{stab} among the discharges: a group of discharges (A) characterised by an upper value $c_{stab} = 1.25$, a group (B) characterised by an intermediate value around $c_{stab} = 0.75$ and a group of discharges (C) characterised by a lower value for c_{stab} between $0.25 \div 0.5$.

The fitting results for c_{stab} at ASDEX Upgrade and at JT-60U applying the fitting technique outlined in section 5.2 are presented in figure 5.5, in which the results for c_{stab} are plotted versus two important parameters $\frac{j_{ECCD}}{j_{BS}}$ and $\frac{x_{mis0}}{d}$. As mentioned in chapter 2, these two figures of merit give an idea of how optimised is each of the NTM stabilisation experiments with ECCD in terms of amount of ECCD current used to stabilise the NTM and misalignment x_{mis} present during stabilisation. The first observation from figure 5.5 is that c_{stab} is characterised by three different constant values for three groups of discharges:

- group A with $c_{stab} = 1.25$
- group B with $c_{stab} = 0.75$
- group C with $c_{stab} = 0.25 \div 0.5$

The discharges that belong to group A are the (2,1) NTM discharges (#46) from JT-60U stabilised with the fundamental O-mode of the ECRH, the (3,2) NTM stabilisation discharges of JT-60U (#41) and one discharge from ASDEX Upgrade (#17977); group B is formed by the ASDEX Upgrade discharges #12257, #13631,

#18691, #19283 and the (3,2) NTM discharge #41652 from JT-60U; group C, instead, is formed by the (2,1) NTMs discharges (#47) stabilised with 2^{nd} harmonic of X-mode at JT-60U and the ASDEX Upgrade discharges ($>$ #18) characterised by a high ratio $\frac{j_{ECCD}}{j_{BS}}$ and small deposition profile $\frac{W_{sat}}{d} > 1$. The discharges belonging to group B are the best optimised ones over the whole database as they have a low ratio $\frac{j_{ECCD}}{j_{BS}}$ and small misalignment x_{mis} for a given $\frac{W_{sat}}{d}$. However, the discrepancy among the values of c_{stab} in figure 5.5 is quite large and in order to understand what are the main reasons for the large scatter in the values of c_{stab} among the groups of discharges indicated above, various aspects which affect the determination of c_{stab} are analysed and their importance in the evaluation of a consistent c_{stab} over the database is weighted in the following sections.

5.5.1 c_{stab}: dependency on geometry effects

In this section, the geometry effects which may play a role in the evaluation of c_{stab} are investigated. In general, the two major geometric effects which arise during stabilisation and which are not covered in the stabilisation term in equation 2.49 are:

1) the real asymmetric shape of the magnetic island described by introducing the asymmetry factor γ in the evaluation of the efficiency function η_{ECCD}

2) the difference in the value of the island width W_{sat} between the low-field side (LFS) (where the island width is measured by ECE) and the high-field side (HFS) (where the current to stabilised the NTM is injected during the experiment)

The first point has been already introduced in chapter 2 and affects the efficiency function in a way that stabilisation will be less effective the more the island has an asymmetric shape. An estimate of the real asymmetric shape of the magnetic island suggests that a factor $\gamma = 0.5$ can be considered as a good approximation for the island shape. The second point, instead, deals with the fact that, both at ASDEX Upgrade and JT-60U, although the stabilisation with ECRH occurs on the HFS, the measurement of the island width by ECE occurs on the LFS. Therefore, in the calculation of the efficiency function η_{ECCD} the saturated island width which needs to be taken into account is the one on the HFS. In order to give an estimate of the island width on the HFS $W_{sat,HFS}$, the difference in the projection on the mid-plane of the two limiting flux surfaces of the island width measured at the LFS $W_{sat,LFS}$ is related to the island width on the HFS by a factor f:

$$\frac{W_{sat,HFS}}{W_{sat,LFS}} = f \tag{5.3}$$

If one assumes that the β-dependence comes from the Shafranov shift, as the β value increases, the 'density' of the contour lines of the equilibrium will increase and the factor f will be larger. As an example, figure 5.8 and figure 5.7 show for ASDEX Upgrade and JT-60U that for a $\beta_N = 1.8$ and $\beta_N = 1.5$ the island width measured on the HFS is a factor $f \approx 1.5$ and $f \approx 1.2$ larger than on the LFS. In table 5.1, for two ASDEX Upgrade discharges and two JT-60U discharges, the values of the island widths at LFS and HFS are listed together with the factor f and since in ASDEX Upgrade the discharges have a higher β-value, the conversion factor f is larger. In order to account for this geometric effect in the fitting of c_{stab}, the mean values $f = 1.55$ and $f = 1.25$ from table 5.1 are set for ASDEX Upgrade and JT-60U discharges respectively.

Table 5.1: Factor f between island size on LFS and HFS

discharge	$W_{sat,LFS}$	$W_{sat,HFS}$	f
18036 (3,2)	0.06	0.09	1.5
19454 (2,1)	0.09	0.14	1.6
41666 (3,2)	0.11	0.13	1.2
46368 (2,1)	0.12	0.15	1.3

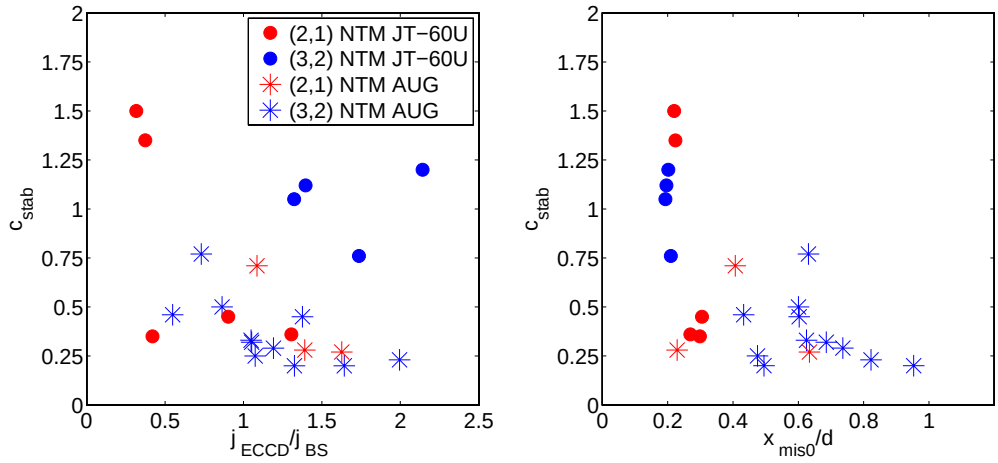

Figure 5.6: Fitting results for c_{stab} obtained considering for the calculation of the efficiency function η_{ECCD} the island width measured on the HFS $W_{sat,HFS}$ and an asymmetrical island ($\gamma = 0.5$): the discrepancy among the ASDEX Upgrade discharges improves whereas the JT-60U discharges show no clear change due to geometric factors such as asymmetry of the magnetic island and difference in HFS-LFS estimate of W_{sat}.

The estimate of c_{stab} by taking into account the real shape asymmetry and the HFS factor is shown in figure 5.6: the scatter in the value of c_{stab} among the ASDEX Upgrade discharges decreases as for discharge #17977 c_{stab} changes from

1.25 to about 0.8 and the (3,2) NTM discharges lying at around $c_{stab} = 0.75$ shift towards $c_{stab} = 0.5$. On the other hand, the JT-60U discharges are not affected so much by the change in the value of the efficiency function given a more realistic island width measure since the increased efficiency due to a larger $\frac{W_{sat,HFS}}{d}$ is counteracted by the loss of efficiency due to asymmetry.

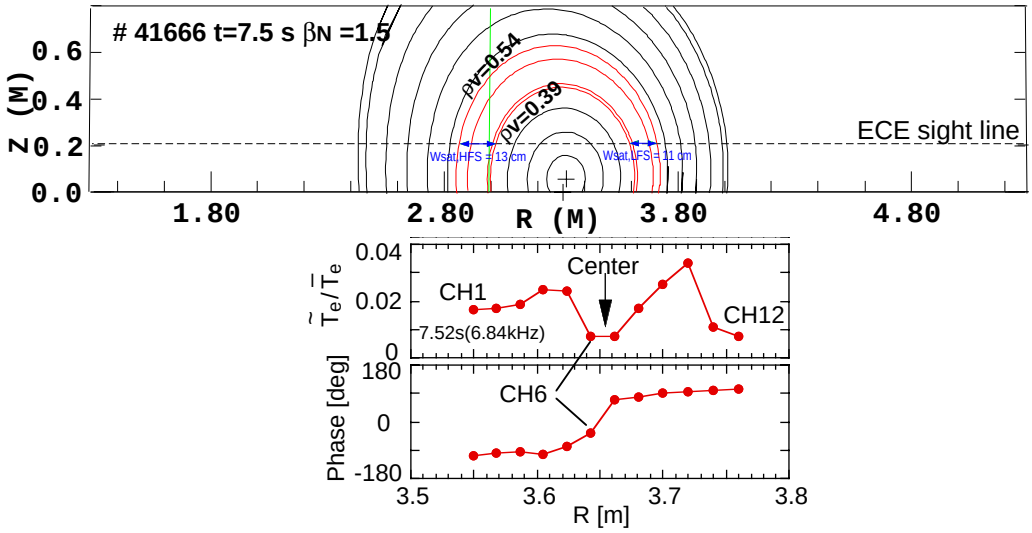

Figure 5.7: Measurement of the factor f for discharge #41666 at JT-60U: for $\beta_N = 1.5$ and (3,2) NTM the island width on the HFS is 13 cm whereas on the LFS it is 11 cm. The FFT signal shows the asymmetry between the two sides of the island.

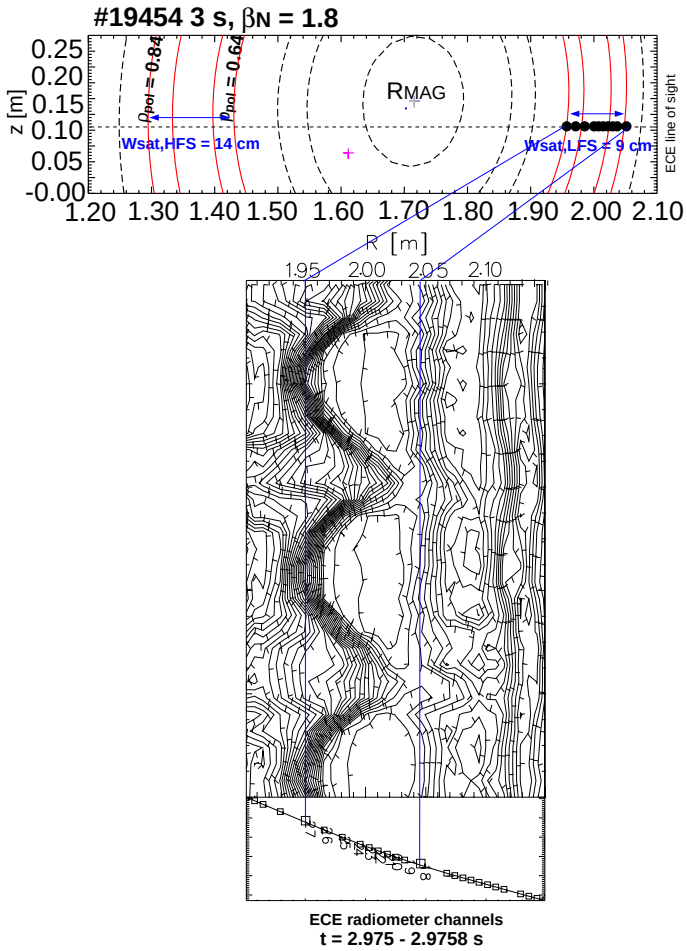

Figure 5.8: Measurement of the factor f for discharge #19454 at ASDEX Upgrade: for $\beta_N = 1.8$ and (2,1) NTM the island width on the HFS is 14 cm whereas on the LFS it is 9 cm. The contour plot of the island shows the asymmetry between the two sides of the island.

5.5.2 c_{stab}: dependency on radial misalignment and over-stabilisation

The fit for c_{stab} obtained considering the geometric corrections still presents a considerable scatter over the whole database of discharges. However, once the geometric effects have been accounted in the fit for c_{stab}, the only two other possible reasons for the discrepancy in its values are that:

3) the ratio j_{ECCD}/j_{BS}, in case of small deposition profile discharges $\frac{W_{sat}}{d} > 1$ is far away too high to clearly be able to isolate the value of c_{stab} independently from it

4) the value of radial misalignment x_{mis} which is considered for the fit is estimated with a high uncertainty and small changes of its value can largely affect the evaluation of c_{stab}

In ASDEX Upgrade, as mentioned in chapter 4, the radial misalignment is robustly measured since the linear change in the toroidal magnetic field B_T is directly proportional to the shift in the radial position of the ECCD beam and, therefore, point 4 is not expected to be relevant. On the other hand, indication that point 3 may influence the determination of c_{stab} is provided by noticing that for ASDEX Upgrade figure 5.5 and 5.6 show that:

- the discharges with lowest c_{stab} are those characterised by a value of $\frac{j_{ECCD}}{j_{BS}} > 1$ given a misalignment of about 2-3 cm (see table A.1 in the Appendix)
- the discharge with highest value of c_{stab} is #17977 which is only marginally stabilised during the experiment and is characterised by $\frac{j_{ECCD}}{j_{BS}} = 0.7$, very poor initial alignment $x_{mis} = 0.05$ m and a large deposition profile $\frac{W_{sat}}{d} < 1$ (figure A.1 in the Appendix). This indicates that for the discharges with smaller misalignment $x_{mis} < 0.05$ cm and $\frac{W}{d} > 1$ the marginal value $\frac{j_{ECCD}}{j_{BS}}$ will lie well below 0.7.

In general, for JT-60U discharges the misalignment is a much more unknown quantity than in ASDEX Upgrade and for the fitting of c_{stab} an initial value $x_{mis} =$ 2 cm has been considered. However, the very rapid decay of the mode as ECCD is switched on indicates that the misalignment can be even smaller. In addition, in figure 5.5 and 5.6 some other aspects need to be considered:

- the two series of (2,1) NTM stabilisation experiment differ very much in terms of results for c_{stab} although among these there are two discharges which are only marginally stabilised (#46367 and #47796) since the ratio $\frac{j_{ECCD}}{j_{BS}}$ has been explicitly lowered in order to study ECCD marginal power requirements

- one of the (3,2) NTM discharges from JT-60U has a lower c_{stab} value compared to the other (3,2) NTM discharges and is characterised during the stabilisation by a drop of the ECRH power which affects the length of stabilisation (figure A.5 in the Appendix)

The first point is an indication that these discharges may be characterised by a different value of misalignment x_{mis} (e.g assuming 2 cm for all of them may be too simplistic). The second point, instead, suggests that also in the JT-60U case, although not as much as in the ASDEX Upgrade case, over-stabilisation for the (3,2) NTM discharges plays a role in the determination of c_{stab}. Given these arguments, in order to improve the discrepancy of c_{stab} among the discharges, it is reasonable to assume:

- a misalignment $x_{mis} \approx 0$ cm for the JT-60U discharges which have $c_{stab} > 0.8$ in figure 5.6
- a ratio $\frac{j_{ECCD}}{j_{BS}} = 0.5$ for the ASDEX Upgrade discharges which have $c_{stab} < 0.5$ in figure 5.6

The fit for c_{stab} is carried out again under these conditions and the result is plotted in figure 5.9. By assuming perfect alignment for the JT-60U discharges with initial

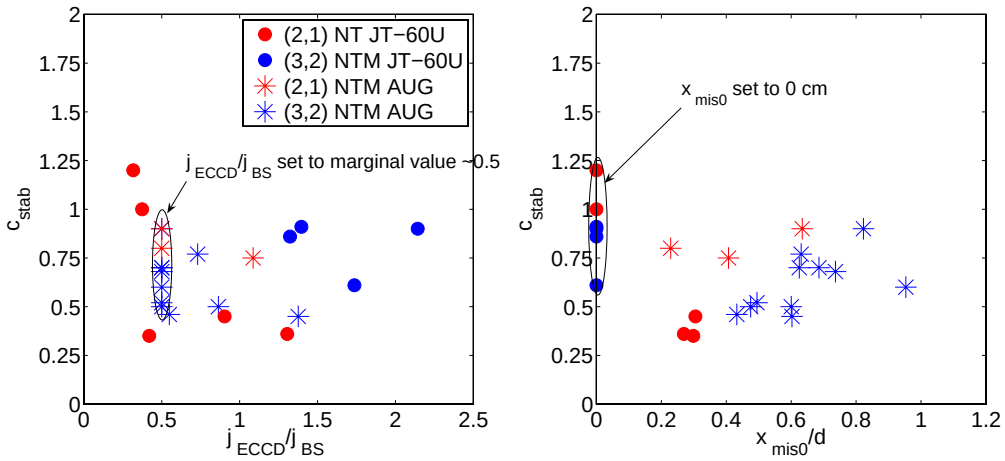

Figure 5.9: Fitting results for c_{stab} obtained by considering for the calculation of the efficiency function η_{ECCD} the island width measured on the HFS $W_{sat,HFS}$ and an asymmetry factor $\gamma = 0.5$ and by accounting for over-stabilisation in case of ASDEX Upgrade and smaller misalignment for group C for JT-60U discharges.

high values of c_{stab}, stabilisation efficiency improves and c_{stab} results to be smaller by a factor 0.7-0.8. In addition, by considering the effect of over-stabilisation for the ASDEX Upgrade discharges, the points with $c_{stab} < 0.5$ shift up leading to

a smaller scatter in the ASDEX Upgrade database. A large discrepancy still remains between the (2,1) NTM discharges of JT-60U: these are, however, the most difficult discharges to analyse as mode coupling is present and one could even argue that for the first set of discharges the (3,2) was stabilised and for the second set the (2,1) was stabilised due to different resonance location of the ECCD injection. Last but no least, the geometry effects, the assumptions on misalignment and over-stabilisation have been treated here quite schematically whereas for each discharge these effects should be weighted differently. In general, some important observations related to the fitting c_{stab} are the following:

- at ASDEX Upgrade the initial misalignment can initially be larger than at JT-60U ($x_{mis0}/d \leq 1.0$).
- at JT-60U it has to be less than half of the saturated island width $x_{mis}/d \leq 0.6$ cm to be stabilising in agreement with ref. [Nagasaki(2003)]
- for ASDEX Upgrade there is a systematical difference between small deposition profiles and large deposition profile discharges which translates into a different behavior in time of the mode stabilisation (Mirnov signal)
- the value of the marginal island width W_{marg} is consistent with W_d or W_b model for all the discharges except for the (2,1) NTM discharges of JT-60U. However these are characterised by the co-existance of (2,1) and (3,2) NTM, therefore the Modified Rutherford equation may be incomplete (an additional term related to the coupling should be included).
- the ratio j_{ECCD}/j_{BS} which marginally stabilises the NTM is $\sim 0.3 \div 0.6$ for $W_{sat}/W_{marg} \approx 2-3$ in both ASDEX Upgrade and JT-60U.
- the mean value of c_{stab} calculated over the whole database is:

$$c_{stab} = 0.68 \pm 0.22 \tag{5.4}$$

Chapter 6

Error analysis for c_{sat} and c_{stab}

In chapter 5, the fitting coefficients c_{sat} and c_{stab} have been calculated for a set of NTM stabilisation discharges from ASDEX Upgrade and JT-60U. The value of these fitting coefficients depends on many plasma parameters which are correlated among themselves and are deteriorated with measurement uncertainty. Therefore, the question arises on how consistently one can give an estimate of the uncertainty on c_{sat} and c_{stab}. In order to approach this problem, an error analysis using a probabilistic method which generalises the standard error propagation technique is developed. The main focus is to investigate how do the measurements on the experimental quantities affect the evaluation of c_{sat} and c_{stab} in the Modified Rutherford equation. The numerical tool which has been developed is able to give together with the fitting coefficients of the Modified Rutherford equation also their standard deviation in the most consistent way.

6.1 Error analysis for the Modified Rutherford Equation using a probabilistic approach

To determine the error on c_{sat} and c_{stab} a probabilistic approach is applied which makes use of the Bayesian Probability Theory (BPT) [Goldstein(2007)]. The Bayes Theorem states that a posterior probability distribution of the event c given the event B can be calculated by multiplying the prior probability distribution $P(c)$ by the likelihood $P(B|c)$ that event B will occur if c is true and its formula is:

$$P(c|B) = \frac{P(B|c)P(c)}{P(B)} \tag{6.1}$$

The likelihood is assumed to be a normal distribution having the form:

$$P(B_i|A) = \frac{1}{\sqrt{2\pi}\sigma_{B_i}} \exp^{-\frac{1}{2}(\frac{B-B_i}{\sigma_{B_i}})^2} \tag{6.2}$$

In this way, the joint probability can be calculated as:

$$p(B|A) = \prod_i p(B_i|A) \tag{6.3}$$

This method applied to the Modified Rutherford equation has several advantages compared to a standard gaussian error propagation since the coefficients c_{sat} and c_{stab} have complex dependencies in the equation 2.49:

$$\begin{aligned} c_{sat} &= c_{sat}(W_{sat}, L_q, j_{BS}, j_{ECCD}.....) \\ c_{stab} &= c_{stab}(W_{ECCD}, L_q, j_{BS}, j_{ECCD}.....) \end{aligned}$$

It also makes possible to consider the physics constraints and the correlations present in the model and to make a sensitivity study on the model to identify which are the most influencing quantities affecting their determination.

6.2 Application to the Modified Rutherford equation

The Bayesian theory is applied to the Modified Rutherford equation written in the form of equation 2.49. $\bar{b}$ is the set of measured data with uncertainties described in chapter 4 and the parameters of interest $\bar{c}$ are the fitting results of chapter 5 for c_{sat} and c_{stab}. The quantities $\bar{B}$ are the true quantities to be measured (e. g. W_{sat}, L_q, j_{BS}, etc.) which are unknown. The marginal probability distribution for c_{sat} and c_{stab} can be obtained by applying the marginalisation theorem and the product rule of BPT:

$$\begin{aligned} p(\bar{c}|\bar{b},\bar{\sigma}) &= \int d\bar{B} p(\bar{c},\bar{B}|\bar{b},\bar{\sigma}) \\ &= \int d\bar{B} \frac{p(\bar{b}|\bar{c},\bar{B},\bar{\sigma}) p(\bar{c},\bar{B})}{p(b,\bar{\sigma})} \\ &\propto \int d\bar{B} p(\bar{b}|\bar{B},\bar{\sigma}) p(\bar{c}|\bar{B}) p(\bar{B}) \end{aligned} \tag{6.4}$$

where the integral is done using a Monte-Carlo simulation (MC); the $p(\bar{b}|\bar{B},\bar{\sigma})$ is the product the likelihood function 6.2 of all the measured quantities, the probability $p(\bar{c}|\bar{B})$ is given by the model which is used (the Modified Rutherford equation in this case) and $P(\bar{B})$ gives the constraints characterising the quantities $\bar{B}$. This last term treats the complex dependencies among the various quantities, it accounts for the physical constraints on each of them (positivity, thresholds, etc...) and for the automatic propagation of errors for each quantity B_{N+1} which depends on the quantity B_N:

$$P(B_1|B_2,....) * P(B_2|B_3.....) * P(B_N) \tag{6.5}$$

In this way, the posterior probability distributions for c_{sat} and c_{stab} is first calculated by applying the marginalisation theorem over each single discharge and in a second phase it is calculated over all the discharges to get a unique value for c_{sat} and c_{stab} for the database. In this way, the probabilistic approach for the Modified Rutherford equation consists of the following steps:

1. sample random values for $\bar{B}$ from probability distributions $p(d|\bar{B},\bar{\sigma}) \cdot p(\bar{B})$ for individual discharges starting from the collected data $\bar{b}$
2. calculate the marginal posterior probability distribution $p(c_{\mathrm{sat}}, c_{\mathrm{stab}}|\bar{d},\bar{\sigma})$ for each single discharge
3. carry out a sensitivity study on the quantities $\bar{B}$ present in the Modified Rutherford equation
4. calculate the marginal posterior probability distribution $p(c_{\mathrm{sat}}, c_{\mathrm{stab}}|\bar{d},\bar{\sigma})$ considering all the discharges simultaneously
5. calculate $< c_{\mathrm{sat}} >$, $< c_{\mathrm{stab}} >$ and $\Delta_{c_{\mathrm{sat}}}$, $\Delta_{c_{\mathrm{stab}}}$ [1] for each single discharge as well as for all discharges together

As explained in chapter 5, the technique adopted to evaluate c_{sat} and c_{stab} has been to measure the necessary quantities $\bar{B}$ present in equation 2.49 at two specific time points t_{sat} and t_{ECCD}. In order to build a numerical tool able to treat the Modified Rutherford equation in a statistical way, the time points needed for the analysis of equation 2.49 are labelled with $i = 1,2$ and the following quantities are defined:

$$\xi_{0i} = r_{\mathrm{res}}\Delta' - \frac{\tau_s}{r_{\mathrm{res}}}\left(\frac{dW}{dt}\right)|_{t_i} \tag{6.6}$$

$$\xi_{1i} = r_{\mathrm{res}}(\Delta'_{\mathrm{BS}} + \Delta'_{\mathrm{GGJ}}) \tag{6.7}$$

$$\xi_{2i} = r_{\mathrm{res}}\Delta'_{\mathrm{ECCD}} \tag{6.8}$$

where ξ_{2i} can be calculated only in case $i = 2 \rightarrow t = t_{\mathrm{ECCD}}$ as it only accounts for the Δ'_{ECCD} term and $\frac{dW}{dt} = 0$ at $t = t_{\mathrm{sat}}$ and $\frac{dW}{dt} \leq 0$ at $t = t_{\mathrm{ECCD}}$. Therefore, the fitting of c_{sat} and c_{stab} can be numerically expressed by re-writing equation 2.49 in the form:

$$0 = \xi_{0i} + c_{\mathrm{sat}}\xi_{1i} + c_{\mathrm{stab}}\xi_{2i} + \epsilon \tag{6.9}$$

where ϵ is the deviance from $\frac{\tau_s}{r_{\mathrm{res}}}\frac{dW}{dt} = 0$ and $< \epsilon >= 0$, $< \epsilon^2 >= \sigma^2$ where σ^2 is its variance. It is assumed to be $\sigma = 0.01$ for all the discharges which represents roughly 10% of uncertainty in the evaluation of $\frac{dW}{dt}$. By assuming a normally

[1] $\Delta_{c_{\mathrm{sat}}} = \sqrt{< c_{\mathrm{sat}}^2 > - < c_{\mathrm{sat}} >^2}$, $\Delta_{c_{\mathrm{stab}}} = \sqrt{< c_{\mathrm{stab}}^2 > - < c_{\mathrm{stab}} >^2}$

distributed error, the fitting of c_{sat} and c_{stab} corresponds to the minimisation of χ^2 defined as:

$$\frac{1}{2}\chi^2 = \frac{1}{2}\sum_{i=1,2}\left(\frac{\xi_{0i} + c_{sat}\xi_{1i} + c_{stab}\xi_{2i}}{\sigma_i}\right)^2 \tag{6.10}$$

In order to minimise the χ^2, the derivative with respect to c_{sat} and c_{stab} has to be 0, that is:

$$\frac{\partial\frac{1}{2}\chi^2}{\partial c_{sat}} = \sum_i \frac{1}{\sigma_i^2}(c_{sat}\xi_{1i} + c_{stab}\xi_{2i} + \xi_{0i})\xi_{1i} = 0 \tag{6.11}$$

$$\frac{\partial\frac{1}{2}\chi^2}{\partial c_{stab}} = \sum_i \frac{1}{\sigma_i^2}(c_{sat}\xi_{1i} + c_{stab}\xi_{2i} + \xi_{0i})\xi_{2i} = 0 \tag{6.12}$$

$$\tag{6.13}$$

By defining the following quantities:

$$\begin{aligned} &\beta_{11} = \sum_i \frac{\xi_{1i}^2}{\sigma_i^2}, \quad \beta_{02} = \textstyle\sum_i \frac{\xi_{0i}\xi_{2i}}{\sigma_i^2}, \quad \beta_{12} = \sum_i \frac{\xi_{1i}\xi_{2i}}{\sigma_i^2} \\ &\beta_{22} = \sum_i \frac{\xi_{2i}^2}{\sigma_i^2}, \quad \beta_{01} = \textstyle\sum_i \frac{\xi_{0i}\xi_{1i}}{\sigma_i^2} \end{aligned} \tag{6.14}$$

the system of equations to be solved simultaneously in order to determine c_{sat} and c_{stab} is:

$$c_{sat}\beta_{11} + c_{stab}\beta_{12} = \beta_{01} \tag{6.15}$$

$$c_{sat}\beta_{12} + c_{stab}\beta_{22} = \beta_{02} \tag{6.16}$$

which leads to the solutions

$$c_{sat} = \frac{\beta_{01}\beta_{22} - \beta_{02}\beta_{12}}{\beta_{11}\beta_{22} - \beta_{12}^2} \tag{6.17}$$

$$c_{stab} = \frac{\beta_{02}\beta_{11} - \beta_{01}\beta_{12}}{\beta_{11}\beta_{22} - \beta_{12}^2} \tag{6.18}$$

In case no ECCD is applied (that is $\xi_{2i} = 0$), c_{sat} can be determined simply as $c_{sat} = \frac{\beta_{01}}{\beta_{11}}$.

6.2.1 Randomisation of the measured quantities, physics boundaries,standard deviations

The quantities present in equation 2.49 which have been treated as a source of uncertainty in the statistical analysis are the following: W_{sat}, W_{ECCD}, T_e , T_i, n_e, L_{ne},

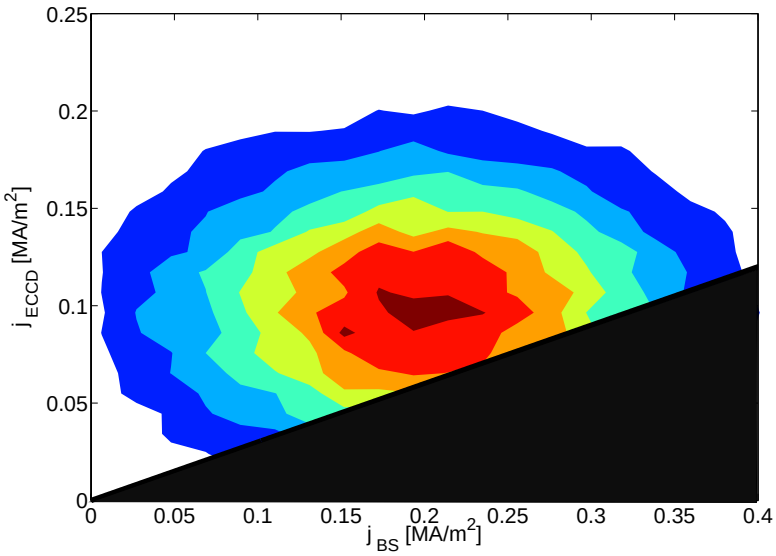

Figure 6.1: One of the physics boundary imposed in the error analysis calculation is that the randomisation of j_{ECCD} and j_{BS} would satisfy the condition $\frac{j_{\mathrm{ECCD}}}{j_{\mathrm{BS}}} > 0.3$ for which in the present database is the marginal value which still allows for stabilisation.

L_{Te}, L_q, j_{BS}, j_{ECCD}, d, η_{ECCD} and dW/dt at t_{ECCD}. The uncertainty on the quantities B_{pol}, B_T, ϵ_s,r_{res} have been neglected because they are negligible compared to the role played by the uncertainty on the quantities listed above. On the other hand, in case of other quantities such as the radial misalignment x_{mis}, which highly affects the resulting c_{stab}, the uncertainties are indirectly and more straightforwardly accounted by considering the uncertainties on η_{ECCD} and $dW/dt|_{\mathrm{ECCD}}$. The effect of the statistical uncertainty of these quantities, however, is small since, as mentioned in chapter 5, the technique to determine c_{stab} has been to choose it in such a way that the simulated $W(t)$ evolution would overlap at its best the experimental one and this method constraints quite strongly the shape of the decaying curve $\frac{dW}{dt}|t_{\mathrm{ECCD}}$. In order to analytically recover c_{stab} from equation 6.18, W_{ECCD} is considered which is the maximum value of the curve $dW/dt|t_{\mathrm{ECCD}}$ used to start the simulation but is not necessarily the same as the marginal island after which the mode naturally decays $W_{\mathrm{marg,ECCD}}$.
Considering the 23 discharges taken into account, the 2 time points necessary for the analysis and the 13 quantities which are considered within their uncertainty, the number of uncertain model parameters in equation 2.49 is $\approx N_{\mathrm{discharges}} * 2 * 13 \approx 600$. In the following statistical analysis each quantity has been randomised 50000 times, which is large enough to get the marginal probability distribution smooth. A randomisation of 10000 times has been tested to be the lower limit for the creation of smooth enough probability distributions. The physics boundaries imposed on the randomisation of the involved plasma quantities are that all the

quantities defined positive should stay positive (or those defined negative as in the case of L_{Te} or L_{ne} or $dW/dt|_{ECCD}$ should stay negative), the deposition width d has to have a minimum value of 2 cm, the minimum ratio j_{ECCD}/j_{BS} for stabilisation is ~ 0.3 (as shown in figure 6.1) and that W_{sat} has to be larger than the seed island size W_d or W_b. One of the main issues is to give a proper estimate for the standard deviations; in general for the quantities measured directly from a diagnostic the value given from the diagnostician is considered as the standard deviation, as for example in the case of the kinetic profiles (for which $\sigma \leq 7\%$ for T_i and T_e and $\sigma \sim 10\%$ for n_e both at ASDEX Upgrade and JT-60U have been assumed). On the other hand, for the quantities which are an output of codes (such as j_{BS} or j_{ECCD}) or are calculated by doing derivatives (as the gradients L_q, L_{ne} or L_{Te}) establishing what is the proper standard deviation is more complicated since one should take into account the approximations in the model on which it is based on, the numerical precision of the calculation etc. In this work, a value of the standard deviations is considered which is a good compromise between being too optimistic and getting very small error bars (smaller than $5-10\%$ uncertainty) on the randomised quantities and being too pessimistic and getting very large error bars (larger than $50-60\%$ uncertainty). The differences between discharges have not been accounted as in principle they have all been treated in the same way, with the same measurements conditions. The values for the standard deviations assumed for the statistical analysis are listed in table 6.1.

Table 6.1: Standard deviations σ given in percentage assumed for the statistical analysis

L_{ne}	W_{sat}, L_q, j_{BS}	j_{ECCD}, d ,n_e, L_{Te}, η_{ECCD}, $\frac{dW}{dt}\|_{t_{ECCD}}$	T_e, T_i	W_{ECCD}
20%	15%	10%	7%	5%

6.3 Results of the error analysis

Given these standard deviations, the plots related to the determination of c_{sat} and c_{stab} discussed in chapter 5 are shown in figure 6.2 and figure 6.3. The uncertainties calculated for c_{sat} and c_{stab} are in the order of 30%; in particular, for the evaluation of σ in the case of c_{stab}, it has to be taken into account that the statistical uncertainty in the value of the misalignment is accounted in $dW/dt|_{t_{\mathrm{ECCD}}}$,$\eta_{\mathrm{ECCD}}$ and W_{ECCD}.

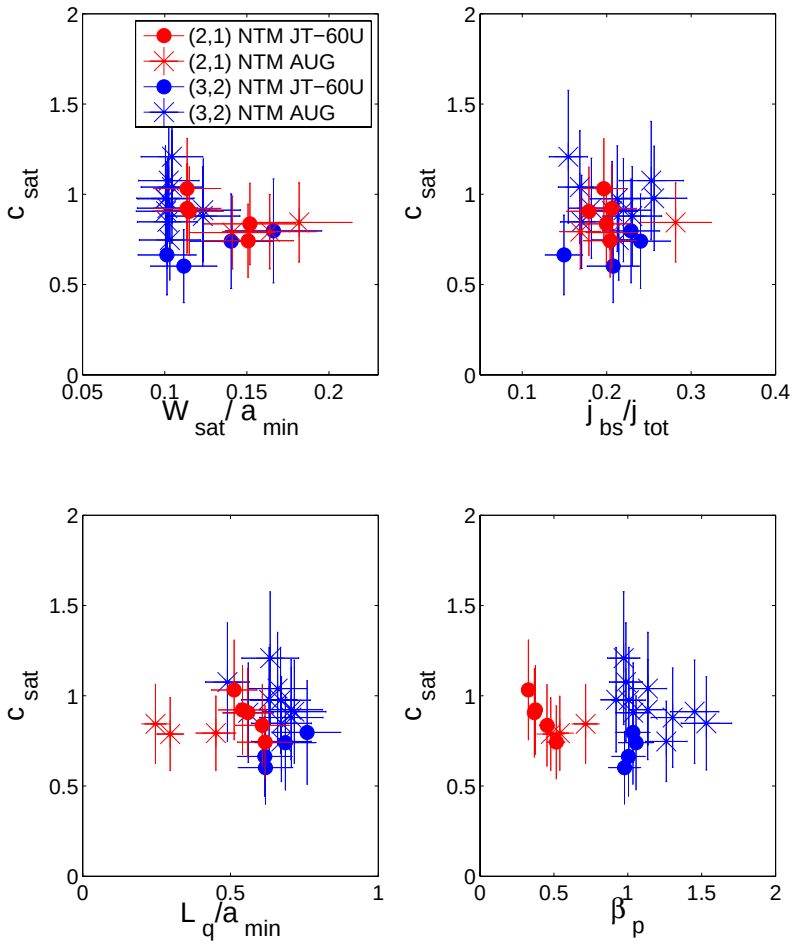

Figure 6.2: Determination of the fitting coefficient c_{sat} for the database collected accounting for the standard deviations in W_{sat}, j_{BS}, L_q and β_p: the error bar on c_{sat} is obtained for every discharge by randomisation of each quantity present in the Modified Rutherford equation over a given range of uncertainty. The value of c_{sat} is given with a standard deviation $\sigma_{c_{\mathrm{sat}}} = 30\%$ considering an uncertainty for W_{sat}, for L_q and j_{BS} and β_p of 15%.

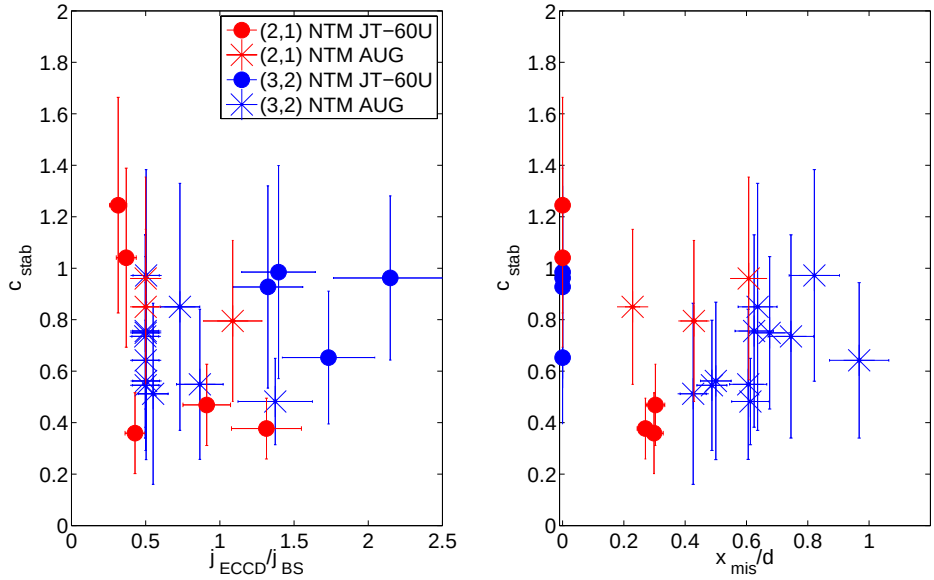

Figure 6.3: Determination of the fitting coefficient c_{stab} for the database collected accounting for the standard deviations in j_{ECCD}, j_{BS}, d: the error bar on c_{stab} is obtained for each discharge by randomising every quantity present in the Modified Rutherford equation over a given range of uncertainty. The value of c_{stab} is given with a standard deviation $\sigma_{c_{stab}} = 30\% \div 40\%$ considering that the uncertainty for j_{ECCD} and for d is $\sim 10\%$, for j_{BS} is 15%.

6.3.1 Sensitivity analysis

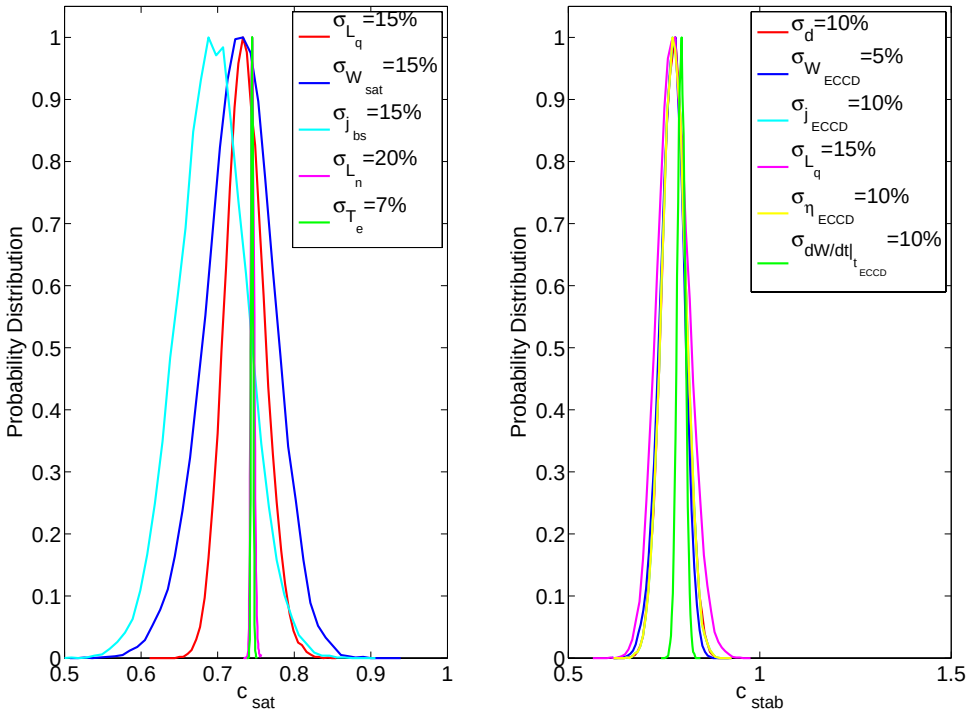

Figure 6.4: Effect on the probability distribution for c_{sat} and c_{stab} of each quantity present in the Modified Rutherford equation which is randomised within its realistic statistical uncertainty. The largest influence on c_{sat} is given by W_{sat}, j_{BS} and L_q whereas the uncertainty of L_{ne}, which is quite large, has almost no effect since it enters explicitly in the Modified Rutherford equation only in the small island physics term Δ'_{GGJ}. As far as c_{stab} is concerned, all the quantities have a similar influence on its value except $dW/dt|_{t_{\mathrm{ECCD}}}$ which is less affecting the width of the probability distribution function.

As mentioned in the section before, not all the quantities present in the Modified Rutherford equation have been randomised over their uncertainty since their uncertainty does not affect the evaluation of c_{sat} and c_{stab}. Nevertheless, for the other quantities considered in the statistical analysis it is convenient to study which quantity has the most effect when doing the analysis. In order to carry out such a sensitivity study only one relevant quantity at a time is considered by switching off the other quantities' uncertainties. Statistically, this means to marginalise the probability distribution over one of the crucial quantities given that the other quantities have no uncertainty, as for example L_q:

$$p(c_{\mathrm{sat}}, c_{\mathrm{stab}}|\bar{d}) = \int d\,Lq p(c_{\mathrm{sat}}, c_{\mathrm{stab}}, L_q|\bar{d}) \tag{6.19}$$

The results of the sensitivity test are shown in figure 6.4 where each quantity is randomised over the realistic the uncertainties listed in table 6.1, W_{sat} and j_{BS} and L_q are found to be the most crucial ones, whereas for c_{stab} all the quantities affect the evaluation in a similar way but the quantity $dW/dt|t_{ECCD}$ which is less influencing the width of the probability distribution with the given σ. Additionally, it is interesting to notice, that some quantities like j_{BS} and W_{ECCD} tend to shift the center of the probability distribution towards the left as their uncertainty is increased and this is due to the non-linear dependence of c_{sat} and c_{stab} on these quantities.

6.3.2 Posterior probability distribution (PDF) and consistency of the data

The results obtained for the marginalised posterior probability distributions for c_{sat} and c_{stab} over a single discharge and over all the discharges are shown in figure 6.5 and 6.6 respectively. The results show that:

- the PDF obtained for each single discharge is centred around a value which agrees with the one calculated from the measured quantities
- the PDF obtained by marginalising over all the discharges is centred around a value which is slightly different ($c_{sat} = 0.64$ and $c_{stab} = 0.62$) than the mean value found from the single discharge calculation ($c_{sat} = 0.74$ and $c_{stab} = 0.54$)
- this difference increases if the standard deviations assumed in the randomisation process also increase whereas if they are kept small, the overall PDF accounting for the randomisation of all the discharges agrees with the simple mean value obtained in chapter 5; this suggests hat the non-linearity of the Modified Rutherford equation plays an important role in the statistical approach for establishing the error and also that for some quantities a skewed probability distribution should better represent the distribution of its values compared to the normal distribution which has been assumed here.
- the standard deviation σ of the PDF for c_{sat} and c_{stab} obtained marginalising over all the discharges becomes smaller ($\sigma = 10\% \div 15\%$) compared to the marginalisation over every single discharge ($\sigma = 30\% \div 40\%$)
- for both the PDF over a single discharge and over all the discharges there is a clear correlation between c_{sat} and c_{stab}

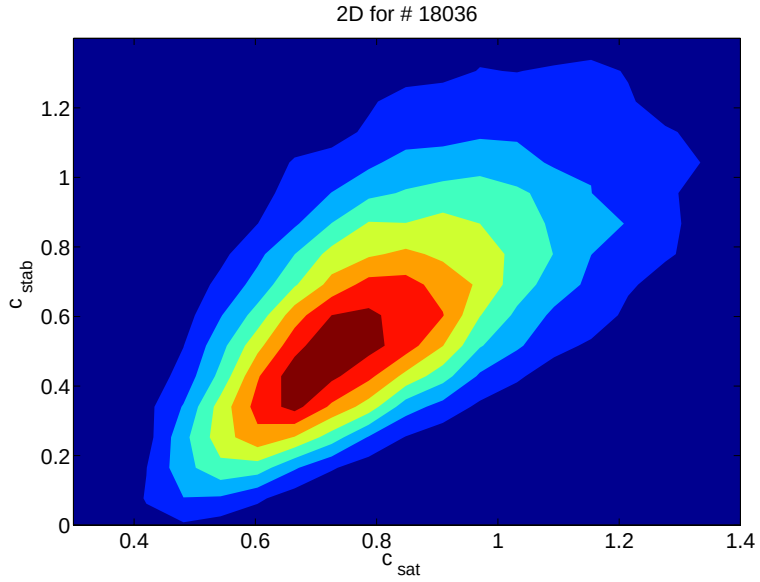

Figure 6.5: 2D marginal posterior probability distribution for one discharge; the resulting probability distribution is centered around the mean value and has an asymmetrical shape indicating correlation between c_{sat} and c_{stab}

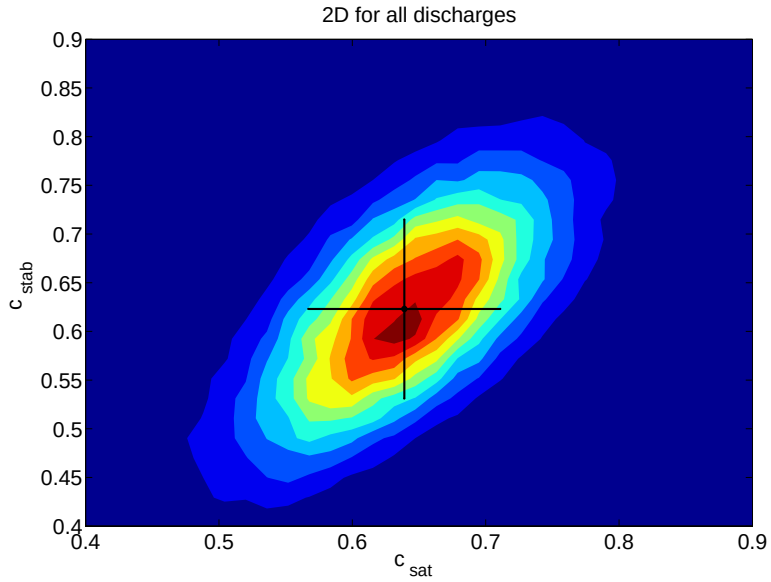

Figure 6.6: 2D marginal posterior probability distribution for c_{sat} and c_{stab} obtained by marginalising over all discharges to get a unique probability distribution for the fitting coefficients considering the whole database. The PDF over all the discharges is asymmetrical indicating clear correlation between c_{sat} and c_{stab}; secondly, although the valus of the fitting parameters are consistent with the marginalised probability over a single discharge, the PDF marginalised over all the discharges has a mean value for c_{sat} and c_{stab} which is slightly different than the simple arithmetic mean.

Chapter 7

Predictions for ITER

This final chapter deals with the predictions that can be made for ITER in terms of power requirements for NTM stabilisation considering the results presented in chapter 5 for the fitting coefficients of the Modified Rutherford equation 2.49. In the first part of the chapter the relevance of NTMs and the ITER scenario in which NTMs are foreseen as being demaging is described and the physics assumptions for using the Modified Rutherford equation are clarified. Then, ITER predictions for the amount of ECRH power necessary for stabilising NTMs are presented both for (3,2) NTMs and (2,1) NTMs in case of continuous current injection, 50% modulated injection considering first a symmetric island and then asymmetric one.

7.1 NTMs in ITER

In considering simulations studies, the main difference between present-day devices and ITER comes from the fact that ITER simulations cannot be constrained by experimental measurements. Predictive models have to be used instead, which implies that an essential step is the experimental validation of those models against tokamak discharges as close as possible to those expected in ITER. Predictions for several features are fairly accurate and well established (heat source, neoclassical terms, ...). Conversely, models for the heat transport, density profile shape are still questionable and their validation is the subject of an intense scientific debate. At the present state, all ITER scenarios are based on the H-mode, which implies transport models for both the pedestal and the core plasma. In particular, the so-called reference scenario 2 is often used. This plasma scenario is characterised by an H-mode plasma with an inductive current $I = 15$ MA with a full bore plasma producing 400 MW of fusion power with $Q = 10$ for about 400 s. The performance of ITER with this plasma scenario is predicted using the transport code ASTRA [Polevoi and Gribov(2002)] which has been already used

in this work for calculating the transport quantities such as j_{BS} and η_{NC} at ASDEX Upgrade. The free boundary plasma equilibrium for ITER is calculated with PRETOR code [Boucher(1992)] using the same current profile as the one used in the ASTRA simulation. NTMs physics is expected to scale with the normalised local ion poloidal gyroradius [Günter(1998)]

$$\rho_{\mathrm{pi}}* = \frac{\rho_{\mathrm{pi}}}{a} = \frac{v_{\mathrm{th}} / \omega_{\mathrm{ci}}}{a} = \frac{\sqrt{2 m_i k T_i(r_{\mathrm{res}})} / eB_{\mathrm{pol}}(r_{\mathrm{res}})}{a} \tag{7.1}$$

and since the $\rho_{\mathrm{pi}_{\mathrm{ITER}}} \sim 0.1 - 0.2 \rho_{\mathrm{pi}_{\mathrm{AUG}}}$, ITER baseline operation scenario lies deeply into a metastable region in which NTMs can easily be excited. However, the mode growth will be slow as the resistive time in ITER has a typical value $\tau_s \approx 70$ s and therefore the detection of magnetic island that form during the discharge is expected to be addressable and stabilisation schemes are being prepared for this purpose. In the plasma scenario 2 the other global parameters which are used in the simulations are the toroidal magnetic field $B_T = 5.3$ T, $\beta_N = 1.9$, $q_{95} = 3.1$ and $Z_{\mathrm{eff}} = 1.7$ (which is assumed to be a flat profile all over the plasma radius). The position of the (3,2) NTM and (2,1) NTM are taken from the equilibrium calculation and indicate that the (3,2) NTM is located at $\rho_p = 0.77$ and the (2,1) NTM is located at $\rho_p = 0.87$. Therefore, the mode positions are located more outside compared to the values in JT60U and ASDEX Upgrade. The local values which are needed in the Modified Rutherford equation 2.49 are calculated by interpolating the output profiles built with ASTRA at the mode position. The neoclassical resistivity profile is calculated using the σ from ASTRA and $\eta_{\mathrm{NC}} \approx (j_{\mathrm{Ohm}} / 2\pi R_{\mathrm{maj}} U)^{-1}$ where U is voltage related to the ohmic current j_{Ohm}. The local flux-averaged poloidal magnetic field is $B_{\mathrm{pol}} = 0.97$ T for (2,1) case and $B_{\mathrm{pol}} = 1.07$ T for the (3,2) case.

NTM	ρ_p	T_e [keV]	T_i [keV]	n_e [10^{20} m^{-3}]	β_p	r_{res} [m]	η_{NC} [10^{-8} Ωm]	ϵ_s	L_p [m]	L_q [m]	j_{BS} [MA / m^2]
(3,2)	0.77	7.6	7.4	1.0	1.4	1.3	2.1	0.2	-1.0	0.88	0.09
(2,1)	0.87	5.6	5.7	0.98	1.0	1.55	3.4	0.25	-0.9	0.87	0.07

Table 7.1: Local plasma parameters in ITER in case of (3,2) and (2,1) NTM

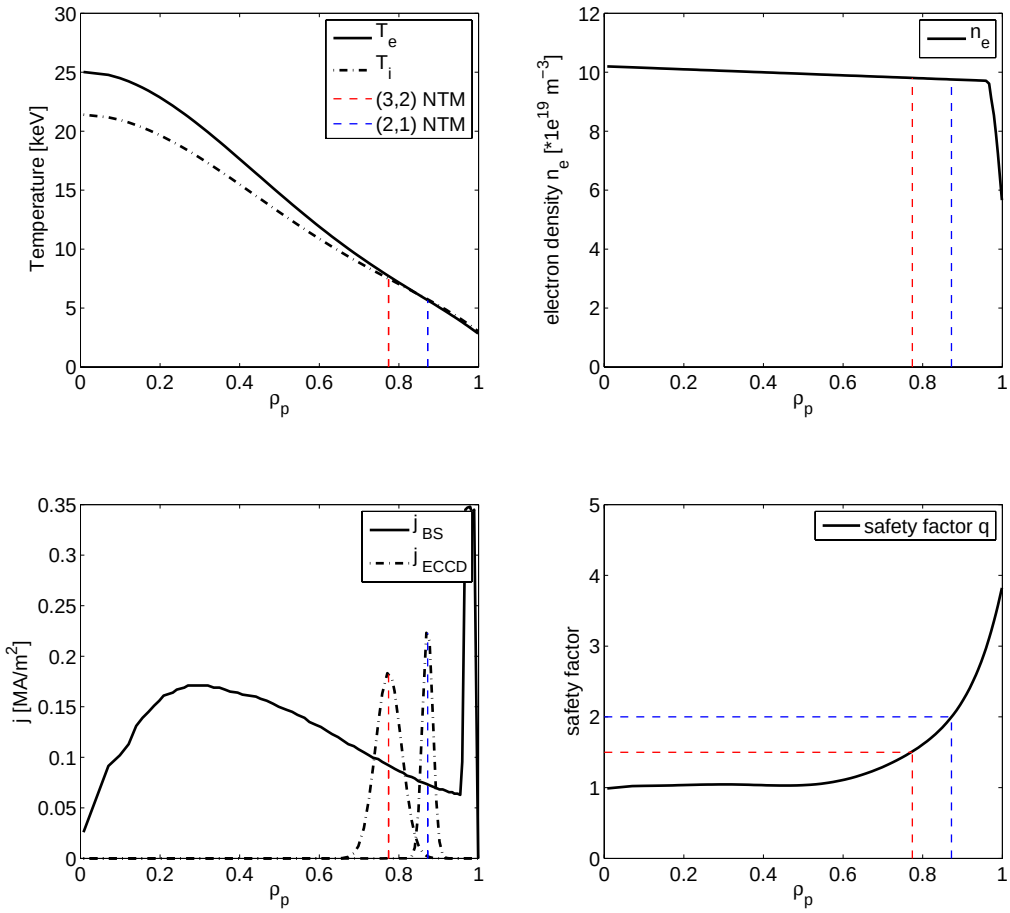

Figure 7.1: Profiles of (a) electron and ion temperatures, (b) plasma electron density, (c) bootstrap current density and ECCD current density and (d) safety factor q. The red and blue dotted lines indicates the position of the (3,2) and (2,1) NTM determined from the position of the $q = 1.5$ and $q = 2$ respectively. The profiles obtained from ASTRA describe what is expected for ITER plasma scenario 2, which is the most likely to be highly affected by the presence of NTM.

7.2 NTM stabilisation in ITER

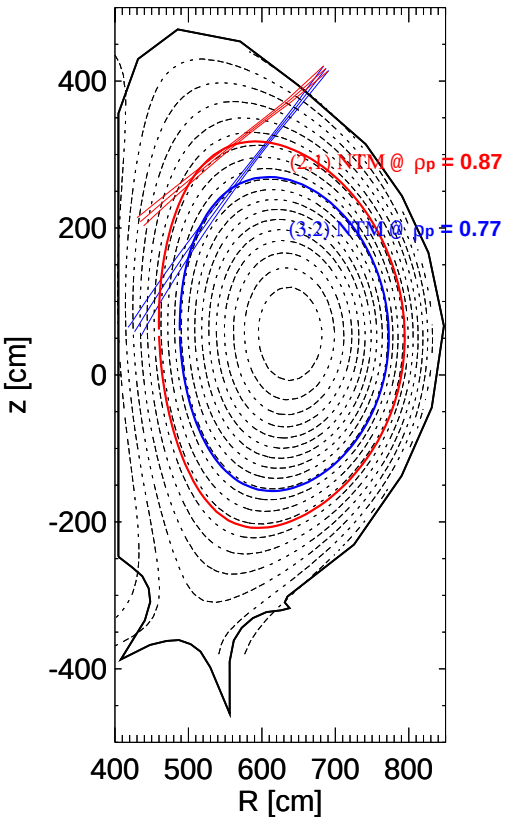

Figure 7.2: Poloidal cross-section of ITER: in color are highlighted the positions of the (2,1) and (3,2) NTM (red and blue respectively) and the ECCD injection beams corresponding to the angles used in TORBEAM for the determination of j_{ECCD} and d.

The ECRH system which is foreseen for ITER makes use of the front steering system from the upper port launcher antenna from which a nominal amount of $P_{ECRH} = 20MW$ will be injected in O-mode with 170 GHz frequency using 24 gyrotrons which will deliver 1-2 MW each [Henderson(2007)]. The amount of ECRH power necessary is still very much under debate as possibly other 20 MW of extra P_{ECRH} are accounted to be added. However, priority in the stabilisation scheme is given to control the (2,1) NTM as this is predicted to be the most damaging NTM. Therefore, the optimisation of the ECCD injection in terms of injected current density j_{ECCD} and deposition width d has been done aiming at injecting the highest possible amount of j_{ECCD} at the resonant surface of the (2,1) NTM with a small deposition width d. The determination of j_{ECCD} and d is carried out using the Torbeam code and the results are shown in figure 7.3. The Torbeam runs were done using the settings foreseen for ITER which optimise the injection from the upper launcher with front steering system: the toroidal angle β is fixed at 20° whereas the poloidal angle α is fixed to 53° and 43° for hitting the resonant surface of the (3,2) and (2,1) NTM respectively as shown in figure 7.3. The toroidal angle β has been fixed to such a value which allows for the maximum injection of current density (such that $j_{ECCD} > 1.2 j_{BS}$) whereas the poloidal angle α is chosen to be able to inject the current at the mode position. Under these assumptions, the (2,1) NTM stabilisation is characterised by a deposition width of about 2.5 cm and the (3,2) NTM stabilisation by a width of about 3.8 cm in

agreement with the values given by [Ramponi(2008)](Table 2) with a ratio

$$\frac{j_{\mathrm{ECCD}}}{P_{\mathrm{ECRH}}} = \frac{14819\ A/m^2}{MW} \text{ for the (2,1) NTM} \tag{7.2}$$

$$\frac{j_{\mathrm{ECCD}}}{P_{\mathrm{ECRH}}} = \frac{12721\ A/m^2}{MW} \text{ for the (3,2) NTM} \tag{7.3}$$

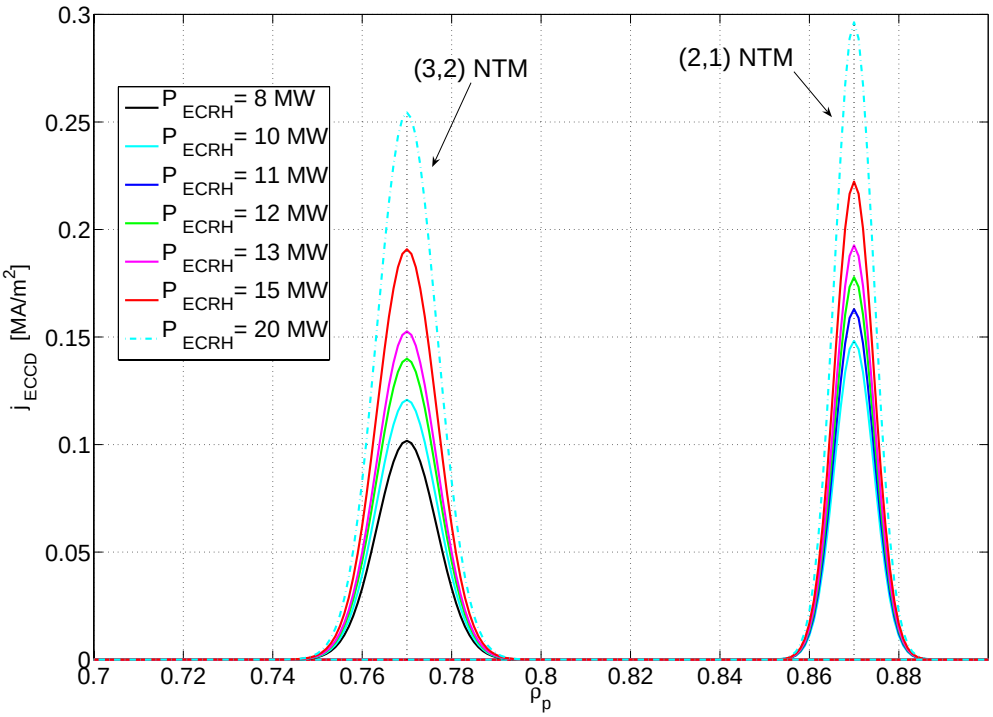

Figure 7.3: Results for Torbeam runs for determining the j_{ECCD} and d given the optimised angles $\beta = 20^\circ$ and $\alpha = 43^\circ$ (for the (2,1) NTM resonant surface) or $\alpha = 53^\circ$ (for the (3,2) NTM resonant surface). As the angles are fixed the deposition width does not change and is $d \approx 0.038$ m for the (3,2) NTM case and $d = 0.025$ m for the (2,1) NTM, for which the ECCD injection has been optimised. The peak of the j_{ECCD} changes by and amount $\frac{j_{\mathrm{ECCD}}}{P_{\mathrm{ECRH}}} = \frac{14819\ A/m^2}{MW}$ for the (2,1) NTM and $\frac{j_{\mathrm{ECCD}}}{P_{\mathrm{ECRH}}} = \frac{12271\ A/m^2}{MW}$ for the (3,2) NTM.

7.3 The Modified Rutherford equation and ITER

To study the amount of ECRH power which is necessary to use in order to stabilise NTMs in ITER, different cases of stabilisation scenarios are analysed and simulated using the Modified Rutherford equation 2.49 with $c_{\mathrm{sat}} = 0.81$ and

$c_{\mathrm{stab}} = 0.68$. Both the cases of a symmetrical island and an asymmetrical one with $\gamma = 0.5$ are considered as one expects that the most realistic case will lie in between these two cases. These different cases are first run for continuous injection and successively for modulated injection (50%). In the simulations the misalignment is kept fixed during the discharge (similarly to JT-60U) given the design of the ECRH system which is planned for ITER. Since the stabilising effect of the simple heating due to ECRH and of j_{ECCD} on the equilibrium current profile via changing Δ' is not incorporated, what is obtained in this work are the upper limits for the power required for stabilisation.

7.3.1 Determination of the saturated island size W_{sat}

First, in order to calculate the power requirements for ITER, the saturated island width W_{sat} for (3,2) and (2,1) needs to be evaluated by inserting the value of c_{sat} resulting from the multi-machine benchmark of chapter 5. In fact, considering equation 2.50 this can be evaluated as:

$$W_{\mathrm{sat}} = c_{\mathrm{sat}} 6.34 f_{\mathrm{GGJ}} \frac{\mu_0 L_q j_{\mathrm{BS}}}{B_{\mathrm{pol}}(-\Delta')} \tag{7.4}$$

where Δ' is set to $\Delta' = -\frac{m}{r_{\mathrm{res}}}$. The results obtained using the global and local

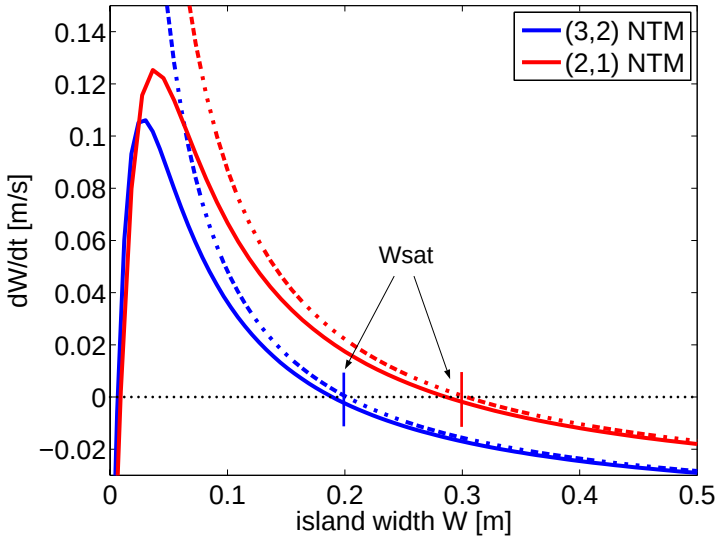

Figure 7.4: Phase diagram for ITER saturated phase characterising the saturation (no ECCD) obtained by assuming c_{sat} from benchmark between JT-60U and ASDEX Upgrade and by neglecting the small island physics terms. By using the mean value $c_{\mathrm{sat}} = 0.81$ obtained in chapter 5, the (3,2) NTM has a saturated island size of $W_{\mathrm{sat}} \approx 0.2$ m whereas the (2,1) NTM is found to have $W_{\mathrm{sat}} \approx 0.3$ m. This corresponds to $0.1a$ and $0.15a$ respectively.

plasma parameters listed above are $W_{\mathrm{sat},32} \approx 0.2\,m$ and $W_{\mathrm{sat},21} \approx 0.3\,m$. The island size which are obtained are quiet large especially in case of (2,1) NTM; nevertheless these values have to be considered as upper limits of the real saturated island width as they are calculated neglecting the stabilising small island width effects such as W_b and W_d which lower of few centimetres the resulting saturated island width as figure 7.4 shows. This large island size ($\sim 0.15a$) suggests that in ITER the (2,1) NTM will easily lock to the wall. However, this will not be always the case since, as already seen in ASDEX Upgrade, (2,1) NTMs may also initially lock but spin up during the stabilisation when the maximum power is applied.

7.3.2 Stabilisation of (2,1) and (3,2) NTM

The saturated island size obtained from the fit with the Modified Rutherford equation has quite a large value compared to the width of the ECCD deposition which is foreseen for the adopted ECRH stabilisation scheme. This indicates that in ITER the operational scenario for ECCD stabilisation of a saturated (3,2) or (2,1) NTM will be characterised by the conditions $W_{\mathrm{sat}} >> W_{\mathrm{marg}}$ and $W_{\mathrm{marg}} \sim d$ mainly implying that both modulation and continuous drive of ECCD will require a very good alignment scheme between ECCD and the O-point of the island. The simulation of the (3,2) and (2,1) NTM stabilisation is done assuming a realistic asymmetric shape of the magnetic island with $\gamma = 0.5$. The general observations that can be done considering the (2,1) NTM stabilisation (figure 7.5) and the (3,2) NTM stabilisation (figure 7.6) are mainly the following:

- the P_{ECRH} necessary to marginally stabilise a saturated (2,1) NTM is $P_{\mathrm{ECRH}} = 10$ MW and $P_{\mathrm{ECRH}} = 9$ MW for DC injection and AC injection respectively
- in the (2,1) NTM stabilisation the maximum allowable misalignment is $\frac{x_{\mathrm{mis}}}{d} = 0.5$ for the DC injection $\frac{x_{\mathrm{mis}}}{d} = 0.8$ in the AC injection case
- the P_{ECRH} necessary to marginally stabilise a saturated (3,2) NTM is $P_{\mathrm{ECRH}} = 10$ MW and $P_{\mathrm{ECRH}} = 7$ MW for DC injection and AC injection respectively
- in the (3,2) NTM stabilisation the maximum allowable misalignment when applying marginal P_{ECRH} is $\frac{x_{\mathrm{mis}}}{d} = 0.4$ in case of DC injection and $\frac{x_{\mathrm{mis}}}{d} = 0.6$ in case of AC injection;
- complete stabilisation occurs roughly in 30 s for both the stabilisation of (2,1) and (3,2) NTMs and given the smaller island size for the (3,2) NTM the stabilisation time will be shorter in this case

In light of these observations, the two important conclusions for the stabilisation for the (2,1) NTM and (3,2) NTM in ITER are that the available ECRH power is enough to cope with large NTMs and in particular with the (2,1) NTM as long as the misalignment is smaller than $x_{\mathrm{mis}}/d \leq 0.4 - 0.5$ in case of DC injection and $x_{\mathrm{mis}}/d \leq 0.6 - 0.8$ for AC injection and that clear benefit from modulation only occurs in the range $\frac{W}{d} < 1$. More power is necessary for stabilising the (2,1) NTM.

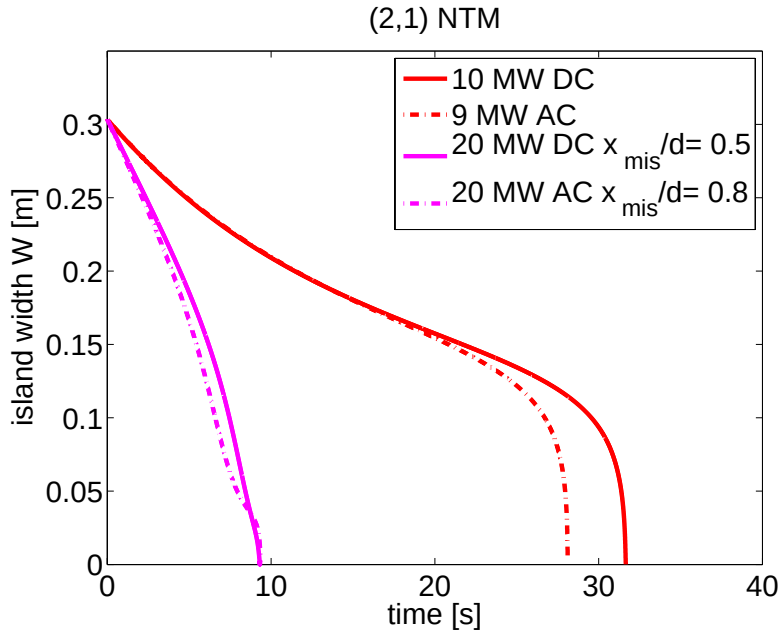

Figure 7.5: Simulation of NTM stabilisation in ITER for (2,1) NTM. In the DC case (full lines), $P_{\mathrm{ECRH}} = 10$ MW is the minimum required ECRH power to stabilise the mode for perfect alignment $x_{\mathrm{mis}}/d = 0$. In case of no perfect alignment, stabilisation is still possible with maximum amount of ECRH power $P_{\mathrm{ECRH}} = 20$ MW as long as $\frac{x_{\mathrm{mis}}}{d} \leq 0.5$. In the AC case (dash-dotted lines), $P_{\mathrm{ECRH}} = 9$ MW is the minimum required ECRH power to stabilise the mode for perfect alignment $x_{\mathrm{mis}}/d = 0$. In the AC case misalignment can reach $\frac{x_{\mathrm{mis}}}{d} = 0.8$ for a maximum amount of available ECRH power $P_{\mathrm{ECRH}} = 20$ MW.

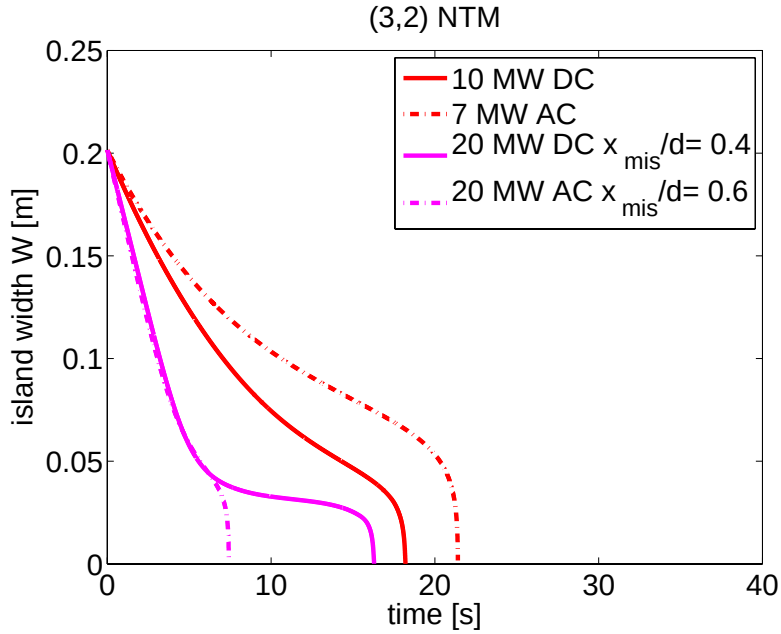

Figure 7.6: Simulation of NTM stabilisation in ITER for (3,2) NTM. In the DC case (full lines), $P_{\mathrm{ECRH}} = 10$ MW is the minimum required ECRH power to stabilise the mode for perfect alignment $x_{\mathrm{mis}}/d = 0$. In case of no perfect alignment, stabilisation is still possible with a maximum amount of ECRH power $P_{\mathrm{ECRH}} = 20$ MW as long as $\frac{x_{\mathrm{mis}}}{d} \leq 0.4$. In the AC case (dash-dotted lines), $P_{\mathrm{ECRH}} = 7$ MW is the minimum required ECRH power to stabilise the mode for perfect alignment $x_{\mathrm{mis}}/d = 0$. In the AC case misalignment can reach $\frac{x_{\mathrm{mis}}}{d} = 0.6$ and stabilisation is still possible for a maximum amount of ECRH power $P_{\mathrm{ECRH}} = 20$ MW.

7.4 Benchmark with other ECRH power requirements' predictions for ITER

It is interesting to compare the results presented in the above section with the previous works [LaHaye(2006)] and [Sauter(2006)] which have pointed out the marginal power requirements for NTM stabilisation in ITER. The different versions of the Modified Rutherford equation are the following:

$$A) \quad \frac{\tau_s}{r_{\rm res}}\frac{dW}{dt} = r_{\rm res}\Delta' + c_{sat}\left[r_{\rm res}\frac{6.34}{2}\mu_0 L_q \frac{j_{\rm BS}}{B_{\rm pol}}\left(\frac{W}{W^2+W_d^2}+\frac{W}{W^2+28W_b^2}\right) - \frac{r_{\rm res}6.35\mu_0 D_R}{\sqrt{W^2+0.65W_d^2}}\right] - c_{stab}16\sqrt{\pi}\mu_0 r_{\rm res}L_q\frac{j_{\rm ECCD}}{B_{\rm pol}}d\frac{\eta_{\rm ECCD}}{W^2}$$

$$B) \quad \frac{\tau_s}{r_{\rm res}}\frac{dW}{dt} = r_{\rm res}\Delta' + r_{\rm res}\Delta'(1-\Delta_\tau W)\left[\frac{W_{\rm sat,\infty}W}{W^2+W_{\rm marg}^2}\right] + c_j r_{\rm res}\Delta'(1-\Delta_\tau W)\frac{W_{\rm sat,\infty}}{d}\frac{j_{\rm ECCD}}{j_{\rm BS}}k_2$$

$$C) \quad \frac{\tau_s}{r_{\rm res}}\frac{dW}{dt} = r_{\rm res}\Delta' + a_2\frac{j_{\rm BS}}{j_\parallel}\frac{L_q}{W}\left[1-\frac{W_{\rm marg}^2}{3W^2}-k_1\frac{j_{\rm ECCD}}{j_{\rm BS}}\right] + r_{\rm res}\delta\Delta'$$

where equation A is the one which has been considered throughout this work, equation B is studied in ref.[Sauter(2006)] and equation C is studied in ref.[LaHaye(2006)].

7.4.1 (2,1) NTM stabilisation with equation B

In equation B, the destabilising term is written as

$$r_{\rm res}\Delta'_{\rm BS} = r_{\rm res}\Delta'(1-\Delta_\tau W)\left[\frac{W_{\rm sat,\infty}W}{W^2+W_{\rm marg}^2}\right] \tag{7.5}$$

$(r_{\rm res}\Delta')W_{\rm sat,\infty}$ is an other way of expressing the destabilising term $r_{\rm res}\Delta'_{\rm BS} = a_{\rm BS}c_{\rm BS}$ where $c_{\rm BS} = \frac{\mu_0 r_{\rm res}L_q j_{\rm BS}}{B_{\rm pol}}$ and $a_{\rm BS}$ is the numerical coefficient to account for the uncertainty in the model. The term $(1-\Delta'_\tau W)$ takes into account the drop of confinement due to the growth of the mode. This influences the value of the saturated island width $W_{\rm sat}$ compared to the β-dependent one $W_{\rm sat\infty} \approx \frac{a_{\rm BS}c_{\rm BS}}{-r_{\rm res}\Delta'}$ which, as already mentioned in chapter 2, is an upper value for $W_{\rm sat}$. In ref.[Sauter(2006)] the value for the fitting coefficient $a_{\rm BS}$ and $(1-\Delta_\tau W)$ are not directly specified; nevertheless the value for $W_{\rm sat\infty} = 32$ cm is given for the (2,1) NTM case and the value of the fitting coefficient can be recovered as $a_{\rm BS} = \frac{W_{\rm sat,\infty}}{c_{\rm BS}} \approx 3.4$. The reference considers a 25% of drop of confinement which translates into an effective island at saturation of width $W_{\rm sat} = 24$ cm. The threshold which allows for the island to develop is given by $\chi_\perp$ model and here the results using $W_d = 2$ cm are considered for the comparison In the $\Delta'_{\rm ECCD}$ term, the function k_2 is $k_2 = 4(\frac{d}{W})^2\eta_{\rm fs}$

where

$$\eta_{\rm fs} = \frac{6}{(\frac{W}{d})^4 + 40} + \frac{1}{(\frac{W}{d})^2 + 10} \tag{7.6}$$

is the efficiency function calculated in ref.[Sauter(2004)] which is shown in figure 7.7 together with $\eta_{\rm ECCD}$. This form of the efficiency function is calculated assuming a current profile within the island to be a helical flux function and results to be more stabilising than $\eta_{\rm ECCD}$. In the simulations carried out with equation B,

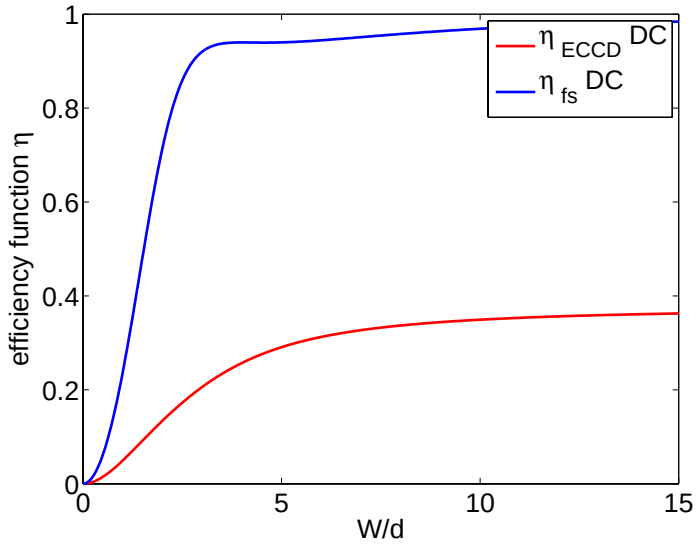

Figure 7.7: Efficiency functions used in model A, B and C: A and C consider a box-type current deposition profile resulting in $\eta_{\rm ECCD}$ whereas B considers the current profile within the island to be a helical flux function resulting in $\eta_{\rm fs}$.

the values for the ECCD injection are the ones outlined in section 7.2 and the coefficient $c_j = 0.5$ is introduced in order to account for over-stabilisation. In this way, the fitting coefficient which accounts for the uncertainty in the $\Delta'_{\rm ECCD}$ term reads $c_j a_{\rm BS}$ and it is halved in comparison with the coefficient present in the destabilising term $r_{\rm res}\Delta'_{\rm BS}$. The main result of ref.[Sauter(2006)] is that for a (2,1) NTM, given a perfect alignment ($x_{\rm mis} = 0$), a power $P_{\rm ECRH} \approx 13.3$ MW is necessary for marginal stabilisation either with CD or AC injection with $\frac{j_{\rm ECCD}}{j_{\rm BS}} = 2.8$.

7.4.2 NTM stabilisation with Equation C

Ref.[LaHaye(2006)] considers a unique fitting coefficient a_2 for the destabilising term and the stabilising one which is 2.8 and 3.2 for the (2,1) and (3,2) NTM respectively with the corresponding saturated islands of width $W_{\rm sat,21} = 25$ cm and $W_{\rm sat,32} = 12.5$ cm. The threshold for the island growth, in this case, is modelled via the polarisation term with a marginal island size given by $W_{\rm marg} = 1.4$ cm in the

case of the (2,1) NTM and $W_{marg} = 1.8$ cm in case of the (3,2) NTM. In equation C the quantities k_1 relates to the efficiency function η_{ECCD} as $k_1 = 4(\frac{d}{W})\eta_{ECCD}$ where η_{ECCD} is defined as in chapter 2. In the simulations done with equation C the values for the ECCD injection used consider a larger deposition width $d_{(2,1)} = 7.5$ cm and $d_{(3,2)} = 11.1$ cm with $j_{ECCD,(2,1)} = 5300\ [\frac{A/m^2}{MW}]$, $j_{ECCD,(3,2)} = 4800\ [\frac{A/m^2}{MW}]$. In addition equation C also accounts for the stabilising effect of ECCD due to the (0,0) component of the j_{ECCD} given in equation C by the term $r_{res}\delta\Delta'$. The main result obtained in ref.[LaHaye(2006)] is that for a (2,1) NTM, given a perfect alignment ($x_{mis} = 0$) cm, $P_{ECRH} \approx 12$ MW is necessary for marginal stabilisation with AC injection and $\frac{j_{ECCD}}{j_{BS}} = 0.9$ and in the (3,2) NTM case $P_{ECRH} \approx 15$ MW is necessary for marginal stabilisation with AC injection and $\frac{j_{ECCD}}{j_{BS}} = 0.75$. In addition, in ref.[LaHaye(2006)] AC injection is much more efficient than DC injection due to the larger values of the deposition width d which are used.

7.4.3 Comparison among ITER predictions of A, B and C

The predictions carried out for ITER using equation A, B and C indicate that the available ECRH power and the planned experimental set-up will be able to stabilise large saturated (2,1) and (3,2) NTMs. In fact, the results from equation A, B and C indicate that the value for minimum required P_{ECRH} will range between 10-13 MW for the (2,1) NTM case and continuous injection. In general, the three equations deal similarly with the major physics affecting the evolution of the magnetic island associated to the NTM; on the other hand, each of them takes into account other minor physics' effects which have a different impact on the results of the prediction for ITER. In figure 7.8 the phase diagrams obtained with the three different models and numerical factors for the ITER prediction in case of the (2,1) NTM stabilisation are shown. To discriminate among these different contributions, equation A, B and C can be written in a simplified form:

$$A1) \quad \frac{\tau_s}{r_{res}}\frac{dW}{dt} = r_{res}\Delta' + c_{sat}6.34 f_{GGJ}\frac{r_{res}\mu_0 L_q j_{BS}}{B_\theta}\frac{1}{W} - c_{stab}4\sqrt{\pi}\frac{4\mu_0 r_{res}L_q d j_{ECCD}}{B_\theta}\frac{\eta_{ECCD}}{W^2}$$

$$B1) \quad \frac{\tau_s}{r_{res}}\frac{dW}{dt} = -r_{res}\Delta' + a_{BS}(1-\Delta_\tau W)\frac{r_{res}\mu_0 L_q j_{BS}}{B_\theta}\frac{1}{W} - c_j a_{BS}(1-\Delta_\tau W)\frac{4\mu_0 r_{res}L_q d j_{ECCD}}{B_\theta}\frac{\eta_{fs}}{W^2}$$

$$C1) \quad \frac{\tau_s}{r_{res}}\frac{dW}{dt} = r_{res}\Delta' + a_2\frac{r_{res}\mu_0 L_q j_{BS}}{B_\theta}\frac{1}{W} - a_2\frac{4\mu_0 r_{res}L_q d j_{ECCD}}{B_\theta}\frac{\eta_{ECCD}}{W^2} + r_{res}\delta\Delta'$$

where the small island term is neglected leaving only the $\frac{1}{W}$-dependance in the destabilising term and $j_\parallel \approx \frac{B_{pol}}{\mu_0 r_{res}}$ and the curvature term in A is parametrized as f_{GGJ} (see chapter 2). The coefficients which affect the destabilising term are highlighted in red and these influencing the stabilisation term are highlighted in green. The term highlighted in magenta is only present in equation C. In this

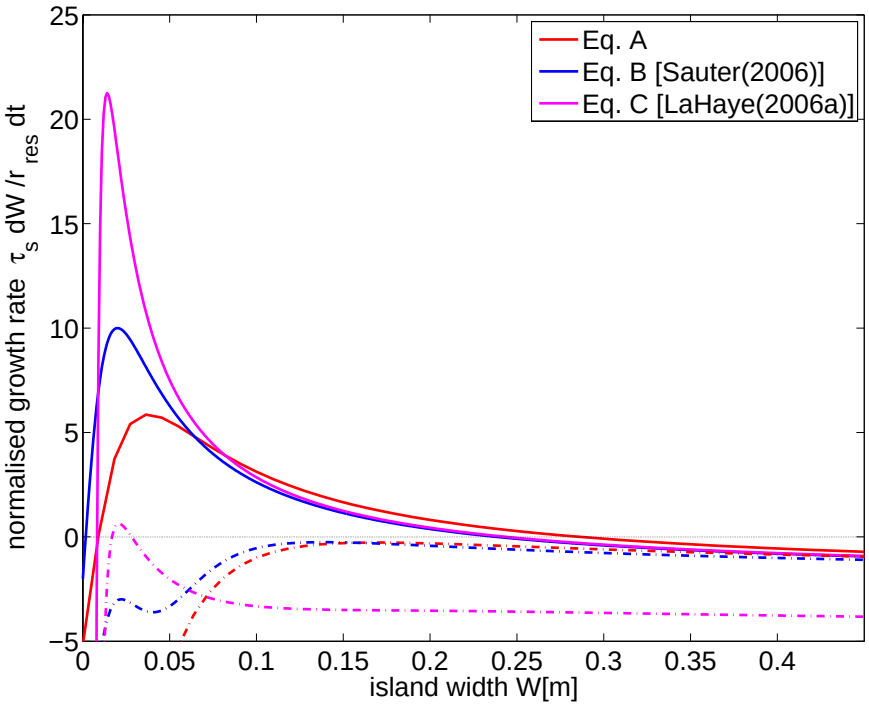

Figure 7.8: Phase diagram of (2,1) NTM stabilisation considering equation A, B, C: the saturated island size is $W_{\text{sat}} = 30$cm, $W_{\text{sat}} = 32$cm and $W_{\text{sat}} = 25$cm respectively. Equation B, however, takes into account the confinement degradation affecting W_{sat} and corrects it by a factor 0.75 leading to $W_{\text{sat}} = 24$ cm. Equation A has a smaller growth rate at saturation (full lines) because it accounts for additional stabilising terms such as the Δ_{GGJ} and the W_b effect as well as the $\chi_\perp$ term (W_d); on the other hand, equation C has the highest growth rate because it is characterised by the polarisation model. Marginal stabilisation (dash-dotted lines) is achieved with 10 MW DC injection, 13.6 MW DC injection and 12 MW AC injection in A, B and C with W_{marg} which varies depending on the threshold model being $\frac{W_{\text{sat}}}{W_{\text{marg}}} = 4-5$ for C and $\frac{W_{\text{sat}}}{W_{\text{marg}}} = 2-3$ for A and B.

way, the differences among the equations affecting the power requirements are isolated. In fact, in comparing the results one has to consider that:

- the amount of P_{ECRH} which is necessary to marginally stabilise the NTM depends on the ratio between the red term and the green one in every equation

- the difference in the value of the saturated island W_{sat} depends on the fitting coefficient at saturation of every equation

Table 7.2: Numerical coefficients which need to be inserted in equation A1, B1 and C1 in case of (2,1) NTM

A1	$c_{sat} = 0.81$	$f_{GGJ} = 0.9$	$c_{stab} = 0.68$
B1	$a_{BS} = 3.4$	$(1 - \Delta_\tau W) = 0.75$	$c_j = 0.5$
C1	$a_2 = 2.8$	-	$a_2 = 2.8$

The numerical coefficients which need to be inserted in equation A1, B1 and C1 are listed in table 7.2 and by substituting these values in the respective equations, the following correspondences apply in equation A1, B1 and C1 among the highlighted quantities:

$$\begin{array}{ccccc} A1 & & B1 & & C1 \\ c_{sat} 6.34 f_{GGJ} & \Leftrightarrow & a_{BS}(1 - \Delta_\tau W) & \Leftrightarrow & a_2 \\ 4.6 & \Leftrightarrow & 2.55 & \Leftrightarrow & 2.8 \\ c_{stab} 4\sqrt{\pi} & \Leftrightarrow & c_j a_{BS}(1 - \Delta_\tau W) & \Leftrightarrow & a_2 \\ 4.8 & \Leftrightarrow & 1.27 & \Leftrightarrow & 2.8 \end{array}$$

These correspondences are such that the ratio between the destabilising term (red) and the stabilising one (green) is 1 for equation A1 and C1 whereas it is 0.5 for equation B1. The difference by a factor 1.2 and 1.5 in the value of the fitting coefficient at saturation between A1 and B1 and A1 and C1 is reflected in the evaluation of the saturated island size. On the other hand, although the island size is larger for A, its coefficient at stabilisation (4.8) is as large as the one at saturation. In equation A the asymmetric nature of the island is also taken into account by using a factor $\gamma = 0.5$ in the efficiency function η_{ECCD} but this, as seen in chapter 5, does no have a deep impact on the power requirements. As already mentioned, equation B uses a form of the efficiency function η_{fs} which is much more stabilising than η_{ECCD} and which provides for an additional stabilising effect. On the other hand, in equation B, if the η_{ECCD} were taken into account instead of η_{fs} the power requirements would increase to $P_{ECRH} = 24$ MW giving $\frac{j_{ECCD}}{j_{BS}} = 5$. Ref.[LaHaye(2006)] uses a much smaller ratio $\frac{j_{ECCD}}{j_{BS}} = 0.9$ whereas in this work and in ref.[Sauter(2006)] $\frac{j_{ECCD}}{j_{BS}} = 2.5$ and $\frac{j_{ECCD}}{j_{BS}} = 2.8$ are obtained; this is explained by the fact that ref.[LaHaye(2006)] also takes into account the effect of (0,0) component of j_{ECCD} which affects $\approx 25\%$ of the stabilisation; if this term were not taken into account, the requirement on the injected power would increase to $P_{ECRH} = 15$ MW with $\frac{j_{ECCD}}{j_{BS}} = 1.1$. For equation A and equation B the threshold island W_{marg} is given by the $\chi_\perp$ model, whereas in equation C it is given by the polarisation model and in this latter case the resulting normalised curve has a higher growth rate and also $\frac{W_{sat}}{W_{marg,ECCD}} = 2 - 3$ compared to the cases A and B

where the growth rate is smaller due to the $\chi_\perp$ assumption and in equation A also because of the inclusion of the Δ'_{GGJ} term. In equation A and C the W_{marg} is quite large and is $\frac{W_{\mathrm{sat}}}{W_{\mathrm{marg}}} = 2 - 3$.

Chapter 8

Summary and Conclusion

The tokamak performance is often limited by the Neoclassical Tearing Modes (NTMs) which are a type of resistive instability characterised by the presence in the plasma of chains of so-called magnetic islands. The most detrimental NTMs have helicities (3,2) and (2,1) where the (2,1) NTMs can even lead to disruptions (dramatic events in which the plasma confinement is suddenly destroyed). Since the onset of this instability scales with the normalised ion-gyroradius ρ_{pi}, in ITER they are expected to be metastable and therefore a lot of effort is taken to be able to experimentally control and stabilise them. The main mechanism underlying the growth of an NTM is related to the existence in a toroidal plasma of the bootstrap current j_{BS} which is proportional to the pressure gradient $\frac{dp}{dr}$: when a magnetic island forms because of some initial seeding process, the short-circuit due to the reconnection of the magnetic field lines leads to a flow of particles and heat towards the edge of the plasma which inevitably flattens the pressure profile inside the island region causing a loss of bootstrap current and reinforcing the magnetic island growth. Experimentally, NTMs are controlled by injecting Electron Cyclotron Current Drive (ECCD) which is used to substitute with the injected j_{ECCD} the bootstrap current j_{BS} which is lost inside the island. The efficiency of the ECCD injection will be inevitably related to how well aligned are the injected ECCD beam and the magnetic island and the figure of merit for stabilisation is given in terms of ratio $\Lambda = \frac{j_{\mathrm{ECCD}}}{j_{\mathrm{BS}}}$ relative to the ratio $\frac{W_{\mathrm{sat}}}{W_{\mathrm{marg}}}$. The behaviour of NTMs during stabilisation experiments is studied using the Modified Rutherford equation which describes the time evolution of the magnetic island width W. In this thesis, the modelling of NTM stabilisation experiments has been carried out by by merging together the recent results present in literature for the various terms (Δ'-terms) present in the Modified Rutherford equation contributing to the physics underlying the NTM evolution and by inserting two free coefficients c_{sat} and c_{stab} to be determined by comparison with a large experimental database. The two fitting parameters c_{sat} and c_{stab} have been added to account for deviations from cylindrical calculations and approximations in the model describing

the NTM at saturation (c_{sat}) and at stabilisation (c_{stab}) respectively. The dominant effects taken into account are the destabilising effect of the missing of bootstrap current j_{BS} inside the island (Δ'_{BS} term) and the counteracting stabilising effect of the externally injected j_{ECCD} current (Δ'_{ECCD}); in addition, other minor stabilising effects have been included such as the effect of the tokamak curvature (Δ'_{GGJ} term) and the effect of the equilibrium current modification (Δ' term). In the Modified Rutherford equation, the seed island necessary for the NTM to develop has been modelled using both the incomplete flattening threshold W_d and the small stabilising effect of the banana orbits W_b whereas the threshold due to the presence of polarisation current W_{pol} has been neglected due to its high uncertainty in the available models. However, in the simulations it has not been found necessary to consider this term at all so that its effect can be considered small or at least comparable to the effect of the other threshold mechanisms. The efficiency of the ECCD injection has been calculated both for continuos (DC) and modulated (AC) injection and a model for describing the real asymmetric shape of the magnetic island (done introducing an asymmetry factor γ) has been included in the averaging procedure for calculating η_{ECCD}. In addition the difference on the island size due to the Shafranov shift between the high-field size (HFS) and low-field size (LFS) has been considered. The modelled Rutherford equation has been used to get different power requirement limits in case of large saturated island and small deposition profile d of the ECCD injection which depend on the ratio $\frac{c_{\mathrm{sat}}}{c_{\mathrm{stab}}}$ and which are found to be consistent with the criterion adopted for ITER $\Lambda > 1.2 \div 1.6$; in addition, a difference between the marginal island width due to lowering of β and the marginal island width when j_{ECCD} is injected during stabilisation has been analytically estimated leading to $W_{\mathrm{marg,ECCD}} \sim 1.5 \div 2\ W_{\mathrm{marg}}$. Since c_{sat} and c_{stab} are machine independent parameters describing only the physics of the NTM and not depending on the size of the devices, a lot of effort has been spent in the determination of a unique and consistent value for c_{sat} and c_{stab} over a multi-machine database of 30 successful NTM stabilisation discharges collected both at ASDEX Upgrade and JT-60U. Due to the small number of modulation experiments only experiments with continuos drive have been taken into account characterised either by a large deposition profile of ECCD injection ($\frac{W_{\mathrm{sat}}}{d} \leq 0$) or by small deposition profile ($\frac{W_{\mathrm{sat}}}{d} > 0$). c_{sat} has been measured as at saturation as $c_{\mathrm{sat}} = \frac{\Delta'}{\Delta'_{\mathrm{BS}} + \Delta'_{\mathrm{GGJ}}}$ whereas c_{stab} has been measured by comparing the integrated island $W(t) = \int \frac{dW}{dt} dt$ with the island width decay observed during the stabilisation and proportional to the detected perturbed magnetic amplitude perturbation. To measure the necessary plasma parameters in the two devices, the collected database of discharges which were used to calculate c_{sat} and c_{stab} has been taken in the same parameter range. However, the experimental schemes to hit the resonant surface of the NTM in ASDEX Upgrade and JT-60U have been modelled differently as in ASDEX Upgrade the linear ramp of the main magnetic field B_T has been considered (radial misalignment $x_{\mathrm{mis}} = r_{\mathrm{dep}} - r_{\mathrm{res}}$ changed linearly in

time) and in JT-60U optimisation from discharge to discharge has been used (x_{mis} is kept fixed in each discharge). The coefficient c_{sat} is found to be constant over a large range of the plasma parameters with a mean value 0.81 ± 0.12. Its consistency among the discharges has been found mainly to be affected by the scaling among β_p, W_{sat} and j_{BS}. In particular, for the (2,1) NTM case, very good linear trends have been found whereas higher uncertainty has been obtained for the (3,2) NTM mainly due to the fact that the (2,1) NTM has more prominent effects which lead to easier measurements in terms of island widths, mode position etc.. In addition, the experimental regime which is investigated has $\frac{W_{\mathrm{sat}}}{W_{\mathrm{marg}}} = 2 - 3$ and therefore the small island physics effects are not negligible. Large variation has been found in the value for $r_{\mathrm{res}}\Delta'$ allowing for c_{sat} to be consistent: for the (2,1) NTMs of ASDEX Upgrade, in fact, $r_{\mathrm{res}}\Delta'$ is set to the more unstable value (close to being positive) $r_{\mathrm{res}}\Delta' = -1$. In order to determine the second fitting coefficient c_{stab}, the values of the deposition width d provided by Fokker-Planck calculations resulted to be unrealistically small in case of the small deposition width discharges of ASDEX Upgrade and therefore these values were re-scaled assuming as a minimum allowable value $d = 0.02$ m. The first determination of c_{stab} lead to a systematic difference in its value among some groups of discharges. This is due to mainly to the fact that in the experiment both over-stabilisation and not precisely known radial misalignment are present. Therefore, by correcting the values of x_{mis} and $\frac{j_{\mathrm{ECCD}}}{j_{\mathrm{BS}}}$ the scatter among the values of c_{stab} has been reduced. In this way, the coefficient c_{stab} resulted to be 0.68 ± 0.22. However, in the Δ'_{ECCD} term only the effect of the injected helical component (m,n) of the current is taken into account, whereas other possible minor stabilising effects as the ECCD pure heating and the effect of (0,0) have been neglected. The radial misalignment x_{mis} in JT-60U which allowed for simulations to overlap well with the experimental curves was found between $0 < \frac{x_{\mathrm{mis}}}{d} < 0.6$ whereas at ASDEX Upgrade even larger initial misalignment is possible $\frac{x_{\mathrm{mis}}}{d} \leq 0.9$ due to the linear ramp of the magnetic field B_T. The experimentally observed marginal island width $W_{\mathrm{marg,ECCD}}$ was found to be $\approx 0.02 - 0.03$ m over the whole database; nevertheless, for the (2,1) NTM discharges at JT-60U the experimental island width decay suggested a larger value of the marginal island width related to the presence of a coupled (3,2) NTM. In general, for NTMs characterised by a ratio $W_{\mathrm{sat}} / W_{\mathrm{marg}} \sim 2 \div 3$, the figure of merit for marginal stabilisation resulted to be $\Lambda \geq 0.3 - 0.5$. To study the effect of the uncertainty on the different quantities present in the modified Rutherford equation a sensitivity analysis has been carried out for understanding the major dependencies in the MRE. The uncertainties of the quantities entering in the Modified Rutherford equation have been set between 5% and 20% depending on the range of variation found in the collected data. The analysis revealed that the value of c_{sat} and c_{stab} has an uncertainty of 30%. The most important quantities which affect the precision with which the two fitting coefficients are determined are in order W_{sat}, j_{BS} and L_q. In addition, the statistical determination of c_{sat} and c_{stab} is

found to be consistent with their determination obtained by using the experimental data. The probability distribution functions for every single discharge and for all the discharges together show a linear correlation between c_{sat} and c_{stab}. These results suggest that further steps in the error analysis of the Modified Rutherford equation studies should focus on the assumptions of distribution functions alternative to the normal distribution for describing some of the quantities present in the Modified Rutherford equation and on the direct inclusion of radial misalignment as a possible source of error. To study the effect of ECCD in ITER, the mean values obtained for c_{sat} and c_{stab} have been inserted in the Modified Rutherford equation. The saturated island width for the (2,1) NTM and (3,2) NTM has been evaluated obtaining as upper values $\sim 0.15\,a$ and $\sim 0.1\,a$ respectively. The simulations with the Modified Rutherford equation have been carried out for both DC and AC injection considering an asymmetric island with $\gamma = 0.5$. The scenario 2 for ITER simulations has been used and the optimised angles of injection which are planned in ITER ECRH system lead to deposition width $d \approx 0.025$ m for the (2,1) NTM case and $d \approx 0.04$ m for the (3,2) case. The main results indicate that in ITER, if the ECCD beam and the O-point of the magnetic island are perfectly aligned, a minimum amount $P_{\mathrm{ECRH}} = 9 - 10$ MW and $P_{\mathrm{ECRH}} = 7 - 10$ MW is required to stabilise the (2,1) and the (3,2) NTM with AC and DC injection respectively. The maximum allowable misalignment is found to be $\frac{x_{\mathrm{mis}}}{d} \leq 0.4 - 0.5$ in case of DC injection and $\frac{x_{\mathrm{mis}}}{d} \leq 0.6 - 0.8$ for AC injection whereas given the values of d and j_{ECCD} and the obtained W_{sat}, a difference which amounts to 10% for the required P_{ECRH} is found between AC and DC injection for marginal stabilisation. The obtained predictions for the ECRH power requirements are compared with the predictions obtained with other forms of the Modified Rutherford equation and are found to be consistent with these. This confirms that NTM control in ITER will be a feasible objective given the capabilities of the planned ECRH system and that the challenging task will be in the optimisation of the alignment (less than $\frac{x_{\mathrm{mis}}}{d} \approx 0.4 - 0.6$) between the ECCD injection beams and the O-point of the magnetic island.

Appendix A

Details on the analysed discharges

Table A.1: Parameters used in the simulations for the analysed discharges including island asymmetry factor γ, $\frac{j_{ECCD}}{j_{BS}}$ (with the values used for the simulations accounting for over-stabilisation in brackets) and normalised misalignment $\frac{x_{mis}}{d}$. The times at which measurements were taken t_{sat} and t_{ECCD} are also listed together with the ratio $\frac{W_{sat}}{d}$ and $\frac{W_{sat}}{W_{marg}}$.

discharge	t_{sat} [s]	t_{ECCD} [s]	$\frac{W_{sat}}{d}$	γ	x_{mis0} [m]	$\frac{W_{sat}}{W_{marg}}$	$\frac{j_{ECCD}}{j_{BS}}$
12257	3.1	3.9	0.8	0.5	0.026	2.1	0.54(0.5)
13631	2.1	2.9	0.6	0.5	0.042	2.2	0.86 (0.5)
15308	2.3	2.7	1.05	0.5	0.03	2.4	1.04(0.5)
17977	2.5	4.0	0.65	0.5	0.05	2.4	0.73
18036	2.5	3.8	1.2	0.5	0.038	2.5	1.19(0.5)
18690	2.5	3.3	1.3	0.5	0.023	2.1	1.1(0.5)
18691	2.5	3.1	1.6	0.5	0.013	2.1	1.37(0.5)
19229	2.5	3.3	2.0	0.5	0.027	2.0	1.32(0.5)
19230	2.5	3.3	1.8	0.5	0.019	2.1	2.0(0.5)
19232	2.5	3.4	1.9	0.5	0.018	2.3	1.64(0.5)
21133	2.5	3.1	1.35	0.5	0.024	2.0	1.05(0.5)
16999	2.7	3.4	1.7	0.5	0.02	2.7	1.39(0.5)
19283	2.5	3.0	3.1	0.5	0.015	3.0	1.0
19454	2.7	3.3	2.9	0.5	0.02	2.3	1.62(0.5)
41647	7.5	8.0	0.8	0.5	0.0	5.7	2.1
41652	7.4	8.7	0.9	0.5	0.0	6.0	1.7
41666	7.5	9.0	1.1	0.5	0.0	6.5	1.3
41695	7.5	9.5	1.3	0.5	0.0	7.5	1.4
46367	8.9	11.5	1.3	0.5	0.0	2.0	0.31
46368	8.9	11.1	1.35	0.5	0.0	2.0	0.37
47788	7.5	8.0	1.34	0.5	0.02	2.0	1.3
47793	7.5	8.2	1.52	0.5	0.02	2.0	0.9
47796	7.5	9.3	1.5	0.5	0.02	2.0	0.42

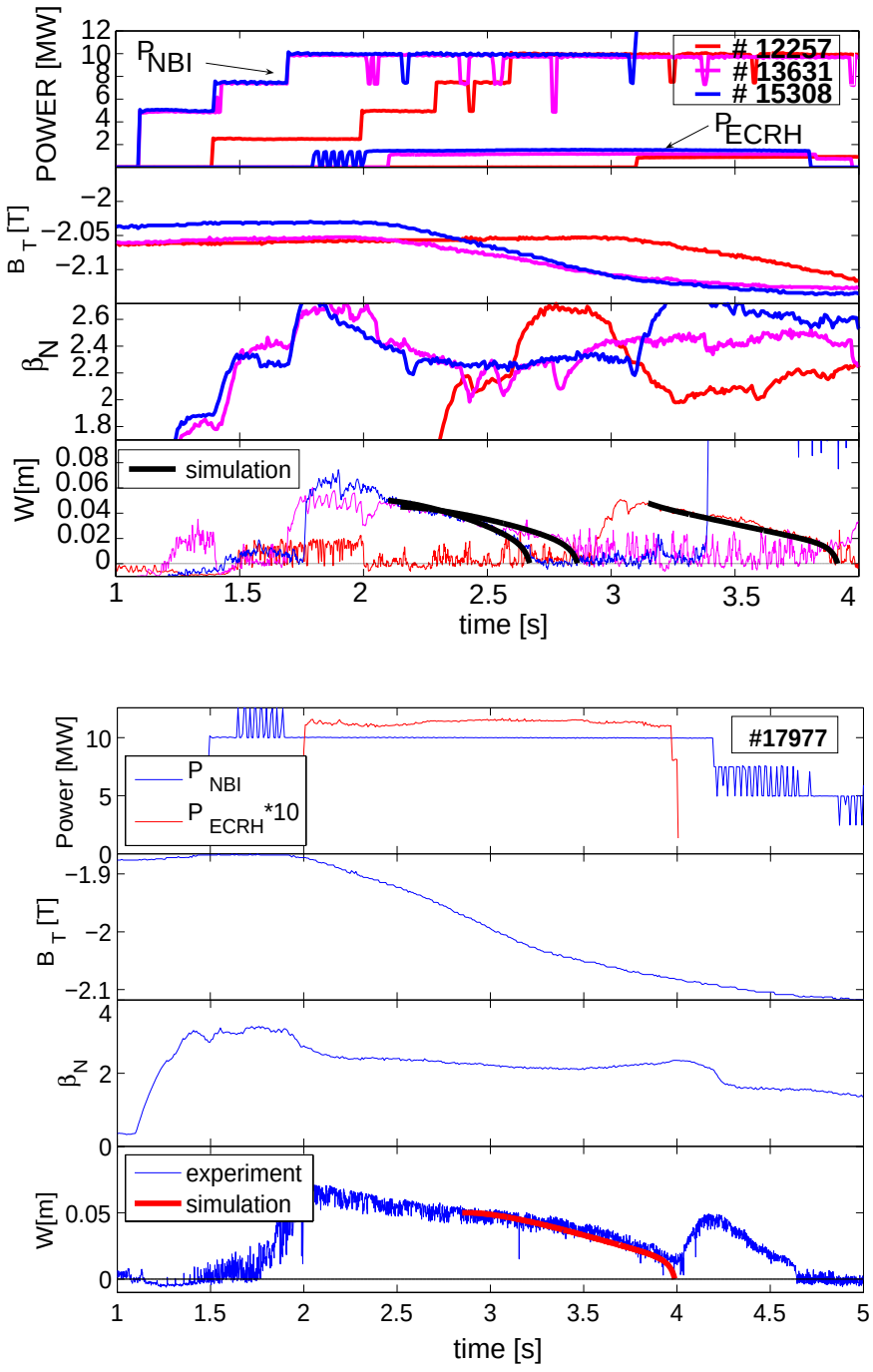

Figure A.1: #12257,#13631,#15308,#17977: (3,2) NTM discharges characterised by a large deposition profile *d*. #12257 starts roughly 1 s later but is very similar to #13631 and #15308. #15308 has a higher $\frac{j_{ECCD}}{j_{BS}}$. Discharge #17977 has a (3,2) NTM which is almost stabilised at 4 s when the ECCD is switched off so that the mode reappears again

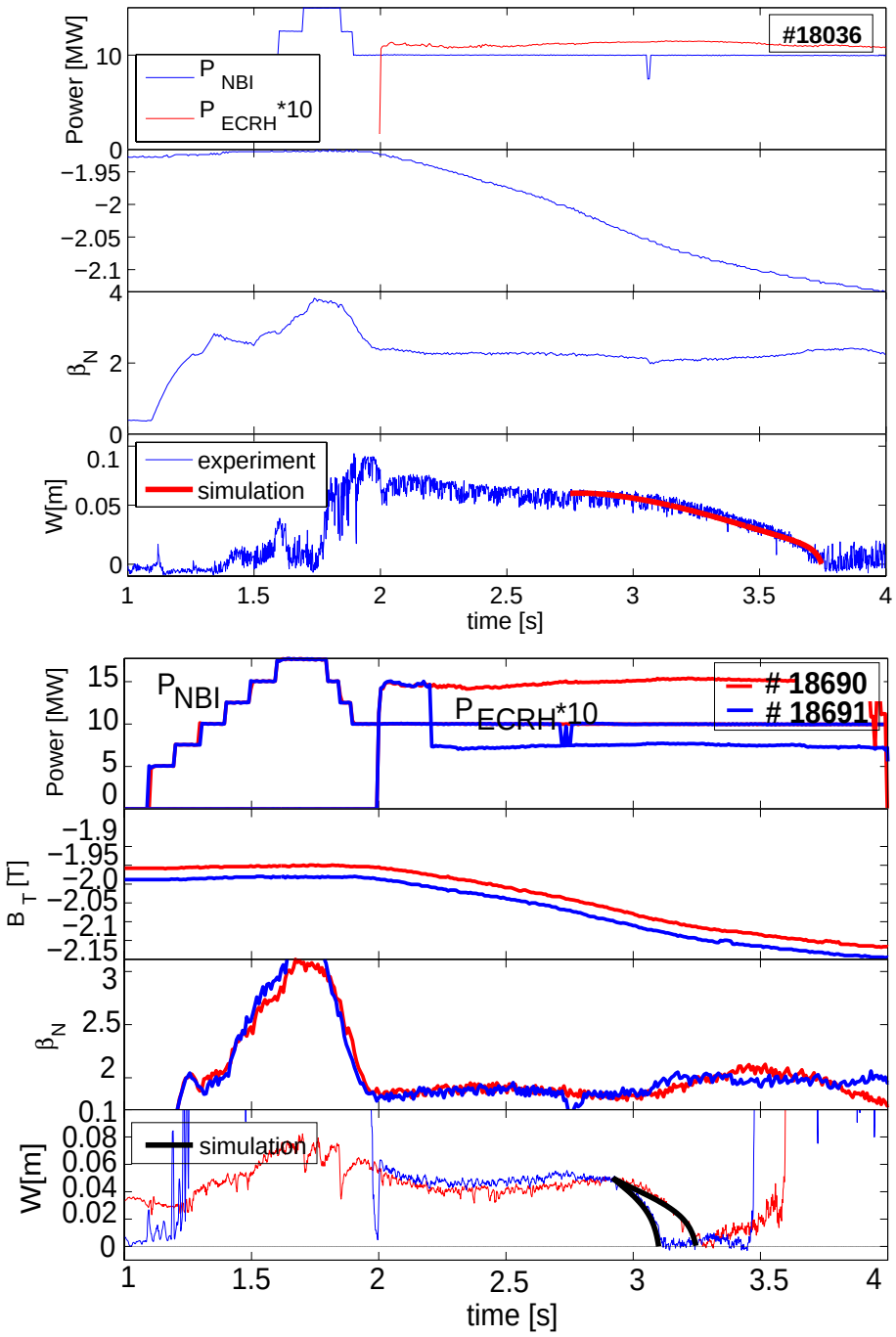

Figure A.2: #18036,#18690, #18691: (3,2) NTM discharge, very similar to #17977 with a smaller initial misalignment x_{mis} and more ECRH power. #18690, #18691 are (3,2) NTM discharges with a small deposition profile, although #18691 has a smaller $\frac{W_{\mathrm{sat}}}{d}$ and almost half of the injected ECRH power, it has a smaller initial misalignment and therefore it is better optimised for NTM stabilisation than #18690

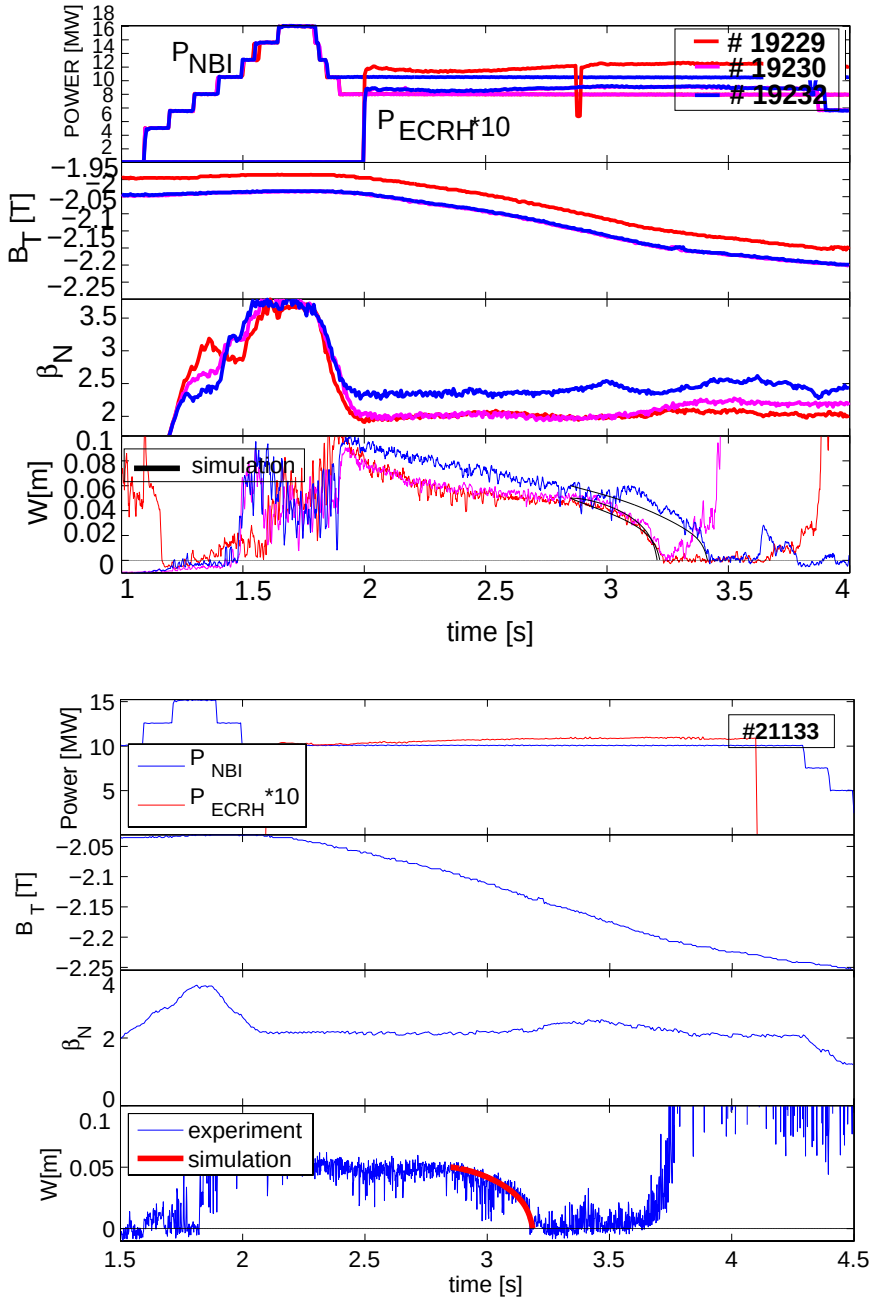

Figure A.3: #19229,#19230,#19232,#21133: (3,2) NTM discharges with a small deposition profile which therefore are characterised by an island width decay almost constant till the ECCD beam gets inside the island. #19229 has the largest misalignment as the initial value of B_T is larger.

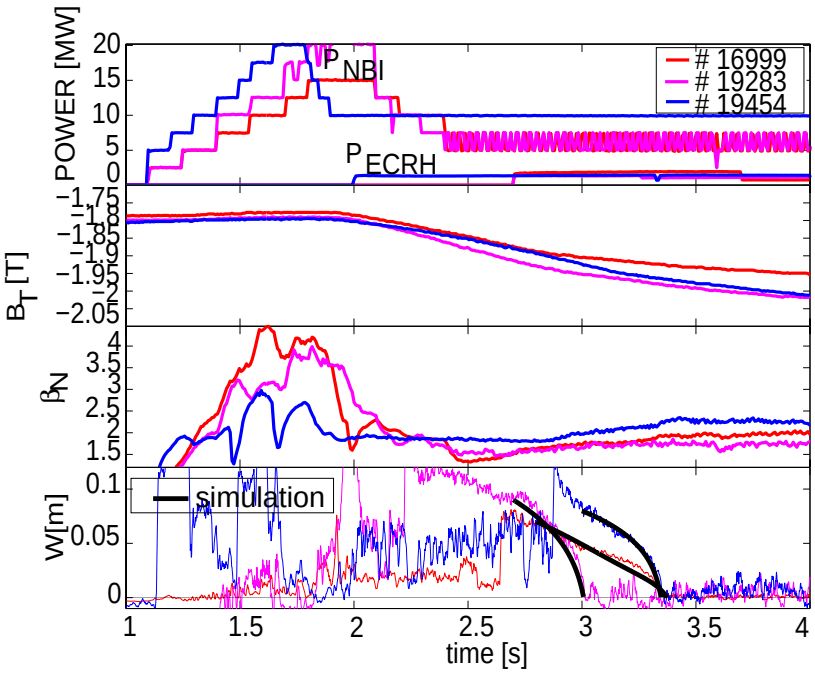

Figure A.4: #16999,#19283,#19454: (2,1) NTM discharges characterised by a small deposition width. #19283 has a smaller misalignment and lower $\frac{j_{ECCD}}{j_{BS}}$ ratio and is one of the most optimised discharges for stabilisation

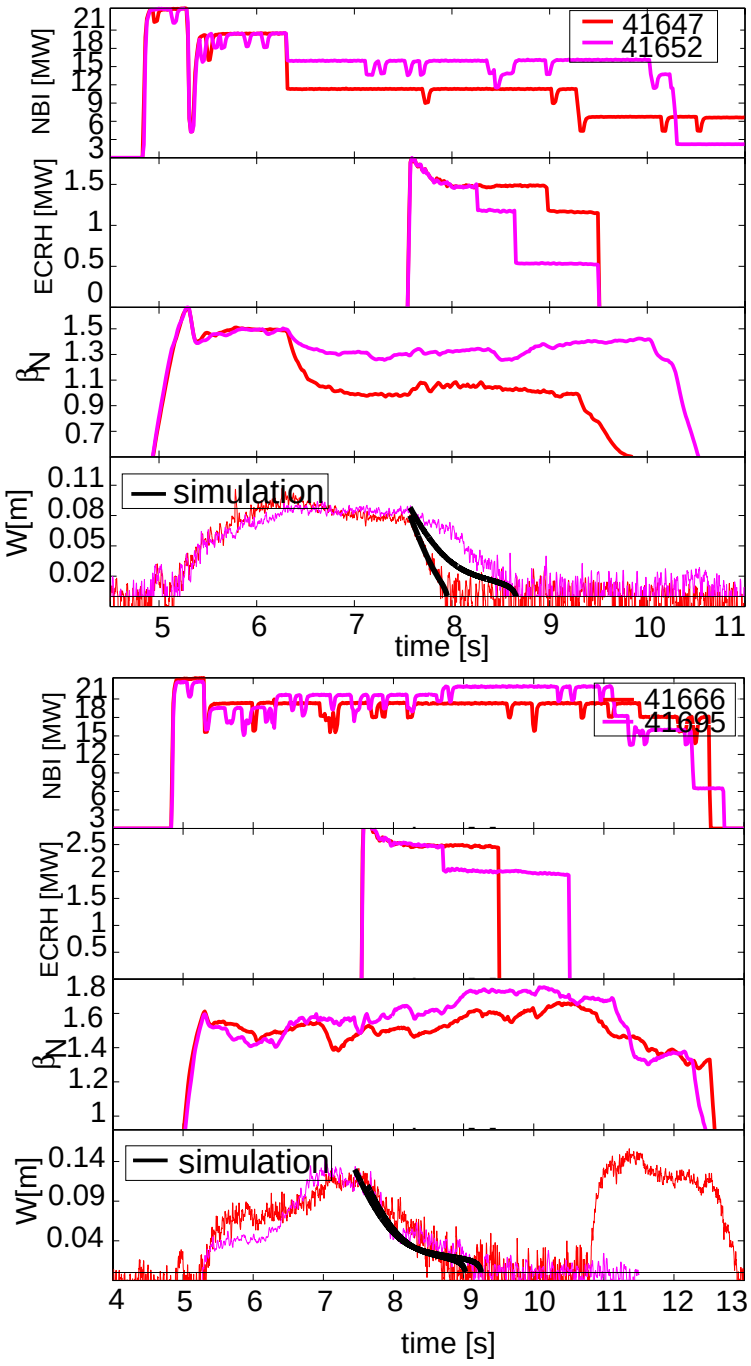

Figure A.5: #41647, #41652,#41666, #41695: (3,2) NTM discharges characterised by a large deposition width and similar misalignment. The discharges have slight different values of *NBI* power and #41652 is characterised by drops in ECRH power during the stabilisation which make the stabilisation time longer.

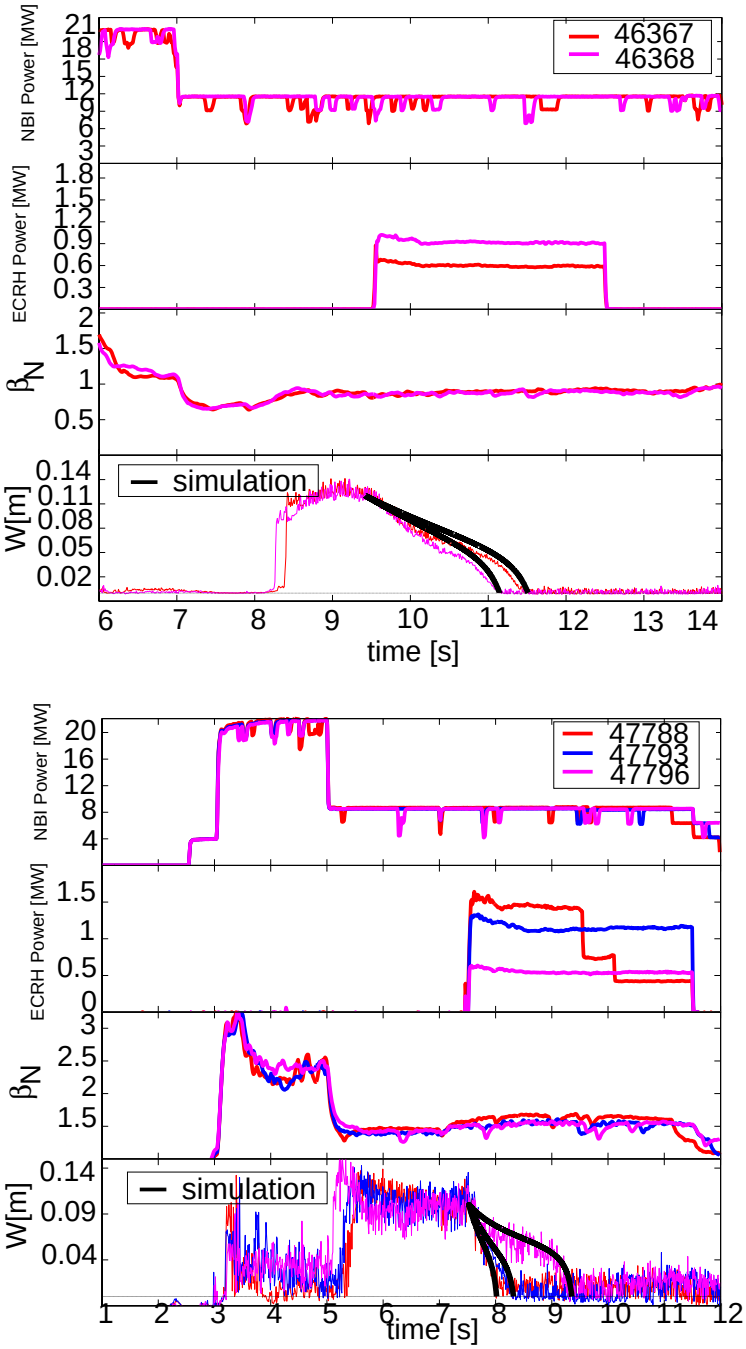

Figure A.6: #46367, #46368,#47788, #47793, #47796: (2,1) NTM discharges characterised by a small ratio of j_{ECCD} / j_{BS} and fine tuned values of injected ECRH power.

Bibliography

[Angioni(2003)] **Angioni, C.** (2003). Density peaking, anomalous pinch, and collisionality in tokamak plasmas. *Physical Review Letters* **90**, 205003–1.

[Azumi(1980)] **Azumi, M.** (1980). *A fluid model numerical code system for tokamak fusion research.* North-Holland Publishing Company.

[Boucher(1992)] **Boucher, D.** (1992). Études et modélisation du transport de l'énergie et des particules dans un plasma de fusion thermonucléaire contrôlée. Application au transport anormal et aux conditions de fonctionnement du tokamak. *Doctoral Thése. Ecole Polytechnique de Paris* .

[Buttery(1999)] **Buttery, R.** (1999). Onset and control of Neoclassical tearing modes on JET. *Proceedings of the 26th EPS Conference on Controlled Fusion and Plasma Physics* **23J**, 121.

[Chang(1995)] **Chang, Z.** (1995). Observation of nonlinear neoclassical pressure-gradient-driven tearing modes in TFTR. *Phys. Rev. Lett.* **74**, 4663–4666.

[Editors(1999)] **Editors, I. P. B.** (1999). Chapter 1: Overview and summary. *Nuclear Fusion* **39**, 2137–2174.

[Fischer(2008)] **Fischer, R.** (2008). Probabilistic Lithium beam data analysis. *Plasma Physics and Controlled Fusion* **50**, 085009 (26pp).

[Fitzpatrick(1995)] **Fitzpatrick, R.** (1995). Helical temperature perturbations associated with tearing modes in tokamak plasmas. *Phys. Plasmas* **2**, 825.

[Freidberg(1987)] **Freidberg, J. P.** (1987). *Ideal Magnetohydrodynamics.* Plenum Press.

[Fujita(1997)] **Fujita, T.** (1997). Plasma diagnostics in a large helical device. *Fusion Engineering and Design* **34-35**, 289–292.

[Fukuda(1989)] **Fukuda, T.** (1989). Frequency stabilized single mode cw 118.8mm CH3OH waveguide laser for large tokamak diagnostics. *Rev. Sci. Instrum* **60**.

[Furth(1963)] **Furth, H. P.** (1963). Finite-resistivity instabilities of a sheet pinch. *Physics of Fluids* **6**, 459–484.

[Gantenbein(2000)] **Gantenbein, G.** (2000). Complete suppression of Neoclassical Tearing Modes with Current Drive at the Electron-Cyclotron-Resonance Frequency in ASDEX Upgrade tokamak. *Phys. Rev. Lett.* **85**, 1242–1245.

[Giruzzi(1999)] **Giruzzi, G.** (1999). Dynamical modelling of tearing mode stabilization by RF current drive. *Nuclear Fusion* **39**, 107–125.

[Glasser(1975)] **Glasser, A. H.** (1975). Resistive instabilities in general toroidal plasma configurations. *Physics of Fluids* **18**, 875–888.

[Goldstein(2007)] **Goldstein, M.** (2007). *Bayes Linear Statistics, Theory and Methods*. Wiley, 2007 edition.

[Günter(1998)] **Günter, S.** (1998). β scaling for the onset of neoclassical tearing modes at ASDEX Upgrade. *Nuclear Fusion* **38**, 1431.

[Hayashi(2004)] **Hayashi, N.** (2004). Numerical analysis of neoclassical tearing mode stabilization by electron cyclotron current drive. *Journal of Plasma and Fusion Research* **80**, 605–613.

[Hegna(1994)] **Hegna, C. C.** (1994). Stability of tearing modes in tokamak plasmas. *Physics of Plasmas* **1**, 2308.

[Hegna and Callen(1997)] **Hegna, C. C. and Callen, J.** (1997). On the stabilization of neoclassical magnetohydrodynamic tearing modes using localized current drive or heating. *Phys. Plasmas* **4**, 2940.

[Henderson(2007)] **Henderson, M.** (2007). EU developments of the ITER ECRH system. *Fusion Engineering and Design* **82**, 454–462.

[Hirshman and Sigmar(1977)] **Hirshman, S. P. and Sigmar, D. J.** (1977). Neoclassical transport of a multispecies toroidal plasma in various collisionality regimes. *Physics of Fluids* **20**, 418–426.

[Isayama(2001)] **Isayama, A.** (2001). Electron Temperature Perturbations Measured by Electron Cyclotron Emission Diagnostic systems in JT-60U. *Fusion Eng. Design* , 129.

[Isayama(2003)] **Isayama, A.** (2003). Achievement of high fusion triple product, steady-state sustainment and real-time NTM stabilization in high-β ELMy H-mode discharges in JT-60U. *Nuclear Fusion* **43**, 1272–1278.

[Kawano(1996)] **Kawano, Y.** (1996). Dual CO2 laser interferometer with a wavelength combination of 10.6 and 9.27m for electron density measurement on large tokamaks. *Rev. Sci. Instrum* **67**, 1520.

[Kirov(2002)] **Kirov, K. K.** (2002). ECRH power deposition studies in ASDEX Upgrade. *Plasma Physics and Controlled Fusion* **44**, 2583–2602.

[Koide(2001)] **Koide, Y.** (2001). Multichordal charge exchange recombination spectroscopy on the JT-60U tokamak. *Review of Scientific Instruments* **72**, 119–127.

[LaHaye(2006)] **LaHaye, R. J.** (2006). Cross-machine benchmarking for ITER of neoclassical tearing mode stabilization by electron cyclotron current drive. *Nuclear Fusion* **46**, 451–461.

[Lütjens(2001)] **Lütjens, H.** (2001). Nonlinear three-dimensional MHD simulations of tearing modes in tokamak plasmas. *Plasma Physics and Controlled Fusion* **43**, A399–A348.

[Maraschek(2003)] **Maraschek, M.** (2003). Scaling of the marginal β_p of neoclassical tearing modes during power ramp-down experiments in ASDEX Upgrade. *Plasma Physics and Controlled Fusion* **45**, 1369–1384.

[Maraschek(2004)] **Maraschek, M.** (2004). Active control of MHD instabilities by ECCD in ASDEX upgrade. *Plasma Physics and Controlled Fusion* **IAEA-CN-116 / EX / 7-2**.

[McCarthy(2001)] **McCarthy, P.** (2001). Current density profile identification in the ASDEX Upgrade pedestal region from kinetic and magnetic data using cliste. In 28^{th} *EPS Conference on Controlled Fusion and Plasma Physics*, volume 25A.

[McCarthy(1999)] **McCarthy, P. J.** (1999). Analytical solutions to the Grad–Shafranov equation for tokamak equilibrium with dissimilar source functions. *Physics of Plasmas* **6**, 3554–3560.

[McCormick(1997)] **McCormick, K.** (1997). Edge density measurements with a fast li beam probe in tokamak and stellarator experiments. *Fusion Eng. Design 34* **34-35**, 125.

[Meister(2001)] **Meister, H.** (2001). Measurement of poloidal flow, radial electric field and e $\times$ b shearing rates at ASDEX Upgrade. *Nuclear Fusion* **41**, 1633.

[Meister(2004)] **Meister, H.** (2004). Z_{eff} from spectroscopic bremsstrahlung measurements at ASDEX Upgrade and JET. *Review of Scientific Instruments* **75**, 4097–4099.

[Meskat(2001)] **Meskat, J. P.** (2001). Analysis of the structure of neoclassical tearing modes in ASDEX Upgrade. *Plasma Physics and Controlled Fusion* **43**, 1325–1332.

[Morris(1992)] **Morris, A. W.** (1992). Feedback stabilisation of resistive tearing modes in tokamaks. *Controlled Fusion and Plasma Physics, Proceedings of the 19th European Conference* **I**, 423–426.

[Murmann(1992)] **Murmann, H.** (1992). The Thomson scattering systems of the ASDEX Upgrade tokamak. *Rev. Sci. Instrum.* **63**, 4941.

[Nagasaki(2003)] **Nagasaki, K.** (2003). Stabilization effect of early ECCD on a neoclassical tearing mode in the JT-60U tokamak. *Nuclear Fusion* **43**, L7–L10.

[Ozeki(2008)] **Ozeki, T.** (2008). Development and demonstration of remote experimental system with high security in JT-60U. In *Proceedings of the* 22^{nd} *IAEA Fusion Energy Conference*.

[Peeters(2000)] **Peeters, A.** (2000). The bootstrap current and its consequences. *Plasma Phys. Control. Fusion* **42**, B231–B242.

[Pereverzev(1991)] **Pereverzev, G.** (1991). Automated System for Transport Analysis. *Report IPP* **5/42**.

[Perkins(2003)] **Perkins, F. W.** (2003). Notes on Neoclassical Tearing Modes.

[Petty(2004)] **Petty, C. C.** (2004). Complete suppression of the $m = 2/n = 1$ neoclassical tearing mode using electron cyclotron current drive in DIII-D. *Nuclear Fusion* **44**, 243–251.

[Pletzer and Perkins(1999)] **Pletzer, A. and Perkins, F. W.** (1999). Stabilization of neoclassical tearing modes using a continuous localized current drive. *Physics of Plasmas* **6**, 1589–1600.

[Polevoi and Gribov(2002)] **Polevoi, A. R. and Gribov, Y.** (2002). Plasma of ITER scenario 2. *Plasma Fusion Research SERIES* **5**, 82–87.

[Poli(2001)] **Poli, E.** (2001). TORBEAM, a beam tracing code for electron-cyclotron waves in tokamak plasmas. *Computer Physics Communications* **136**, 90 – 104.

[Poli(2002)] **Poli, E.** (2002). Reduction of the ion drive and $\rho_\theta*$ scaling of the neoclassical tearing mode. *Physical Review Letters* **88**, 075001.

[Ramponi(2008)] **Ramponi, G.** (2008). Physics analysis of the ITER ECW system for optimised performance. *Nuclear Fusion* **48**, 054012.

[Reimerdes(2002)] **Reimerdes, H.** (2002). From current-driven to neoclassically driven tearing modes. *Physical Review Letters* **88**, 105005.

[Rutherford(1973)] **Rutherford, P. H.** (1973). Nonlinear growth of the tearing mode. *Physics of Fluids* **16**, 1903–1908.

[Sauter(2002)] **Sauter, O.** (2002). Marginal β-limit for neoclassical tearing modes in JET H-mode discharges. *Plasma Physics and Controlled Fusion* **44**, 1999–2019.

[Sauter(2004)] **Sauter, O.** (2004). On the contribution of local current density to neoclassical tearing mode stabilisation. *Phys. Plasmas* **11**, 4808.

[Sauter(2006)] **Sauter, O.** (2006). Partial stabilization and control of neoclassical tearing modes in burning plasmas. In *IAEA Conference*.

[Shafranov(1967)] **Shafranov, V. D.** (1967). Condition for flute instability of a toroidal-geometry plasma. *Soviet Physics JETP* **26**, 682.

[Smolyakov(2004)] **Smolyakov, A. I.** (2004). Ion sound effects on magnetic islands. *Plasma Physics and Controlled Fusion* **46**, L1–L6.

[Stäbler(2003)] **Stäbler, A.** (2003). Current drive in ASDEX Upgrade. *Fusion Science and Technology* **44**, 730–742.

[Suttrop(1996)] **Suttrop, W.** (1996). Principle and limitations of ECE diagnostic. *IPP Report* **1/306**.

[Suzuki(2002)] **Suzuki, T.** (2002). Measurement of current driven by electron cyclotron waves in JT-60U. *Plasma Physics and Controlled Fusion* **44**, 1–9.

[Tani(1992)] **Tani, K.** (1992). Numerical analysis of 2D MHD equilibrium with non-inductive plasma current in tokamaks. *Journal of Computational Physics* **98**, 332 – 341.

[Wesson(1997)] **Wesson, J.** (1997). *Tokamaks*. Oxford University Press, 2nd edition.

[Wolf(1997)] **Wolf, R. C.** (1997). Motional Stark Effect polarimetry for the determination of ASDEX Upgrade current density profile. In 24^{th} *EPS Conference on Controlled Fusion and Plasma Physics*, volume 21A-IV.

[Yoshida(1999)] **Yoshida, H.** (1999). Multilaser and high spatially resolved multipoint Thomson scattering system for the JT-60U tokamak. *Rev. Sci. Instrum* **70**, 751–754.

[Yu(2004)] **Yu, Q.** (2004). Numerical modeling of nonlinear growth and saturation of neoclassical tearing modes. *Physics of Plasmas* **11**, 140–150.

[Zohm(1990)] **Zohm, H.** (1990). Untersuchung magnetischer moden am tokamak ASDEX. *IPP report* **1/254**.

[Zohm(2001)] **Zohm, H.** (2001). The physics of neoclassical tearing modes and their stabilization by ECCD in ASDEX Upgrade. *Nuclear Fusion* **41**, 197–202.

[Zohm(2007)] **Zohm, H.** (2007). Control of NTMs by ECCD on ASDEX Upgrade in view of ITER application. *Plasma Physics and Controlled Fusion* **49**, B341–B347.

Acknowledgements

In the three years of this research work, I learned from the knowledge, encouragement and support of several people. At this stage, I would like to express my gratitude. In particular I would like to thank

- Prof. Dr. Zohm who gave me the opportunity to perform this challenging work under his supervision. I will always consider his great curiosity and his so positive attitude towards scientific research as one of the most important things I learned during this PhD.
- Dr. A. Isayama with whom I collaborated in JT-60U and who supervised me during my visit in Japan. I learned a lot from him and I really appreciate his effort and the time he dedicated to our collaboration. My three months in Japan were just fantastic!
- Dr. M. Maraschek, Dr. R. Fischer and Dr. E. Poli with whom I worked most on both the experiments and analysis and who were very always willing to provide help and suggestions.
- Dr. C. Angioni for explaining me a lot about transport in a tokamak and for helping me to use ASTRA
- Dr. P. McCarthy for explaining how to run and interpret CLISTE results
- the ASDEX Upgrade Team and the JT-60U Team for offering me the possibility to experience their professionalism and expertise in the world of experimental physics and fusion
- Dr. A. Flaws for the time spent showing me the tricks of MATLAB. I think I would still be here listing numbers in ASCII files without him...
- Dr. F. Volpe for the discussions on ECE measurements, NTM physics and for his enthusiasm and support
- the PHD students and colleagues who joined during lunch-time in the kantina, who supported me and always listened to me patiently: Minja, Karl, Manolo, Eleonora, Marco, Arthur, Nano, Costanza, Tillmann, Fernando and many more!
- my parents and my sisters, so spread around the world and nevertheless always so close
- Philipp, who shared with me the nice times but also the difficult times during the realisation of this work
- last but not least, my three dogs Pucci, Belle and Maya